2014

Synthesis of nano-ceramics for supercapacitors

Azrin Akhter Chowdhury
University of Wollongong

Synthesis of Nano-ceramics for Supercapacitors

A thesis submitted in fulfilment of the requirements for the award of the degree

DOCTOR OF PHILOSOPHY

from

The University of Wollongong

By

Azrin Akhter Chowdhury

B.Eng. (Hons)

Materials Engineering

Aug, 2014

CERTIFICATION

I, Azrin Akhter Chowdhury, declare that this thesis, submitted in fulfilment of the requirements for the award of Doctor of Philosophy, in Engineering Materials Institute, Faculty of Engineering, University of Wollongong, is wholly my own work unless otherwise referenced or acknowledged. The document has not been submitted for qualifications at any other academic institute.

Azrin Akhter Chowdhury

29 August, 2014

DEDICATION

For my mom, dad, my brother Tushar and my beloved husband, Tanvir.

ABSTRACT

Cross-disciplinary research into the development of nanomaterials and nanotechnologies for energy storage systems is one of the most dynamic areas of current research and technology. This investigation focused on the synthesis of complex oxide nano-ceramics with dielectric constants, using a new and cost-effective material and fabrication technology described as Electric Discharge Assisted Mechanical Milling (EDAMM). This technique utilises a novel chemical reactor which combines mechanical milling and transferred arc plasma processing for the reactive processing of powders under a controlled atmosphere. This technique was used in this doctoral work to synthesise different types of complex nano-ceramics including; magnesium aluminium iron oxide ($MgAl_2O_4$), calcium copper titanium oxide $CaCu_3Ti_4O_{12}$ (CCT), barium lanthanum titanium oxide $BaLa_2Ti_4O_{12}$ (BLT) and bismuth titanium iron oxide $Bi_5Ti_3FeO_{15}$ (BTF). The processed samples were then pressed into pellets and heat-treated in air to produce recrystallised microstructures with good dielectric properties. The microstructures were studied using X-ray diffraction (XRD), FESEM, Transmission Electron Microscopy (TEM) and Energy-Dispersive X-ray Spectroscopy (EDS) analysis, while the dielectric properties were examined on an LCR meter. Dielectric measurements were performed on pressed and sintered samples using an LCR meter.

For investigation of the initial processing parameters for optimum EDAMM synthesis of complex dielectrics oxides, the $MgAl_2O_4$ – MgO- Al_2O_3 system was studied first. Samples of MgO and Al_2O_3 were processed under both AC and DC type electrical discharge conditions, and under different atmospheres (e.g. Argon, Nitrogen, Helium), each of which have different dissociation temperatures. Starting

powders processed in an argon atmosphere under AC conditions showed the best results with high yields of nano-structural $MgAl_2O_4$ precursor powder which, after pressing and sintering in air, produced high dielectric constant $MgAl_2O_4$. The high quality of the results obtained by EDAMM processing in argon was interpreted in terms of the combination of high Ar dissociation temperature and high-energy transfer, deep penetration of ions into the surfaces of the starting powders and subsequent diffusion. This, in turn, is believed to enhance interactions between particle surfaces and the nucleation and growth of the desired new phase. DC processing resulted in poorer results due to the melting of particles of starting powders possibly because the amount of energy transfer was too high.

Following determination of optimum EDAMM processing parameters, three other high dielectric constant complex oxides; $CaCu_3Ti_4O_{12}$, $BaLa_2Ti_4O_{12}$, $Bi_5Ti_3FeO_{15}$ were successfully synthesised from both elemental and oxide ingredients and these experiments are described in detail in the thesis. Any variations in the dielectric properties were found to depend on the processing and microstructure of these complex oxides; the details of which are in discussed in this thesis. Of the four compositions synthesised, the best dielectric properties were found in $CaCu_3Ti_4O_{12}$, (CCT). This was explained in terms of the internal barrier layer capacitance (IBLC) model of dielectric properties and the nature of the complex CCT microstructure, which comprised semi-conducting grains and an insulating grain boundary structure.

Conventional Magneto-ball milling was also used to process complex nano-ceramics both under ball-particle impact and shear modes under an oxygen atmosphere. The dielectric properties of $CaCu_3Ti_4O_{12}$, (CCT) and $MgAl_2O_4$ produced under the

gentler shear-milling mode showed better results, apparently due to lower amounts of Fe contamination in these samples.

ACKNOWLEDGEMENTS

I would like to express my sincere appreciation to my research supervisors, Associate Professor Andrzej Calka, Dr. David Wexler and Dr. Kostantin Kontantinov for their guidance and assistance throughout different stages of the present work. Their implicit trust in my research abilities not only freed me to pursue my goals, it also gave me an opportunity to learn how to manage time and allocate resources. They were ever vigilant in providing me with additional learning opportunities by supporting my attendance at international conferences.

It is my great pleasure to acknowledge the considerable assistance I received from the people at the University of Wollongong, Australia, during the course of my doctoral studies. Thank you also to my fellow colleagues, Mr. Nick Mackie and Mr. Greg Tillman, whose knowledge and experience proved very helpful in this research.

To my parents, I am forever indebted to their non-stop spiritual support. Most importantly, I wish to express my gratitude to my beloved husband, Tanvir Saqlain whose unfailing love, patience, perseverance and encouragement allowed me to concentrate on my studies.

TABLE OF CONTENTS

3 . EXPERIMENTAL METHODS

LIST OF FIGURES

.

LIST OF TABLES

List of Equations :

$$C = \varepsilon_r \varepsilon_o \frac{A}{d} \quad (2.1)$$

$$C = \frac{dq}{dv} \quad (2.2)$$

$$W = \int_0^Q V dq = \int_0^Q \frac{q}{C} dq = \frac{1}{2}\frac{Q^2}{C} = \frac{1}{2} CV^2 = \frac{1}{2} VQ \quad (2.3)$$

$$C = \varepsilon \frac{n.A}{d} \quad (2.4)$$

$$U = \frac{W}{Ad} = \frac{\int_0^Q V dq}{Ad} = \int_0^{E_{max}} D dE \quad (2.5)$$

$$U = \int_0^{E_{max}} P dE \quad (2.6)$$

$$U = \int_0^{E_{max}} \varepsilon_0 \ \varepsilon_r E dE \quad (2.7)$$

$$U = \int_0^{E_{max}} P dE = \frac{1}{2} \varepsilon_0 \varepsilon_r E^2 \quad (2.8)$$

$$x = \exp\left[-\frac{Ea}{RT}\right] \quad (2.9)$$

$$A_xO + vB\text{-}xA + B_xO \quad (2.10)$$

$$\frac{3}{2} KT_i = \frac{1}{2} m_t v_t^2 \quad (2.11)$$

$$n\lambda = 2d\sin\Theta \quad (3.1)$$

$$D = \frac{0.9\lambda}{\beta\cos\theta} \quad (3.2)$$

$$d = \lambda / 2n \sin\alpha \quad (3.3)$$

$$\lambda = \frac{h}{\left\{2m_0 E\left(1+\frac{E}{2m_0c^2}\right)\right\}^{1}/_{2}} \quad (3.4)$$

$$Ba^{2+} = La^{3+} + e^- \quad (4.1)$$

$$Ba^{2+} + \frac{1}{4} Ti^{4+} = La^{3+} + \frac{1}{4} \square Ti \quad (4.2)$$

$$\lg p(O2) = \frac{A}{xc} + B \quad (4.3)$$

$$[V_o^{gg}] = \left[La_{Ba}^{g}\right]^{-n} \quad (4.4)$$

$$2O_o^x = O_2(g) + 2V_o^{\cdot} + 4e' \quad (4.5)$$

List of Publications

Publications:

1. Rapid Synthesis of Functional Oxides by Electric Discharge Assisted Mechanical Milling Method-Andrzej Calka, Professor; Azrin Chowdhury; Konstantin Konstantinov,Dr **;** (Journal of Alloys and Compounds; Volume 536, Supplement 1 Pages S3–S8).

2. High dielectric constant nano-structure ceramics synthesis using novel Electric Discharge Assisted Mechanical Milling and Magneto Ball Milling and its properties by *Andrzej Calka, Professor; Azrin Chowdhury; Konstantin Konstantinov,Dr* - (accepted in International Journal of Nanotechnology).

3. Ultra-fast synthesis and properties of high dielectric constant CCT ceramics by EDAMM in oxygen and argon plasma by *Andrzej Calka, Professor; Azrin Chowdhury; Konstantin Konstantinov,Dr*-submitted in Journal of European Ceramic Society.

4. Synthesis and properties of $MgAl_2O_4$ from MgO and Al powders as starting constituents by mechanical alloying in oxygen atmosphere by *Andrzej Calka, Professor; Azrin Chowdhury; Konstantin Konstantinov,Dr* . (under preparation)

5. Fast synthesis and properties of $MgAl_2O_4$ by EDAMM of MgO and Al_2O_3 in oxygen, nitrogen, argon and helium plasma at atmospheric pressure by *Andrzej Calka, Professor; Azrin Chowdhury; Konstantin Konstantinov,Dr* . (under preparation)

6. Comparison of EDAMM and conventional ball milling methods in synthesis and properties of CCT high dielectric constant ceramics by *Andrzej Calka, Professor; Azrin Chowdhury; Konstantin Konstantinov,Dr* . (under preparation)

List of abbreviations

Abbreviation	Full name
FE-SEM	Field emission scanning electron microscopy
EDS/EDX	Energy dispersive X-ray spectroscopy
SEM	Scanning electron microscopy
XRD	X-ray diffraction
TEM	Transmission electron microscopy
EMI	Engineering Material Institute
ISEM	Institute of superconducting and electronic materials
CCT	Calcium copper titanate
$MgAl_2O_4$	Magnesium aluminium oxide
BTF	Bismuth titanium iron oxide
BLT	Barium lanthanum titanate
C	Capacitance
ε_r	Dielectric constant
ε_o	Electric constant / absolute dielectric permittivity
A	Area
V	Voltage
Q	Charge
E	Electric field
MLCC	Multi layer ceramic capacitor
EDAMM	Electric Discharge Assisted Mechanical Milling
nm	Nanometer
wt%	Weight percentage

Abbreviation	Full name
N	Newton
eV	Electron volt
Kpa	Kilo Pascal
f	Frequency
tanδ	Dielectric loss
SPS	Spark plasma sintering
AC	Alternate current
DC	Direct Current
mA	Milliampere
T	Temperature
N_2	Nitrogen
Ar	Argon
He	Helium
O_2	Oxygen
Ɵ	Angle
Ὼ	Resistance
IBLC	Internal barrier layer capacitance
□	Vacancy.

CHAPTER 1. INTRODUCTION

The rapidly increasing demand to develop more powerful and cost-effective energy storage systems and devices is leading to the worldwide implementation of energy efficient and green technologies that are aimed at limiting global climate change. Rechargeable batteries, currently the most popular conventional energy storage devices, have some generic limitations that arise from their electrochemical storage mechanism, and there are also some upper limits to their power and energy storage densities, which are determined by the materials used for the electrodes. They also suffer from a relatively short life and high replacement costs. This has motivated the research and development of other alternative types of energy storage devices such as supercapacitors, which are currently attracting worldwide attention from researchers and industrial investors. A breakthrough is currently occurring in this field that involves the development of new hybrid systems and new types of materials with very high permittivity. This project focused on the cross-disciplinary field of advanced nanostructured materials and their application to new generations of energy storage systems, and the significant impact this would have on the world economy.

The overall aim was to develop new nanoscale ceramic composite materials for high performance ceramic solid state Supercapacitors, using innovative technologies. These materials include complex nano-ceramic multi-layered materials. The specific scientific aims are outlined as follows:

- Apply the EDAMM method to fabricate novel nanostructured perovskites with giant dielectric permittivity, and low temperature dependent dielectric constants for application of solid state ceramic supercapacitors. The latest categories of supercapacitors are potentially promising to replace or argument Li-ion batteries in the future.
- Study the dielectric properties of complex nano-ceramics systems in order to improve their capacitance and energy storage performance.

CHAPTER 2: LITERATURE REVIEW AND THEORETICAL BACKGROUND

2.1 Introduction

Over the past decade, there has been a rapidly rising interest in energy storage devices that can deliver high power and have a long life; of which rechargeable lithium batteries and supercapacitors are the most prominent alternatives. Super capacitors provide higher specific power than batteries and higher specific energy than conventional dielectric capacitors that are filling up the gap between batteries and conventional capacitors due to the high capacitance of the electrode materials. At present, electric double layer capacitors and Redox super capacitors are being investigated more than any others because these supercapacitors can deliver high power and store a remarkable amount of energy. Even if their stored energy is less than lithium batteries, they can be charged and discharged for hundreds of thousands of cycles without adversely affecting their lifetime; albeit batteries are known to suffer from a low cycling life (generally <1000). Figure 2.1 shows the power density as a function of energy density of these energy storage devices [1]. Commercially used conventional dielectric capacitors are primarily manufactured from dielectric polymers or dielectric ceramic, with an average energy density of 10^{-2} to 10^{-1}W.h/kg (less than 2 J/cm3)[2, 3] . Unlike conventional dielectric capacitors, although electrochemical supercapacitors have a moderate energy density, their power density still does not meet the requirement in some super-high-powered electronics and systems. At present, an electrochemical supercapacitor is limited by its high self-discharge, high dielectric absorption, and low internal resistance which allows for

rapid discharge. So the energy storage density of the dielectric capacitors could become competitive with electrochemical supercapacitors or even batteries; their field of application would be greatly expanded. Despite this, an overall summary of the research status of dielectric materials for high-energy storage has still not been carried out, so in this present work, some physical principles were first applied to indicate the basic rules for exploring these promising materials. A breakthrough that involves the development of new hybrid systems and new types of materials with very high permittivity is currently going on this field, with an emphasis on a ceramic solid state ultra-capacitor based on the electrostatic charge mechanism in ultra-high permittivity ceramic composite with a potentially high-energy storage. Moreover, investigations into the energy storage of dielectric materials such as anti-ferroelectric, dielectric glass-ceramics, relaxor ferroelectrics, and polymer-based ferroelectrics are also current.

In this project, we will attempt to synthesise nanostructured ABO_3 perovskite ceramic composites with proven giant dielectric permittivity and low temperature dependence.

2.2 Energy Storage Devices:

There are various types of energy storage devices currently used to mitigate the demand for more powerful and cost-effective energy storage systems i.e.; fuel cells, conventional batteries, ultra-capacitors and conventional capacitors. A Ragone chart was used to assess the performance of various energy-storing devices, such that the values of energy density (in Wh/kg) are plotted versus power density (in W/kg). A Ragone chart was first used to compare the performance of batteries [4] , but it can also compare any energy-storing device, as shown in Figure 2.1.

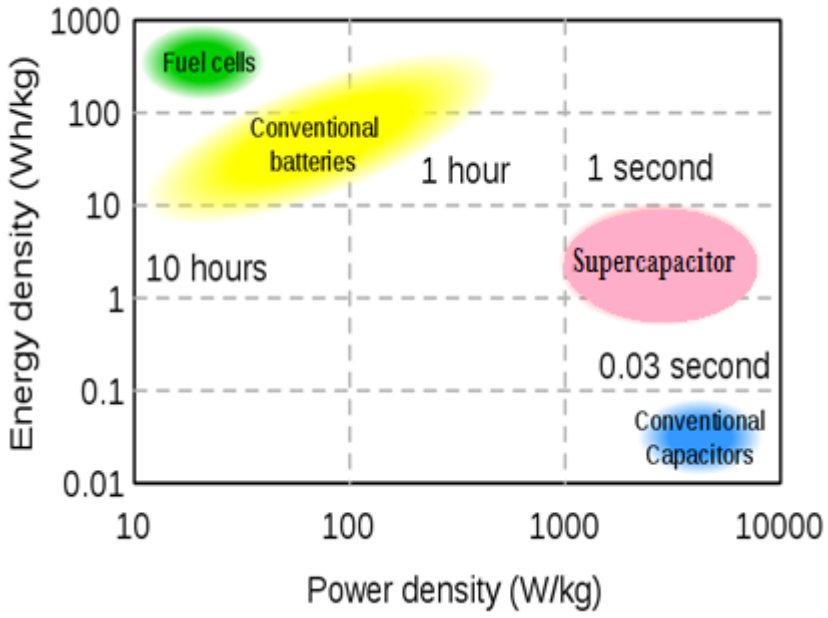

Figure 2.1: Ragone chart showing energy density vs power density for various energy-storing devices.

2.2.1 Fuel Cells:

A fuel cell converts chemical energy from a fuel into electricity through a chemical reaction with oxygen or another oxidising agent [5] such as hydrogen (the most common fuel), although hydrocarbons such as natural gas and alcohols are also used. Fuel cells differ from batteries in that they require a constant source of fuel and oxygen/air to sustain the chemical reaction, whereas fuel cells can produce electricity continuously, as long as these inputs are supplied.

2.2.2 Conventional Batteries:

An electric battery consists of one or more electrochemical cells that convert stored chemical energy into electric energy. Each cell contains a positive terminal (cathode), and a negative terminal (anode). Electrolytes allow ions to move between the electrodes and terminals, which in turn allows a current to flow out of the battery to perform work.

2.2.3 Conventional Capacitors:

A capacitor stores energy in an electric field created between a pair of conductors on which equal but opposite electric charges have been placed. Capacitors are fundamental electrical circuit elements that store electrical energy in the order of microfarads, and also assist in filtering. Capacitors have two main applications, one function is to charge or discharge electricity and the other function is to block the flow of DC. This function is applied to filters that extract or eliminate particular frequencies.

Energy storage in a capacitor is a function of the voltage between the plates, indeed its ability to store energy as a function of voltage (potential difference between the two leads) results in trying to maintain voltage at a constant level. When the voltage across a capacitor has increased, it draws current from the rest of the circuit, and in this condition it is said to be *charging,* but when the voltage across a capacitor has decreased, it supplies current to the rest of the circuit by acting as a power source. In this condition, a capacitor is said to be *discharging.*

2.2.4 Supercapacitors:

Supercapacitors fit in between batteries and conventional capacitors in terms of energy density, so their classification is somewhat complex (Figure 2.2). They can be classified depending on the material used and /or on the energy storage mechanism. The term “Supercapacitor” was originally linked only with carbon-based electrochemical capacitors that used an electric double layer (EDL) electrostatic mechanism.

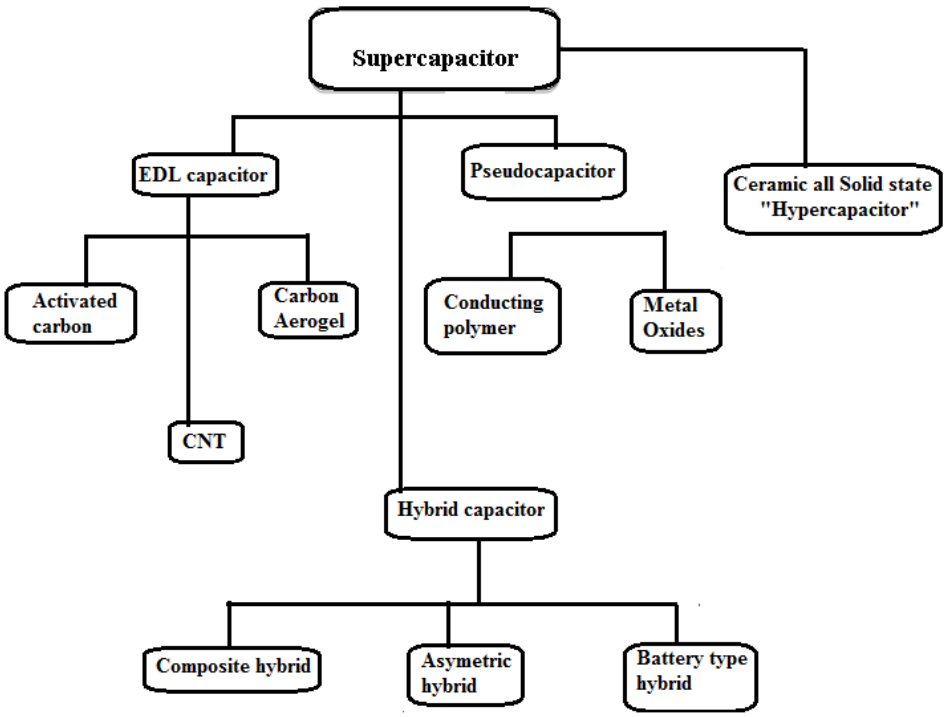

Figure 2.2: Classification of Supercapacitors

Various carbon-based materials have been used as electrodes in EDL ultra-capacitors, i.e., : activated carbon, carbon nanotubes (CNTs), carbon aerogels, glassy carbon, and others [6-8]. They generally have an excellent lifecycle, albeit with limited specific capacitance values and low working voltages up to 2.7 V. Pseudocapacitors store a charge through fast reversible oxidation-reduction reactions involving a charge transfer between electrode and electrolyte that is accomplished through electrosorption, reduction-oxidation reactions, and intercalation processes [9]. Some pseudocapacitors are based on metal oxides and hydroxides, such as MnO_2, $Co(OH)_2$ and especially RuO_2, and they can achieve higher energy and power densities than similar EDL supercapacitors and conducting polymer pseudocapacitors [10-15]. Indeed, the equivalent series resistance (ESR) of hydrous RuO_2 is also lower than other electrode materials, which is an added advantage, but

its success as a material, is limited by its prohibitive cost. Metal oxide based supercapacitors also suffer from poor cyclability, while conducting polymers, which are famous for their flexibility, also have a limited lifecycle and poor capacitance.

Hybrid supercapacitors attempt to exploit the relative advantages and mitigate the relative disadvantages of EDL supercapacitors and pseudocapacitors to realise better performance characteristics [16-18]. They use hybrid or composite electrode materials and systems that are asymmetric (electrodes of different materials) or incorporate a combination of supercapacitor/ battery. Supercapacitors coupled with batteries or fuel cells are being considered as promising solutions for low or zero emission transport vehicles [19] .

Since 2006, a new type of all solid state ceramic supercapacitor has been in development. They are based on the electrostatic charge mechanism in complex ceramic composites with very high permittivity [20, 21]and thus are far outperforming all previous systems. These materials can potentially reach higher energy density values than the current Li- ions batteries.

Supercapacitors can also be classified, according to the electrolyte used, i.e., as aqueous or organic based. Organic electrolytes make it possible to achieve higher working voltages up to 2.7 V (1 V for aqueous), but are more expensive and have 20-50 times higher resistance. Depending on the electrode materials used for the electrodes, supercapacitors can be classified as symmetric (electrodes made from the same materials) or asymmetric (electrodes made from different materials). In the latter case, the total capacitance is now close to the higher capacitance value of the corresponding electrode.

2.3 Conventional Capacitor Properties:

2.3.1 Capacitance and Dielectric Properties of Different Types of Oxide Materials:

A capacitor stores energy in the electric field created between a pair of conductors on which equal but opposite electric charges have been placed. Their main characteristics are: capacitance, dielectric strength, dielectric strength, and electric breakdown voltage.

2.3.2 Capacitance: A capacitor typically consists of two conductor plates filled with certain dielectric materials, as shown in Figure 2.3. The ability of a capacitor to store energy is called its capacitance, which is governed by the physical dimensions (geometry) of the conductors and permittivity of the dielectrics. Capacitance is independent of the potential difference between the conductors and total charge on them, for example, the capacitance of a parallel plate capacitor constructed of two parallel plates fulfilled with certain dielectrics is approximately equal to the following:

$$C = \varepsilon_r \varepsilon_o \frac{A}{d} \qquad (2.1)$$

Where C is the capacitance, A is the area of overlap of the two plates, ε_r is the relative permittivity (also known as dielectric constant), $\varepsilon_o$is the dielectric constant or absolute dielectric permittivity (8.85×10^{-12} Fm^{-1}) and d is the distance between the plates. Capacitance is directly proportional to the overlap area of the conductor plates and the relative permittivity of the dielectrics, while being inversely proportional to the distance between the plates.

A capacitor's capacitance (*C*) is a measure of the potential difference or *voltage* (*V*) which appears across the plates for a given amount of charge (*Q*) stored on each plate: C = Q/V. In SI units, a capacitor has a capacitance farad. Factors that affect the capacitance are: plate area, plate spacing and the dielectric materials.

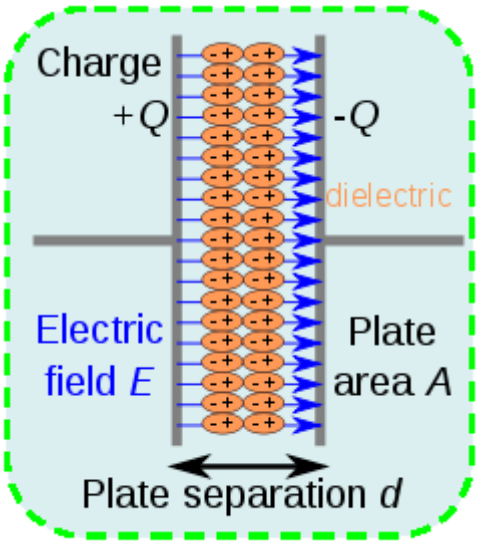

Figure 2.3: Parallel plate capacitor under the function of electric field.

As Figure 2.3 shows, if an external voltage V is applied onto the conductor plates, electric polarisation occurs such that positive and negative charges with equal content will accumulate on the two plates, respectively, that is called the charge process of the capacitor. The charge process will finish when the electrical potential caused by the accumulated charge -Q on both plates is equal to the external applied voltage V; so Q=V is equal to the capacitance C of the capacitor. Sometimes, the relative permittivity of the dielectrics is changed by an external bias which causes the capacitance to vary, in which case capacitance is defined in terms of incremental change:

$$C = \frac{dq}{dv} \qquad (2.2)$$

During the charge process, the charges are moved between the conductor plates by the function of external bias, that indicates that work must be done and electric energy is being stored in the dielectrics at the same time. Hence, the amount of stored energy, W could be obtained from the following formula:

$$W = \int_0^Q V dq = \int_0^Q \frac{q}{C} dq = \frac{1}{2}\frac{Q^2}{C} = \frac{1}{2}CV^2 = \frac{1}{2}VQ \qquad (2.3)$$

2.3.3 Capacitor Leakage:

Any type of capacitor may develop excessive leakage if it is subjected to excessive applied voltage or high voltage spikes.

These types of overloads may actually puncture the dielectric material and produce a short circuit or high resistance leakage path.

2.3.4 Dielectric Strength:

The dielectric strength is the capability of a material to withstand an electric field without breaking down while allowing an electric current to pass. It has units of volts per unit thickness of the dielectric material.

2.3.5 Dielectric Polarisability:

The degree of polarisability or charge storage capability of a material is identified by the term relative dielectric constant (k); this is also referred to as relative permittivity.

2.3.6 Breakdown Voltage:

The breakdown voltage of an insulator is the minimum voltage that caused a portion of an insulator to become electrically conductive. Factors affecting the breakdown voltage are as follows:

For a capacitor, it will depend on: 1) Properties of dielectric materials, 2) the thickness of the dielectric materials, and 3) sometimes the resistance of the circuits.

2.3.7 Design of A Capacitor:

Typical designs consist of two conductive electrodes or plates, each of which stores an opposite charge, that are separated by an insulator or dielectric. The charge is stored at the surface of the plates and at the boundary with the dielectric. A ceramic capacitor is where ceramic material acts as dielectrics. Ceramic capacitors, especially the multi-layered (MLCC), are used in electronic applications [22]. An MLCC consists of a number of individual capacitors stacked together in parallel and connected via terminal surfaces (shown in Figure 2.3).

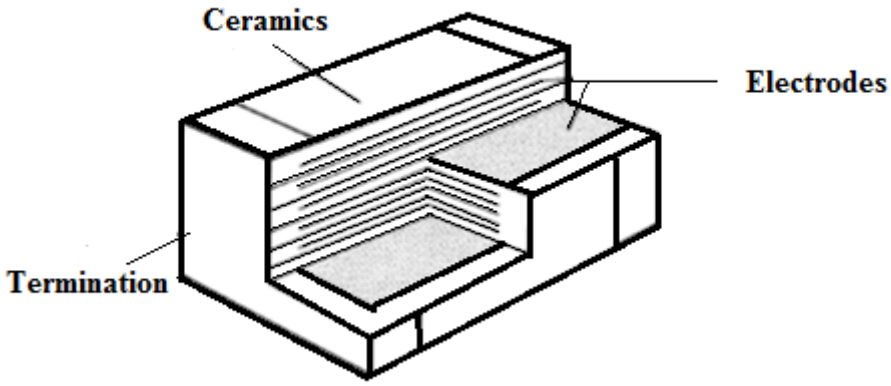

Figure 2.4: Design of Multi-layer ceramic capacitor

The capacitance formula (C) of an MLCC capacitor is based on the formula for a plate capacitor with a number of layers:

$$C = \varepsilon \frac{n.A}{d} \tag{2.4}$$

Where ε is the dielectric permittivity; A is for the surface area of the electrode; n is the number of layers and d is the distance between the electrodes.

2.4 Energy Storage Density Measurement for Dielectric Capacitor:

Energy storage density is the amount of energy stored in a given system or region of space per unit volume or mass of a dielectrics *U*. The energy storage density could be induced from the above formula (3), but from a physics base, it could be known that the charge density (Q/A) on the conductor plate of capacitor is equal to the electrical displacement D ($D = \varepsilon_o \varepsilon_e E$) in the dielectrics. Thus, by combining with the formula (3), the energy -storage density *U* could be expressed as follows:

$$U = \frac{W}{Ad} = \frac{\int_o^Q V dq}{Ad} = \int_0^{E_{max}} D dE \tag{2.5}$$

where E is the external applied electrical field and is equal to V=d, and other letters are defined just as before. For dielectrics with a high permittivity, the electrical displacement D was very close to their electrical polarisation P, so formula (5) can be rewritten as:

$$U = \int_0^{E_{max}} P dE \tag{2.6}$$

Based on this equation, the energy storage density of the dielectrics can be obtained. The curve of the electric field-polarisation (P-E) loops is shown in Figure 2.5.

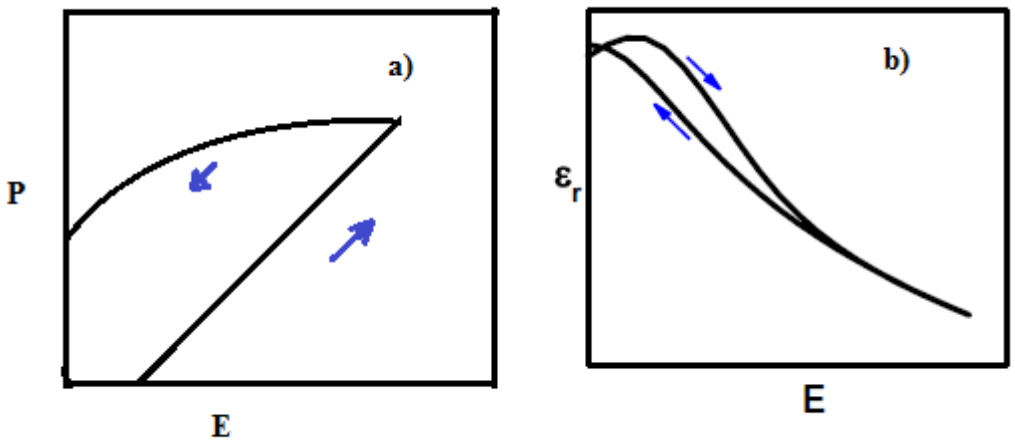

Figure 2.5: a) Polarisation b) permittivity on electric field of ferroelectrics.

Since the permittivity was defined as dP/dE as shown in Figure 2.5 b), the formula (6) can be expressed as:

$$U = \int_0^{E_{max}} \varepsilon_0 \ \varepsilon_r E dE \qquad (2.7)$$

For linear dielectric materials, whose permittivity is independent of any external applied field, the formula (7) can be expressed as follows:

$$U = \int_0^{E_{max}} PdE = \frac{1}{2}\varepsilon_0 \varepsilon_r E^2 \qquad (2.8)$$

This result indicates that the energy storage density for linear dielectric materials is directly proportional to the relative permittivity of the dielectrics, and to the square of the operating field.

2.5 Complex Ceramic Oxides:

In recent years, compounds based on compositions of barium, titanium and REE (rare earth element) oxides are becoming the most promising from the point of view

of electrical properties[23]. Oxides with a perovskite structure have high dielectric constant, and a dielectric constant higher than 1000 is known as relaxor which shows ferroelectric properties. In most cases the relaxors are limited by their temperature dependency but Subramanian et al [24] reported one class of oxides ($\boldsymbol{A}Cu_3Ti_4O_{12}$, where $\boldsymbol{A}$=trivalent rare earth or Bi) with a perovskite structure had dielectric properties with low temperature dependency compared to those of ferroelectrics or relaxors. Some ceramic materials having dielectric properties are described below:

2.5.1 Magnesium Aluminium Oxide ($MgAl_2O_4$):

$MgAl_2O_4$ is a mixed oxide material whose physical properties range between magnesium and aluminium oxide. $MgAl_2O_4$ nano-ceramic has high strength, a high melting point, and good resistance, although Zhang [25] reported dielectric behaviour with temperature. It has been shown that the dielectric constant of $MgAl_2O_4$ nano-ceramic does not vary significantly with temperature. $MgAl_2O_4$ Crystals have a spinel structure with lots of important properties, indeed many unconventional methods such as precipitation, the aerosol method, the citrate-nitrate route, classical Sol-gel route combining gelation and co-precipitation were used to prepare $MgAl_2O_4$ [26]. In recent years, mechanical synthesis has been one of the methods successfully used to produce $MgAl_2O_4$ that avoided the formation and calcinations of its precursors at high temperature. This method involved a single step where powder mixtures were milled at room temperature under an air atmosphere. The degree of $MgAl_2O_4$ formation depends on the milling time, but to have a 99% degree of formation takes 160h [27].

2.5.2 Calcium Copper Titanium Oxide ($CaCu_3Ti_4O_{12}$):

In recent years, the researcher has found that cubic perovskite $CaCu_3Ti_4O_{12}$ (shown in Figure 2.6) has a high dielectric constant, and its permittivity can even be increased from 10,000 to 300,000, as a result of grain growth. The dielectric constant of this ceramic does not depend on temperature which makes it more attractive [28], especially since no phase transition can occur between 25^0C to1000^0C [29]. The origin of the high permittivity of $CaCu_3Ti_4O_{12}$ is not yet fully understood, but according to some authors, the polarisability and dielectric constant are enhanced by tension on the Ti-O bonds and some others claim that microstructure and Ca/Cu ratio cause the high dielectric constant[30].

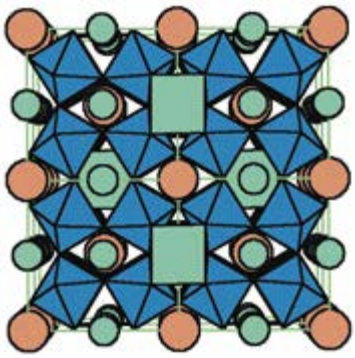

Figure 2.6: Crystal structure of $CaCu_3Ti_4O_{12}$; Brown spheres = Ca, Green spheres = Cu, Blue = TiO_6 units; green squares = CuO_4 planar units.

Sinclair et al 4 believed, that according to impedance spectroscopy studies, a high dielectric constant is associated with the internal barrier layer capacitor. They showed that a $CaCu_3Ti_4O_{12}$ compound has electrically heterogeneous properties which consist of semi-conducting grains with an insulating grain boundary[31]. Recently Ni-, Fe- and Co-doped CCT gave enormous results of dielectric permittivity, up to 150,000, by Co-doping on Ti-site [32]. Dong reported a dielectric constant value of 420,000 by substituting Ti with Nb in $CaCu_3Ti_{4-x}Nb_xO_{12+x/2}$ (where

x = 0). [33]. Another concern with this ceramic is reducing the loss of dielectric by doping with suitable elements such as La [33].

2.5.3 Bismuth Titanium Iron Oxide, $Bi_5Ti_3FeO_{15}$ (BTF):

$Bi_5Ti_3FeO_{15}$ (BTFO) is an Aurivillius compound characterised by a high phase transition temperature (1023K) and interesting dielectric properties. Aurivillius compounds are a family of layered Bi-containing oxides, whose existence has been known for more than 60 years with a general formula (Bi_2O_2) $(A_{n-1}BnO_{3n+1})^{2-}$ [34, 35]. These compounds consist of the regular intergrowth of perovskite-like (A_{n-1} B_nO_{3n+1}) blocks and (Bi_2O_2) slabs, where A is mono-trivalent elements (Na,K,Ca,Sr,Ba,Pb,Bi,etc) allowing for a dodecahedral coordination and Bi tri-pentavalent transition elements (Fe, Ti, Nb, Ta, Cr, etc.) that allow for octahedral coordination. Over the last decade, the Aurivillus compounds have attracted considerable interest due to their magneto-electric properties [36-40]. BTFO is a very complex and complicated structure due to the Gibbs' free energies of formation of differently layered Aurivillus phases. $Bi_5Ti_3FeO_{15}$ can be synthesised by Sol-gel, solid state reaction, and the molten salt synthesis method.

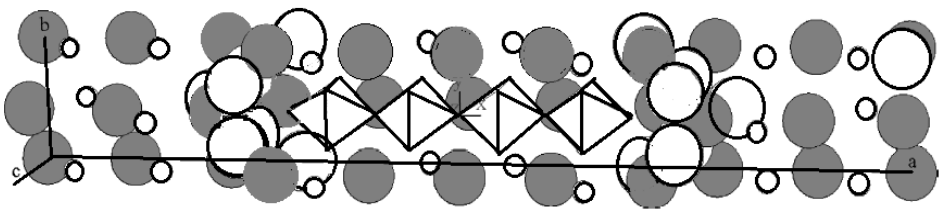

Figure 2.7: The crystal structure of $Bi_5Ti_3FeO_{15}$. Spheres: large white – O; small white – Ti; large grey – Bi. O atoms at the corners of Ti-coordination octahedral omitted.

2.5.4 Barium Lanthanum Titanium Oxide, $BaLa_2Ti_4O_{12}$:

Ceramic materials in the $BaO–Ln_2O_3–TiO_2$ system (with Ln firstly standing for Nd and Sm) have been used to manufacture high frequency ceramic capacitors and microwave dielectric resonators, substrates and other microwave elements. Ceramics with this composition have a high permittivity or dielectric constant and these properties can be optimised by modifying their composition by doping, partial substitution and solid solution formation [41]. Ceramics doped with rare earth were prepared by the soft-chemistry route and a solid state reaction. $BaZr_xTi_{1-x}O_3$ (BZT) is one example of a kind of doped ceramic. Doping ceramics with impure BZT ($Ba_{1-x}Ln_x$)Zr0.2Ti0.$_{8-x/4}O_3$ ($Ln_{¼}$La, Sm, Eu, Dy, Y) is also becoming a common way of improving the electrical properties. These ceramics have demonstrated the effects of different ionic radius rare earth elements on their dielectric properties [42].

2.6 Conventional Synthesis of Ceramic Oxides:

The synthesis of processing solids to the desired structure, compositions and properties continues to be a challenge to chemists, material scientists and engineers. The formation of solids by the ceramic method is controlled by the diffusion of atoms and ionic species through reactants and products and thus requires repeated grinding, pelletising and calcination of reactants (oxides or carbonates) for longer periods (than soft chemical routes) at high temperatures.

The current work of solid state is to enhance the reactivity of materials in order to speed up the reaction kinetics because the rate of a solid state reaction depends on ionic conduction or diffusion within a solid. Solid state diffusion occurs because of temperature, which in turn causes lattice vibrations.

The mole fraction of any particular equation is based on Fick's first and second laws:

$$x = exp\left[-\frac{Ea}{RT}\right] \qquad (2.9)$$

Where Ea is the activation energy required for a particular defect to form, R is the gas constant, and T is the temperature. From this, we find that the number of defects will increase with higher temperatures, which will allow for a rapid diffusion and therefore a higher rate of reaction.

In advanced materials, the first consideration is given to systematic synthesis and control of the structure of the materials to provide a precisely tailored set of properties for demanding applications [43]. It is now recognised that the structure and constitution of advanced materials can be better controlled by the processing method, of which the solid state reaction process, the Sol-gel method, the combustion method, mechanical alloying [44-48], plasma processing , and vapour deposition [49, 50] need to be mentioned.

The conventional method for preparing functional oxides is ceramic-powder-based processing, i.e., through a solid state reaction at high temperatures [51, 52] . This process has disadvantages, such as a high temperature reaction, a limited degree of chemical homogeneity, and low sintering ability. Therefore, over the last few years, several chemically-based processing routes such as freeze-drying [53, 54], spray-pyrolysis [55, 56], sol–gel [57, 58], spray-drying [59], and pyrolysis of complex compounds [60, 61] have been developed to prepare powders with a more homogeneous composition, improved reactivity, and sintering ability at low temperatures. Recently, non-conventional processing methods such as mechanical alloying and mechano-chemical approaches have been used to create reactions between species [62, 63] . However, the reaction kinetics in this method is very slow

and processing takes a long time, which is why recent projects on the base energy storage of super capacitors have needed new high capacitance materials to the improve energy storage properties

2.6.1 Solid State Reaction:

Solid state science is an enormous field of fundamental knowledge and engineering, from mineralogy to quantum physics and from the design of high temperature materials to the development of catalysts. A small part of it is devoted to the study of solid state reactions. A distinction should be made between reactions of the solid state and solid-solid reactions. The first comprises all possible reactions of a solid, from decomposition to catalytic activity. Only one of the reactants needs to be solid. Solid-solid reactions occur between solids only, although reaction products are not necessarily solids.

A solid state reaction, a dry media reaction or a solvent less reaction, is a chemical reaction in which solvents are not used. Solids do not react together at room temperature over normal timescales, they must be heated to a much higher temperature, often 1000ºC to 1500ºC in order for a reaction to occur at an appreciable rate. The factors on which the feasibility and rate of a solid state reaction occur include, the reaction conditions, the structural properties of the reactants, the surface area of the solids and reactivity of the solids, and the thermodynamic change in free energy associated with the reaction [50, 64]. Conventional solid state reactions had been done via the oven technique and the melt technique. In the oven technique, a high temperature was used to encourage reactions without solvents, whereas in the melt technique the reactants melt and then interact in liquid state and a paste which then hardens into a solid. This conventional solid state reaction depends

on the rate of diffusion, which is a temperature dependent process. Thus at higher temperatures the rate of diffusion is higher, which enhances the formation of a new crystalline solid.

2.6.2 Sol-gel Process:

The Sol-gel process is a versatile solution process for making advanced materials, including ceramics and organic-inorganic hybrids. It involves the evolution of inorganic networks through the formation of a colloidal suspension (**sol**) and gelation of the sol to form a network in a continuous liquid phase (**gel**). The precursors for synthesising these colloids consist usually of a metal or metalloid element surrounded by various reactive ligands. The starting material is processed to form a dispersible oxide and forms a sol in contact with water or dilute acid. Removing the liquid from the sol yields the gel, and the sol/gel transition controls the size and shape of the particles. With further drying and heat treatment; i.e. calcination produces dense materials. The Sol-gel method of synthesising nanomaterials is very popular amongst chemists and is widely used to prepare oxide materials.

The Sol-gel process can be characterised by a series of distinct steps:

Step 1: Formation of different stable solutions of the alkoxide or solvated metal precursor (the sol).

Step 2: Gelation resulting from the formation of an oxide- or alcohol-bridged network (the gel) by a polycondensation or polyesterification reaction that dramatically increases the viscosity of the solution.

Step 3: Ageing of the gel (Synthesis), during which polycondensation reactions continue until the gel transforms into a solid mass can take 7 days and is critical for the prevention of cracks in gels that have been cast.

Step 4: Drying of the gel, when water and other volatile liquids are removed from the gel network.

Step 5: Dehydration, during which surface-bound M-OH groups are removed, stabilises the gel against rehydration. This is normally achieved by calcining the monolith at temperatures up to 800^0C.

Step 6: Densification and decomposition of the gels at high temperatures (T>800^0C). The pores of the gel network collapse, and remaining organic species are volatilised. The typical steps involved in Sol-gel processing are shown in the schematic diagram below.

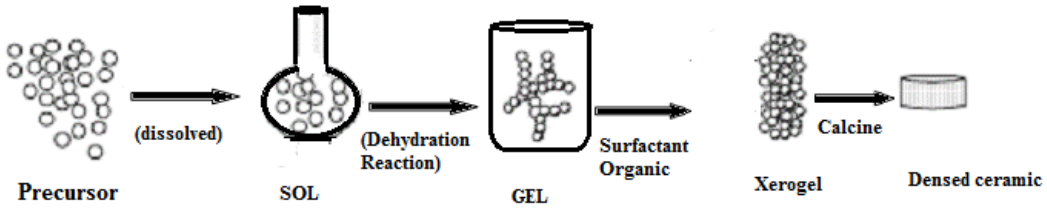

Figure 2.8: Schematic representation of Sol-gel process of synthesis of nanomaterials

Applications for Sol-gel derived products are numerous [65-67]. Ultra-fine and uniform ceramic powder, refractory ceramic, protective coating, thin films and fibre etc. can be produced by the Sol-gel method.

2.6.3 Combustion Synthesis Method:

Combustion synthesis is an attractive technique to synthesise a wide variety of advanced materials such as powders and near-net shape products of ceramics, intermetallics, composites, and functionally graded materials.

Concerning the combustion synthesis of ceramic oxide, the general procedure is to mix metal powder with metal oxides at a proper ratio, and then press them to get the reactant compact. The compact is ignited in an oxidising atmosphere and ceramic oxide products are thus obtained after combustion [68-71]. This indicates that the metal powder is the fuel whereas the oxidising agent is oxygen. Both materials cause combustion and result in a high temperature with phase transformation to obtain the final product. However, the reaction must be conducted under a required oxygen pressure. At this operating point, the metal may melt and then coalescence and grain growth of as-synthesised product may occur due to the combustion reaction arising out of high temperature (about 1400–1600ºC).

Combustion synthesis (CS) can occur by two modes: ***self-propagating high temperature synthesis*** **(SHS)** and ***volume combustion synthesis*** **(VCS).** In both cases, the reactants may be pressed into a pellet which is typically cylindrical in shape. The samples are then heated by an external source (e.g. tungsten coil, laser) either locally **(SHS)** or uniformly **(VCS)** to initiate an exothermic reaction.

2.6.3.1 Self-propagated high temperature (combustion) synthesis (SHS):

Self-propagating synthesis can be used to produce engineering ceramics and other advanced materials [72, 73]. This process, also referred to as CS, provides energy and cost–saving advantages over the more conventional processing route because it is concerned with igniting a mixture of compressed powder, in air or an inert

atmosphere, to produce a chemical reaction, with enough heat released (exothermic reaction) such that it becomes self-sustaining. The temperature of the reaction can be moderated by adding inert salt such as sodium chloride that absorbs heat during melting or evaporation.

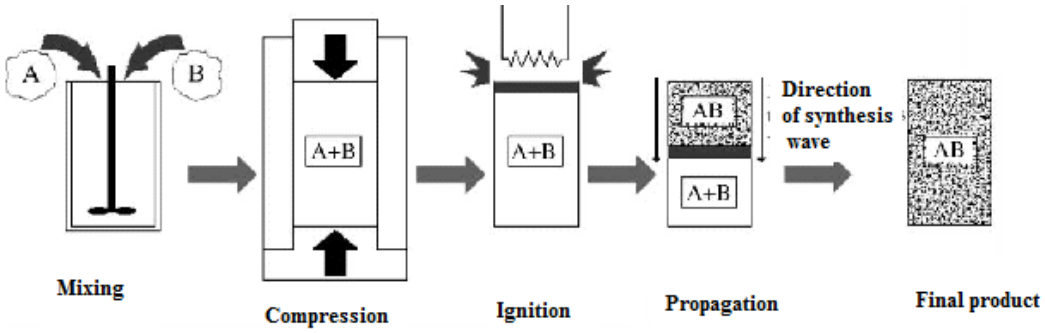

Figure 2.9 a: Schematic representation of SHS process stage

2.6.3.2 Volume combustion synthesis (VCS):

During VCS, the entire sample is heated uniformly in a controlled manner until essentially a reaction occurs simultaneously throughout the volume. This mode of synthesis is more appropriate for weakly exothermic reactions that require preheating prior to ignition, and is sometimes referred to as the ***thermal explosion*** mode. The term explosion used in this context refers to the rapid rise in temperature after a reaction has been initiated, not the destructive process usually associated with detonation or shock waves. For this reason, VCS is perhaps a more appropriate name for this mode of synthesis.

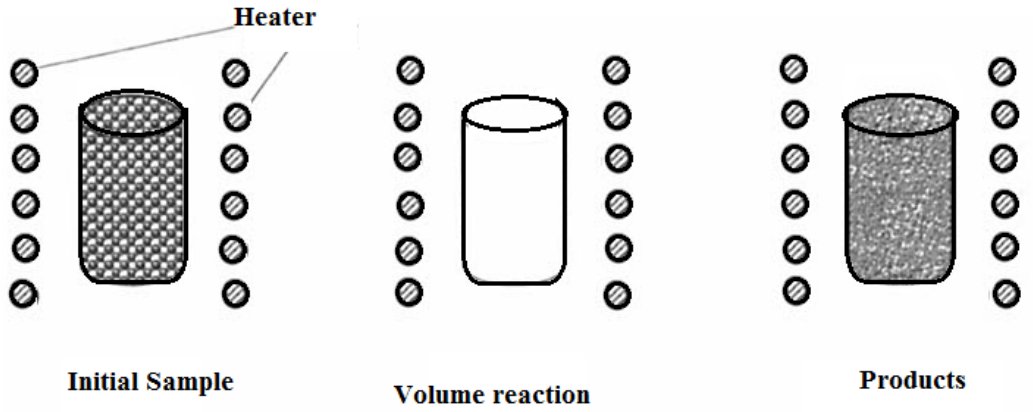

Figure 2.9b: Schematic representation of VCS

2.7 Mechanical Milling:

Mechanical milling is carried out by various devices such as ball, attritor, and vibrational, universal and planetary mills. These mills can use impact or shear fracture modes or a combination of both. This process provides energy to the material being milled. The obvious use of this energy is fracture and the creation of new surfaces such as in grinding and crushing. This energy can also be converted to crystal lattice defects such as dislocations and the generation of heat due to friction. Manipulating the milling parameters to control these physical changes can induce a completing process of plastic deformation and dynamic recovery of the milled material in a manner which produces nano-crystalline particles. This is due to the creation of randomly orientated, high angle grain boundaries within the larger polycrystals [74] . As well as milling parameters, the properties of the material being milled are key determinants in the fracture mode and final particle size and morphology.

Initial particle size is critical because larger particles require less milling energy to facilitate the equivalent reduction in size than smaller particles. This can be understood in terms of the Griffith theory of brittle fracture [75], because internal

flaws must be a critical length to initiate fracture, whereas larger particles are weaker because they are more likely to contain a flaw of critical length .

The melting temperature affects the final crystal and particle size, such that a smaller final grain size can be obtained for particles with higher melting points [76]. This was more accurately attributed to the temperature at which the recovery processes were initiated [76] Recovery works to remove crystal defects such as dislocations and low angle grain boundaries because with further deformation these defects can become high angle grain boundaries [77]. Therefore, recovery is more likely to work against boundary formation in low melting point materials and will therefore produce a larger crystal size. For example, aluminium with a melting point of 660˚C can attain a minimum crystal size of 22 nm while iridium, with a higher melting point of 2446°C can attain a smaller crystal size of 6 nm.

The contamination of powders must be considered during mechanical milling due to contamination in the grinding media and the internal surfaces of the mill housing, as well as any gases within the mill.

There are two terms to denote the processing of powder particles in high-energy ball mills, i.e., *Mechanical Alloying* and *Mechanical Milling.*

Mechanical alloying is when mixtures of powders (different metals, alloys/compounds) are milled together, during which materials transfer to obtain a homogeneous alloy. On the other hand, milling uniform (often stoichiometric) composition powders, such as pure metals, intermetallics, or pre-alloyed powders, where material transfer is not required for homogenisation, has been called *Mechanical Milling* (MM) .

In mechanical alloying some other terms are also used in literature; i.e. reaction milling, rod milling, mechanically activated annealing, double mechanical alloying, and mechanically activated self-propagating high temperature synthesis (MASHS).

Reaction Milling: In this process the powder is milled without any process control agent, but this mechanical alloying process is accompanied by a solid state reaction [78]. *Mechano-chemical synthesis* of materials is the general name given to the process of milling metal powders while chemical reactions occur during milling [79]. Rod milling essentially reduces the contamination of powder during processing, where the balls are replaced by long rods [80] that rotate in a cylindrical vial and exert mainly shear forces on the material.

Mechanically Activated Self-Propagating High- Temperature Synthesis (MASHA) is based on a combination of mechanical alloying (MA) and SHS where the powder mixture is mechanically alloyed to produce a nano-crystalline structure, after which an SHS reaction is initiated by pressing the powder into a pellet and igniting it in a furnace [81, 82] .

2.7.1 Types of Milling:

Different types of high-energy milling equipment are used to produce mechanically alloyed powders.High energy mills use different types of mills; such as **vibrational shake mills** (SPEX), **planetary mills,** and **attritor mills** depending on their different efficiencies and capabilities. Vibrational shake mills use a back-and-forth shaking motion combined with a lateral motion, which gives high ball velocities and impact as well. Its only shortcoming is it provides a small output. In planetary mills, the vial is arranged with a rotating support disk where the vial and rotating support disk rotate in opposite directions. This mill also uses high-energy milling media such as

stainless steel and tungsten carbide. The combined effect can provide a high-energy ball milling. Various types of ferroelectric material can be synthesised by planetary milling. Attritor mills consist of vertical drum and a series of internal impellers arranged at right angles to each other. Three types of impact occur in these mills: between the balls, between the balls and container walls, between balls, while the agitator shaft and impellers make it more efficient for size reduction. This mill can produce large amounts of throughput [81, 83]. Mechanical milling involves using a number of different parameters such as milling materials, milling time, milling speed, ball to powder ratios etc. in different ways [84]. Mechanical milling was carried out for several hours.

2.8 Newly Designed Milling Devices:

Currently, several newly designed mills have been developed for specific purposes. These include redesigned rod mills, vibrating mills from NEV-MA-8, Tokyo, Japan, where the temperature of the milling can be controlled; and the Uni-Ball-Mill from Australian Scientific Instruments, Australia where the nature and impact of the balls in this machine can be controlled by the field strength and the adjustable magnets. In this doctoral project, a Uni-Ball-Mill (Figure 2.10) was used to synthesise high dielectric ceramic powders. Figure 2.10 illustrates how the impact energy in a ball mill is controlled using magnetic grinding media in conjunction with a magnet in the Uni-Ball Mill [85]. During high-energy ball milling there are high temperature excursions at a local level when particles of powder become trapped between the colliding and grinding media, but the extent to which the temperature changes depends on the milling parameters and the powder being processed.

Due to the dynamic nature of ball milling, any local increase in temperature cannot be measured directly. Lohse et al [86], reviewed the work carried out by ten authors who observed temperature dependent phase changes to indirectly determine these localised temperatures; their results range from as low as 50˚ C to as high as 746˚C. This combination of thermal energy, and other phenomena that occur during milling induces the MA of metal powders. The mechanism attributed to MA is repeated welding, fracturing and re-welding of solid powders which leads to alloyed powders with a homogenous composition.

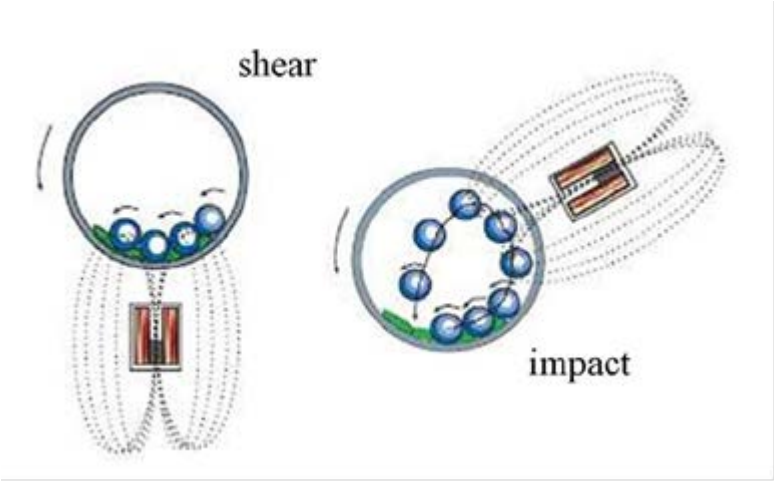

Figure 2.10: Using magnets to influence fracture mode during ball milling

2.9 Reactive Ball Milling:

High-energy ball milling has been extended to activate chemical reactions, a term known as reactive milling or mechano-chemical synthesis [86]. A range of compounds have been synthesised from their element powders such as oxides, nitrides, chalcogenides and semi-metals [87] . Reactive ball milling is unique solid

state processes because reactions which normally require elevated temperatures can be activated at room temperature due to the energy that accumulates as strain defects as well as by a reduction in grain size. These defects shorten the diffusion pathway from bulk diffusion to short circuit diffusion and ultimately reduce the activation energy for the chemical reaction. The activation energy needed to reduce cuprous oxide by metallic iron can be reduced from 575 KJ/mol to 199 KJ/mol by ball milling [88], Figure 2.11 shows how the activation energy is lowered during ball milling.

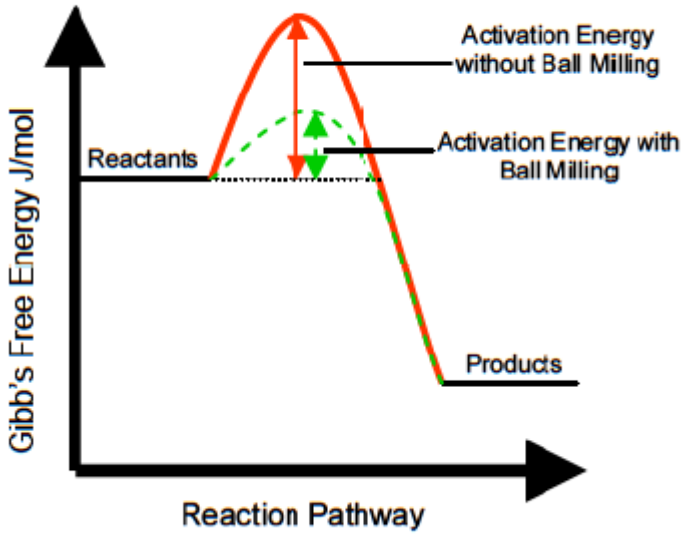

Figure 2.11: Reaction milling reduces activation energy of chemical reactions.

A range of metal oxides have been reduced to their metals by reactive ball milling. These reactions were carried out using displacement reactions of the type shown in Equation 2.10 where metal oxides are reduced by strong metallic reducing agents [87]. This is called a metallothermic reduction. Oxides of copper, aluminium,

calcium, magnesium, titanium, manganese iron and nickel have all been reduced by this method.

$$A_xO + vB - xA + B_xO \qquad (2.10)$$

2.10 Plasma Deposition Method:

Plasma is a gas with a high enough energy content to induce ionisation, with the results that the plasma can conduct electricity and be affected by electromagnetic forces. An ionised species has at least one electron free to move which is not bound to a particular atom or molecule. However, despite containing free charges, plasma is neutral overall [89].

Although plasma usually takes the form of neutral, gas-like clouds, they are also manifested as ion-beams and dusty plasmas, which are plasmas containing charged nano-sized or micro-sized particles[89]. Plasmas are typically formed when gas is heated to a high enough temperature to strip one or more of its electrons. This creates positive and negative particles which are free to move independently of each other within the plasma. Some familiar plasma includes the electric arc in an arc welder, the gas inside a fluorescent light globe, lightning, the sun, stars and polar aurora. Plasma can be classified into two groups; thermal or equilibrium plasmas, which are commonly called “hot” plasmas , and non-thermal or non-equilibrium plasmas which are commonly called “cold” plasmas [89].

By definition, “hot” equilibrium plasmas approach Local Thermodynamic Equilibrium (LTE), which means that the electron temperature (T_e) approaches the temperature of the heavy particle, ion, or gas temperature (T_g) (kinetic equilibrium) while simultaneously approaching chemical equilibrium. In addition, hot plasmas have small field strength to pressure ratio (E/p) which is a measurement of the excess

energy of the electron gas in the plasma, while on the other hand, “cold” plasmas are characterised by large deviations from kinetic equilibrium where Te/Tg ranges from 10 to 100. Additionally, the field strength to pressure ration (E/p) is high [89]. Figure 2.12 graphically demonstrates the difference between hot and cold plasmas. The mean temperature of particles of type I within plasma is related to the mean kinetic energy shown in Equation 2.11 where K is Boltzman’s constant, m_t is the mean mass of the particles i and v_t is their mean kinetic energy [89]. During an elastic collision between an electron and a molecule, the kinetic energy of the molecule increases, while the temperature of the electron is barely affected; this mechanism converts electrical energy to heat energy within plasma. Inelastic collisions modify the internal energy of particles via processes such as excitation, ionisation, recombination, and dissociation.

$$\frac{3}{2}kT_i = \frac{1}{2}m_t v_t^2 \qquad (2.11)$$

Compared to ions and molecules in plasma, the electron mass is small, and therefore if the same force acts on an electron as on an ion, the velocity of electron will be much higher than that of the ion. If the frequency of collision is low, such as at low pressures, this means the average kinetic energy and therefore the temperature of the electrons will be higher than the ions and other heavier particles in the plasma. These are “cold” plasmas where the high kinetic energy of electrons in these plasmas can rupture the molecular bonds while the gases are at an ambient temperature, such as in a fluorescent light globe [89]. Conversely, if the frequency of collision is high, such as at higher pressures, the electrons will have a greater number of opportunities to transfer kinetic energy to heavier ions, thus increasing their kinetic energy and temperature to the extent that at approximately atmospheric pressure, the mean

electron temperature and mean ion temperature are equal. This is a characteristic of "hot" plasma. Ions are formed in hot plasma as the electrons are liberated by the high thermal energies of the molecules and ions. These differences between hot and cold plasma are illustrated in Figure 2.12.

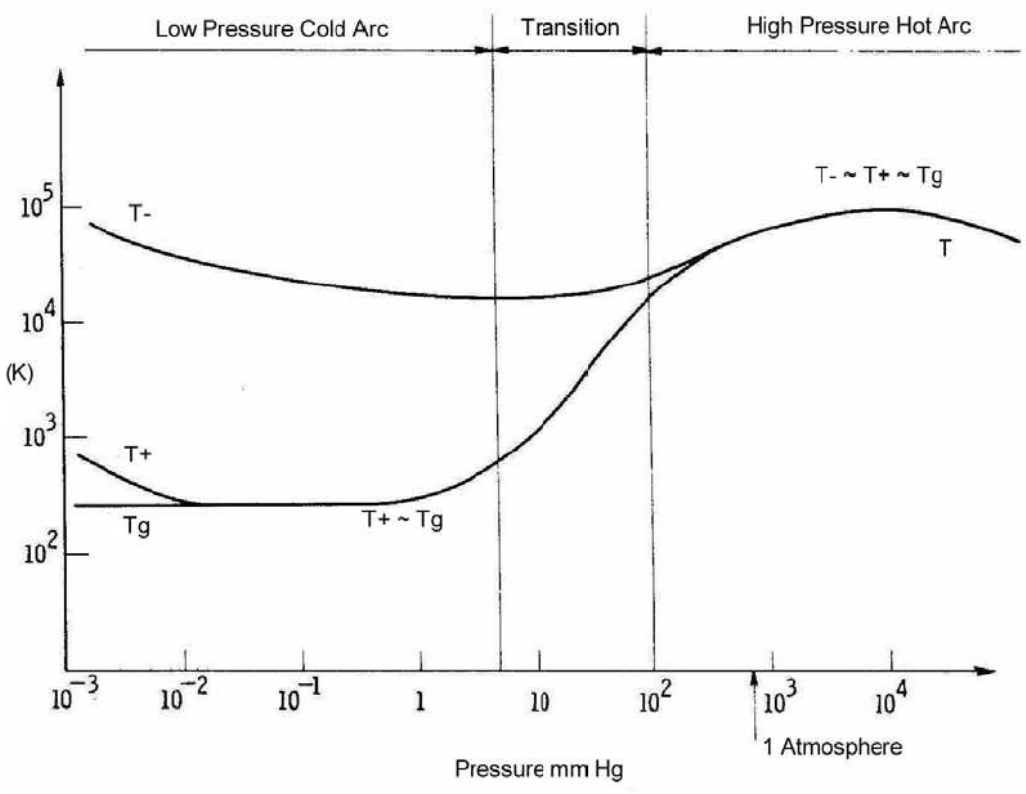

Figure 2.12: Electron, ion and gas temperature as a function of pressure in plasma [90]

Figure 2.12 illustrates the two arrangements by which industrial plasma arcs are initiated;

(a) The non-transferred mode, where the plasma arc is ejected from a torch.

(b) The transferred mode, where the plasma arc is transferred to an external electrode, which may be a molten bath, solid particles or second electrode.

The transferred mode does not require a high gas flow (to force the plasma flame out of the torch), and it also makes use of the Joule Effect to facilitate highly efficient

heating of the anode solid or liquid [91]. The Joule Effect describes how the temperature of a material increases as it conducts electricity.

Figure 2.13: (a) Non-transferred mode arc plasma and (b) Transferred mode arc plasma [91]

Plasma is therefore an ionised gas containing a range of charged particles in a highly energised state. Ionisation in cold plasma is initiated by electrons with high energies that rupture the molecular bonds while hot plasma is initiated by supplying thermal energy to gas molecules. In transferred arc plasma devices the anode material can be Joule heated with energy efficiency.

2.11 Ceramic Oxides in Plasma Environment:

The plasma environment is suitable for ceramic oxide synthesis because the high temperatures available in a plasma force, together with different atmospheric conditions, help to form complex ceramic oxides from metal oxides. The temperature in the plasma chamber could fulfil the energy activation required for a specific complex oxide, and once the temperatures needed to meet the energy required to activate the metal oxide are attained, complex oxides can form the temperatures below the decomposition temperature. However, if the temperature attained in the

process is above the decomposition temperature of the oxides, they will not form because the metal oxide, even if it does form, will decompose once the temperature exceeds the decomposition temperature. The reverse reaction occurs when the temperature is much lower than the decomposition temperature.

To fulfil any specific purpose a new mill can be designed that considers that a high-energy ball mill should have high impact velocities and high impact frequencies, for example, Calka et al. at the University of Wollongong in 2002, designed special high-energy ball mills to produce nano-crystalline materials and amorphous alloys, respectively. EDAMM actually provides kinetic benefits beyond those achievable by only using conventional mechanical milling techniques, but until now the EDAMM technique has mostly been used for metal nitriding, elemental alloying, and rapid reduction processes in various oxides.

It is not necessary to rely upon high temperatures alone to rapidly synthesise materials because non-conventional synthesis methods such as mechanical milling can also accelerate reactions between species at lower temperatures by inducing defects and causing plastic deformation within a bulk material. Shearing and impact forces create numerous fresh and highly reactive surfaces, such that diffusion at these sites is much faster than in the bulk, and therefore represents areas of high diffusivity or “easy diffusion paths”. Synthesis of materials by mechanical milling is far more complex than conventional solid state “mix and heat” methods because they involve multiple reaction mechanism.

Plasma processing is a non-conventional technique used to increase reaction kinetics, and its mechanism is described in the following:

2.11.1 Plasma Processing:

Small solid particles, which possess a surface charge, can also be part of a cold or non-equilibrium plasma. When these particles are in the nano or micro scale this is called dusty plasma; indeed industrial plasma and plasma in space is usually dusty plasma. Within this plasma, the dust may form crystals, clusters, or clouds. This phenomenon is contrary to accepted physics which states these solids should possess a net negative charge and repel each other [92] . Particle attraction can be explained by considering two large negative particles that form a stable complex by collecting a cloud of positive charges between them. Secondary electrons can also be released if the particles are energetic enough, which would make the particle surface positive [92]. Whatever the mechanism of attraction, there are opportunities for a range of particle collisions within dusty plasma to occur such as solid-solid, solid-ion, solid-electron, solid-gas, ion-ion, ion-electron, ion-gas, gas-electron and electron-electron interactions. This provides an opportunity for a range of alternative reaction pathways at potentially lower activation energies. The possible mechanism of dusty plasma is shown in Figure 2.14.

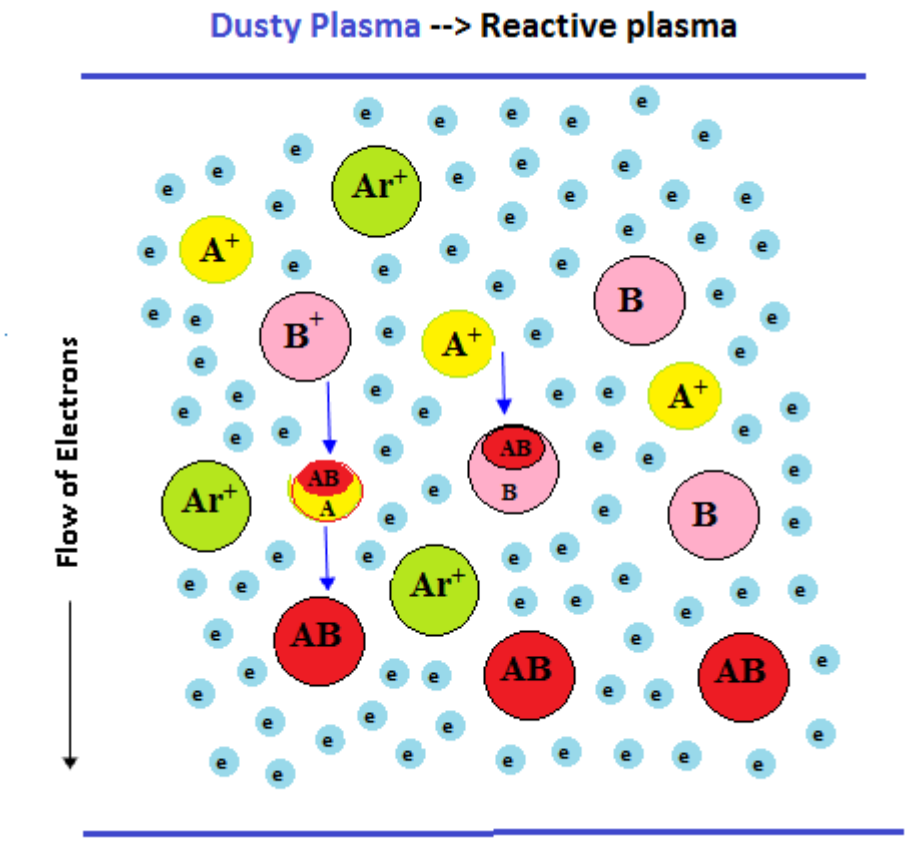

Figure 2.14: Schematic representation of "dusty plasma" developed during EDAMM

EDAMM is a high-energy materials synthesis technique that utilises mechanical milling and plasma processing simultaneously in one process. By using EDAMM, high purity single-phase multi-element oxides can be formed in as little as 0.1% of the processing time required in conventional solid state techniques. Materials can be processed directly from their starting powder whereas the Sol-gel and solid state reaction process consists of multiple steps and have a longer processing time, as shown in Figure 2.15.

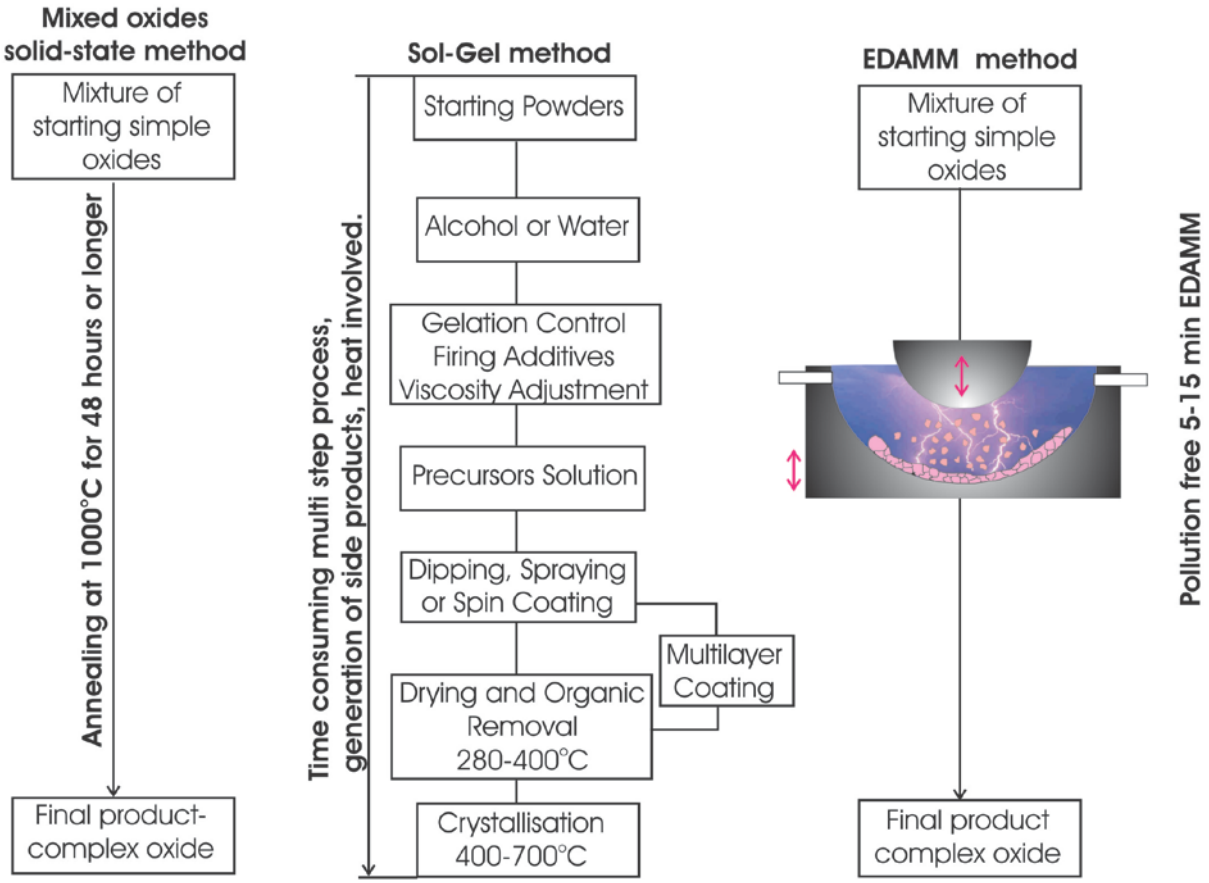

Figure 2.15: Comparison of complex oxides synthesis methods, left: mixed oxides solid state method, middle: Sol-gel method and right: EDAMM method

We used EDAMM synthesised complex ceramic oxides of CCT, BLT, BTF, and $MgAl_2O_4$ within a very short, one-step process, by carefully selecting the electrical (voltage, current, total power) and mechanical (vibration frequency or amplitude) experimental parameters.

CHAPTER 3: EXPERIMENTAL METHODS

3.1 INTRODUCTION

This chapter will describe the experimental procedure, the equipment settings, and the selection and characterisation of the materials.

3.2 Electric Discharge Assisted Mechanical Milling (EDAMM):

. Here we can report the application of a novel Electric Discharge Assisted Mechanical Milling (EDAMM) [93] technique to synthesise various high capacitance oxides. Using EDAMM means that high purity single-phase multi-element oxides can be formed in as little as 0.1% of the processing time required for conventional solid state techniques. We used EDAMM to (i) synthesise oxides from elemental powders by oxidation in oxygen plasma and to (ii) synthesise single-phase multi-element oxides from premixed oxides as starting materials.

However, the original set up of the EDAMM apparatus needed significant alterations, and the power source was redesigned before these functional powders were successfully synthesised.

3.2.1 Description Of Device:

A vibrating laboratory rod mill was modified to a produce a milling where a hardened and curved rod end could repeatedly impact on particles placed on a vibrating stainless steel hemispherical container under a controlled electrical discharge, and in a controlled atmosphere. The reaction chamber was supplied with a steady flow (200 cm^3 min^{-1}) of a selected gas (O_2, Ar, N_2, H_2) via the inlet/outlet valves. During milling, gaps of up to ~ 3 mm, between the vibrating mill bases, the powder particles and the loosely suspended conducting plunger occurred, as shown in Figure. 3.1a. A particular type of electrical discharge was generated within those

gaps. The experiments were carried out using a custom built power supply that was, designed to generate kHz frequency range pulsed arc discharges, of variable energy and duration, superimposed on and a thermal or glow discharge. The arc discharge would locally heat up powders which were subsequently subjected to complex ac plasma treatment (Figure. 3.1a). The pulse current and pulse duration time (in the 20–100 ms range) could be adjusted manually to create a range of electrical conditions, as shown in Figure 3.1b. The main electrical parameters that varied in this study were the current (10–800mA range) and impulse duration time, as shown in Fig. 3.1b. The power supply was connected through an AC high voltage transformer, generating typically up to 3 kV and 10–800mA impulses within the kHz range. A digital camera image of discharge near the milled particles is shown in Figure. 3.1c.

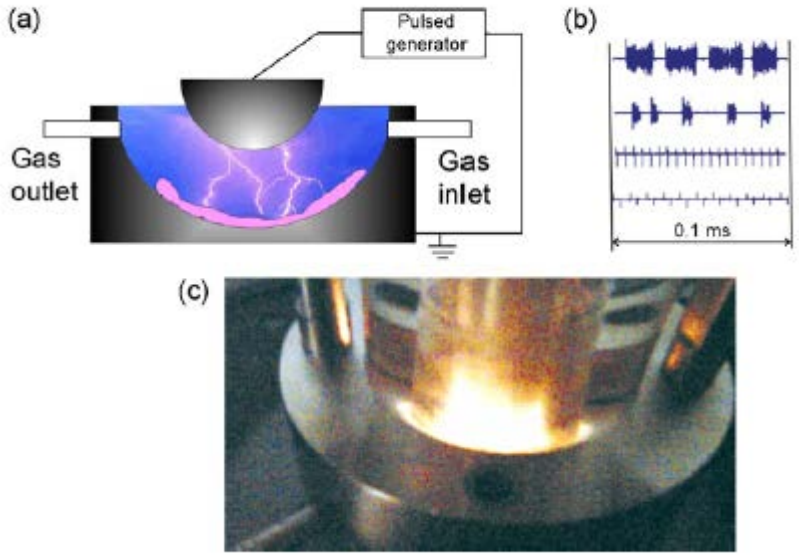

Figure 3.1 : a) Electric Discharge milling cell , b) Spectra of pulsed discharge used in this work , c) photograph of plunger base, perspex shield and mill base during discharge milling

3.2.2 Electric Discharge Assisted Mechanical Mill (EDAMM) Setting:

Experiments were carried out with a suitable spark milling setting to introduce the desired reaction in the powders being processed. The amplitude of the milling base vibration, the current intensity, and the pulse time were the three settings that had to be carried out. To achieve a nano-crystalline structure the following parameters were used:

Table 3.1 : EDAMM settings for spark milling

Starting powder	Atmosphere	Flow	Current Intensity (A)	Vibration amplitude	Current mode	Pulse duration (mins)
BTF CCT $MgAl_2O_4$ BLT	Ar	1-2 Bubble /Sec	1-5	0.5-0.7	AC/DC	5-20

3.2.3 Procedure For EDAMM Milling:

The first step needed to continue with the experiment was to scrub the internal surfaces of the reaction chamber with abrasive paper and ethanol to remove any remaining loose powder or material that had partially welded itself to the milling surface. This was followed by rinsing with ethanol and then drying. When milling a new type of starting powder, the metal milling surfaces were also cleaned using an electric drill with a grinding attachment; this was a necessary step in order to strip the milling cell back to a fresh stainless steel surface by removing the surface layer which had become alloyed with powders during milling.

The volume of the powder is shown in Figure 3.2a, and the powder sample was placed in the milling cell as shown in Figure 3.2b.

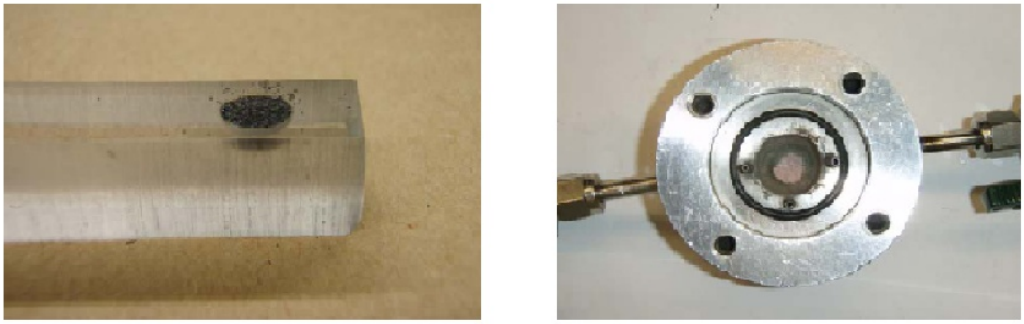

(a) (b)

Figure 3.2: a) Powder measurement b) Milling cell

The milling chamber was maintained at an argon atmosphere and a flow rate of 2 bubbles/sec and to remove air from inside the chamber, it was flushed at least three times. Milling started for 5, 10 or 15 minutes depending on the materials and other parameters such as the vibration amplitude and peak current density. After the milling was completed, the chamber was opened and the milled powders were collected with a clean spatula. These powders were then stored in a sealed glass tube until required for XRD and Scanning Electron Microscopy (SEM) analysis.

3.3 Magnetic Controlled Ball Milling:

The MA method is frequently used in synthesis of complex ceramic materials [46]. The main advantage of this method is the formation of very reactive nano-crystalline powders that could form final products during sintering at much lower temperatures than conventional solid state synthesis [94]. However, the main disadvantage of complex oxide synthesis using MA is contamination from the milling media [95]. The starting powders are simple oxides that are often very hard, abrasive materials that cause excessive wear of the milling media during milling. In most balls milling experiments, the steel balls and vials used became contaminated with iron. In

published papers, levels of contamination from 5 wt % to 6.8 wt % have been reported [96]. In addition, the level of contamination depends on the ball milling device used. In general, higher milling energy causes higher contamination than low milling energy devices [97]. In this study, we proposed a novel approach to reduce Fe contamination while synthesising complex oxides by ball milling. In our method, we replaced hard and highly abrasive oxide starting powders with their metals.

In this work a Uni-Ball-Mill device was used because its parameters such as the milling energy, pattern of ball movement pattern, and shearing to impact ratio [98, 99] was much better. It was a planer-type ball mill consisting of four 25 mm diameter hardened steel balls confined inside a 20 cm stainless steel cell. The typical ball mill charge was 10 g powder. Ball movement during milling was controlled by an external magnetic field 0.3T generated by FeNdB magnets. The maximum pulling force of one 5 mm ball from the surface of the magnet was 70 N. In this work, a 70-150 rpm rotational speed was used, and by adjusting the spatial and/or temporal profiles of the magnet field, the ball trajectories, impact energy and shearing energy can be varied.

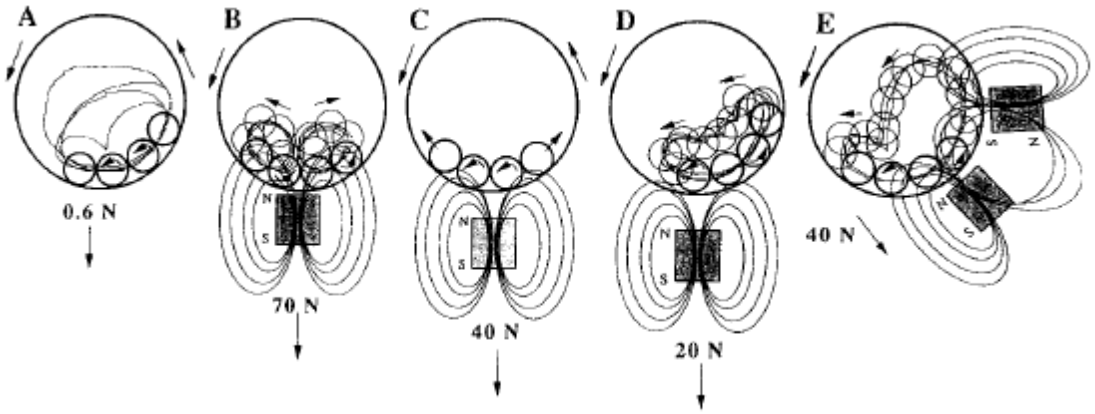

Figure 3.3: Ball trajectories (A,B,C,D and E) generated by different intensity and geometry of magnetic field.

Ball movement without magnetic field is shown in Figure 3.3 (milling mode-A), and indicates that after a number of revolutions the trajectories of individual balls are quite chaotic. At a lower mill speed the balls move along the shell to a point where a component of gravity (on ball weights 0.6 N one ball weights) moves in a parabolic path until it hits the shell, but at a higher speed, the balls begin to centrifuge, so to produce a mostly cascading motion and very little contract between the balls, the mills should be operated at an optimum speed. This is similar to the milling condition presented in Figure 3.3 (milling mode-E) where two magnets are configured with a closed geometry magnetic field that generates a pulling force of 40N on each ball. This force causes the trajectories of the balls to be more uniform, such that they fall at a smaller angle. The balls falling down hit the balls at the bottom that are rotating in an opposite direction, which generates a strong impact and shearing as the balls collide. In this mode, the grinding processes appeared to be controlled mainly by the impact. Interesting ball trajectories can be created by a magnetic field placed at the bottom of the vial (Figure 3.3, milling mode -B, C and D), and by moving the magnet away from the vial, different pulling forces can be generated that dramatically affect the pattern in which the balls move and a maximum pulling force of 70 N pushes the balls up to the central section of the vial that results in a characteristic split in the rotational movement in opposite directions (Figure 3.3, milling mode B). When the pulling force was reduced to 40 N, the balls rotated and oscillated around the equilibrium position at the bottom. The particles of powder trapped between the rolling balls were mostly affected by shearing (Figure 3.3, milling mode-C). A further reduction in the pulling force to 20N created the characteristic ball movements seen in Figure 3.3 (milling mode-D). Here, individual

balls rotated in one direction, while the top balls fell down to the bottom over all the others. This cluster-like structure created a sliding movement which rotated and oscillated up and down, and generated additional shearing between the balls and the vial.

All of these operating modes can have a significant effect on the solid state reactions, the rate of fracturing, ball/ vial wear behaviour, and milling efficiency.

3.4 Materials selection:

The materials and chemicals used during the PhD studies for the synthesis, characterisation and dielectric testing are summarised in Table 3.2. The supplier's details are also provided for reference.

Table 3.2: List of Materials

Materials/Chemicals	Formula	Purity (%)	Supplier
Calcium Oxide	CaO	99.5	Sigma Aldrich, Australia
Copper Oxide	Cu_2O	99.5	Sigma Aldrich, Australia
Titanium Oxide	TiO_2	99.5	Sigma Aldrich, Australia
Barium Oxide	BaO	99.99	Sigma Aldrich, Australia
Iron Oxide	Fe_2O_3	99.9	Sigma Aldrich, Australia
Bismuth Oxide	Bi_2O_3	99.5	Sigma Aldrich, Australia
Magnesium Oxide	MgO	99.5	Sigma Aldrich, Australia
Aluminum Oxide	Al_2O_3	99.5	Sigma Aldrich, Australia
Lanthanum oxide	La_2O_3	99.99	Sigma Aldrich, Australia

Materials/Chemicals	Formula	Purity (%)	Supplier
Magnesium	Mg	99.9	Sigma Aldrich, Australia
Aluminum	Al	99.5	Sigma Aldrich, Australia
Barium	Ba	99.5	Sigma Aldrich, Australia
Iron	Fe	99.5	Sigma Aldrich, Australia
Titanium	Ti	99.9	Sigma Aldrich, Australia
Copper	Cu	99.5	Sigma Aldrich, Australia
Bismuth	Bi	99.5	Sigma Aldrich, Australia
Lanthanum	La	99.5	Sigma Aldrich, Australia

3.5 Sample preparation:

3.5.1 For dielectric measurement:

Samples for dielectric tests were prepared as pellets; synthesised powders were pressed into 6-7 mm diameter and 0.8-1 mm thick pellets. The pellets were then sintered in the air at 900^0C for 24hrs. The as-prepared thick films were sintered in air at 900°C for 24 hours with a slow rise in temperature to avoid cracking. To perform electric measurements, metal electrodes were deposited on both sides of the samples, and the silver paint was used as a metal electrode.

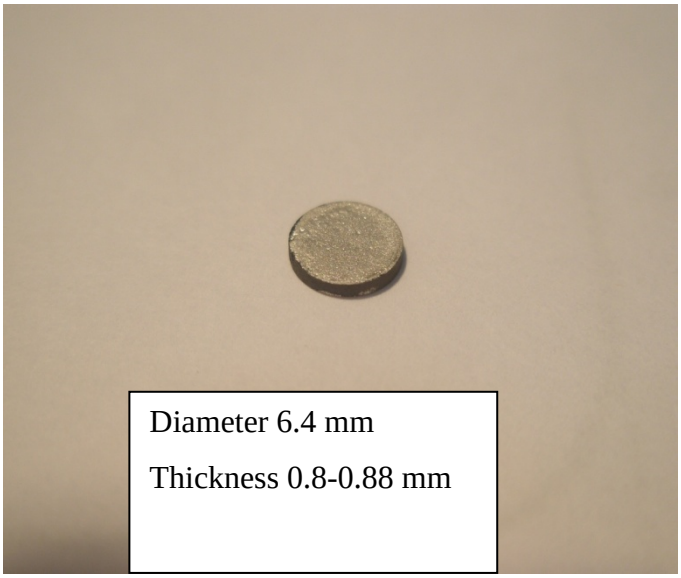

Figure 3.4: Sample of pallet measuring its dielectric properties

3.5.2 For SEM analysis:

SEM was performed using a JEOL (LVSEM) JEOL JSM 6490 with JEOL JED - 2300 EDS and mapping system, and a JEOL 7001 field emission instrument with Oxford instruments X-Max 80 80 mm^2,123 eV SDD energy-dispersive X-ray detector and AZTEC eds and X-ray mapping software. EDS semi-quantitative chemical analysis was carried out using internal machine standards.

Samples for SEM characterisation were prepared either as samples of loose powder or as hot mounted samples of dispersed powders or compacts which were subsequently ground and polished metallographically. All the samples were mounted on a specimen holder with a conduction path via a carbon surface coating. Preparing a loose powder sample was very simple; powder was mixed with ethanol in an aluminium pan which was then dried in an oven at 140°C for 10-15 mins. A very thin layer was shaped on the pan. The sample holder was stamped with sticky tape

and then pressed onto the powder such that it adhered to the tape. These samples were used to observe the morphology of powder in particles.

Grinding and polishing was performed with a Struers metallographic grinding and polishing medium and standard recipes for hard materials. Hot mounting conducting phenolic resin was performed under a pressure of 4200 kpa, and a temperature of 150°C for 8 min. Rough grinding (15 micron and 9 micron diamond) was carried out using MD-Allegro laps. This was followed by coarse polishing (6μm diamond) on an MD/DP-Plan laps, intermediate polishing steps MD/DP –Dur (3 μm diamond), and finally finish polishing with 0.25 μm diamond.

3.5.2.1 Carbon coating:

For imaging in SEM, the specimen must be electrically conductive, at least at the surface, and electrically grounded to prevent an electrostatic charge accumulating at the surface. The samples were plasma cleaned and then mounted on a specimen tub. In this work, all the samples were non-conductive. Non-conductive specimens tend to charge when scanned by an electron beam, especially in secondary electron imaging mode, which causes scanning faults and other imaging artefacts. They are therefore usually coated with an ultra-thin coating of electrical conducting material that has been deposited on the sample. The conductive materials used here are carbon and on some samples, gold.

3.6 Methods of characterisation:

3.6.1 X-ray diffraction (XRD):

XRD is a non-destructive analytical technique which reveals information about the crystal structure, chemical composition, and physical properties of materials and the preferred orientation in polycrystalline or powdered solid samples. The samples can be reused for other tests after XRD analysis. The X-rays are scattered at a characteristic angle by each set of lattice planes and the scattered intensity is a function of the arrangement of atoms in the crystal. This scattering from all the different sets of planes results in a pattern that is unique to the crystal structure of a given compound. The X-rays are generated in X-ray tubes when the anode material (usually copper) is irradiated with a beam of high-energy electrons that is accelerated by a high voltage electric field to a very high speed. In addition, photons with energies are emitted as characteristics of the target material. A monochromator is used to preferentially suppress photons with other energies than the characteristic photon. The X-rays produced are directed at the sample being studied and X-rays with a wavelength from 10 to 0.01 nanometers, which is in the order of the lattice spacing, are elastically diffracted from the atom planes in the crystalline material. Re-emitted X-ray interference gives constructive and destructive interference. Bragg's Law (Eq. 3.1) describes the diffraction condition from planes with a spacing, of *d*:

$$n\lambda = 2d\sin\Theta \qquad (3.1)$$

where *d* is the distance between atomic layers in a crystal, λ is the wavelength of the incident X-ray beam, *n* is an integer and Θ is the angle of incidence experienced by the X-ray beam reflection from the faces of the crystal. Figure 3.5 shows the

interference between waves scattered from two adjacent planes of atoms in a crystal. In this PhD study, only X-ray powder diffraction was used. The powder sample was loaded into a small disc-shaped sample holder with a flattened surface. The sample holder was then placed on one axis of the diffractometer and tilted to an angle Θ, while a detector rotated around it on an arm set at a 2Θ angle. This is known as the Bragg-Brentano configuration where each crystalline solid produces a distinctive pattern of diffraction. Both positions (corresponding to the lattice spacing) and the relative intensities of the lines act to characterise the "fingerprint" for materials. As well as identifying crystalline phases, XRD can also estimate the crystal or crystallite size. This can be obtained from the broadening of the peaks according to Scherrer formula:

$$D = \frac{0.9\lambda}{\beta \cos\theta} \qquad (3.2)$$

Where λ represents the wavelength of X-ray, β is the full width at half maximum (FWHM) and Θ is the Bragg angle.The Scherrer formula assumes zero contribution to lattice strain, equiaxed defect free crystals, and crystallite sizes below 0.1-0.2 μm. More sophisticated formulae are generally employed when these assumptions are invalid. The goniometer was calibrated by performing a test scan on a single crystal silicon plate. All XRD were initially analysed using the Difftech Traces v6 software packages and cross-matched for purity with the international centre for diffraction data (ICDD) database. XRD patterns were collected in a 2Θ configuration using either Philips PW 1730 or a GBC MMA 017 diffractometer (Cu Kα radiation, λ = 1.5418 A^0). The following parameters were maintained and are given in Table 3.2.

Table 3.3:XRD settings for phase analysis

GBC MMA X-ray Diffractometer	
Starting Angle(°)	10
Finishing Angle(°)	100
Step Size(°)	0.05
Scanning rate(°/min)	2
Generator Voltage(kV)	35
Generator Current (mA)	28.5
X-ray Wavelength (nm)	0.154

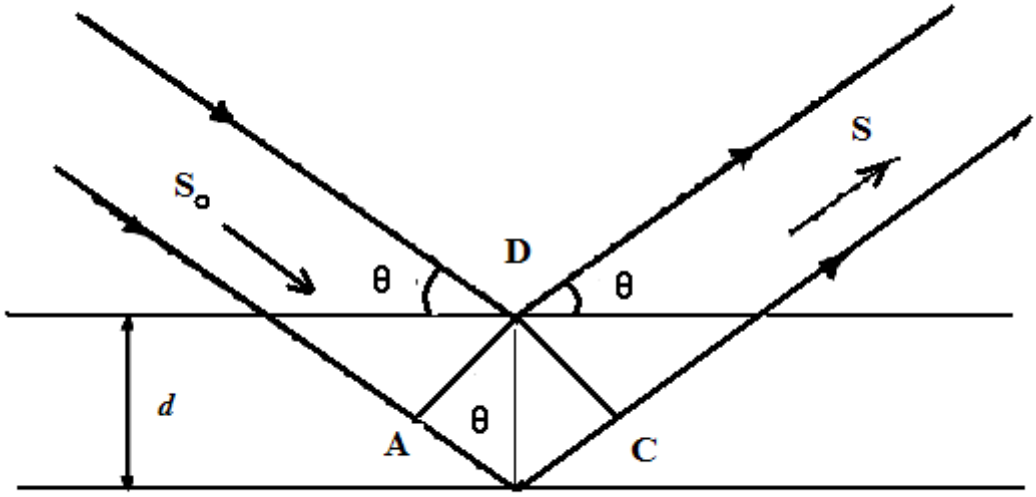

Figure 3.5: Reflection of X-rays from lattice planes according to Bragg's law

3.6.2 Scanning Electron Microscopy (SEM):

A scanning electron microscope is a type of electron microscope that images a sample by scanning it with a beam of electrons in a raster scan pattern. It consists of an electron optical column, a vacuum system and various electronics. The electron gun at the top of the column produces a high-energy electron beam which is focused onto a fine spot on the specimen. Secondary electrons are produced on the surface of

a specimen that is then detected by a suitable detector. The amplitude of the secondary electron signal varies with time according to the topography of the specimen's surface.

During SEM measurements, a sample is bombarded with a scanning beam of electrons that interact with the atoms to produce signals that contain information about the topography, composition and other properties of the sample surface, such as electrical conductivity. The types of signal produced by an SEM include those from the secondary electrons, backscattered electrons (BSE), characteristic X-rays, light specimen currents and transmitted electrons. Secondary electron detectors are common in all SEM. Magnification is totally determined by the electronic circuitry that scans the beam over the specimen's surface. In principle, the resolution of an SEM is determined by the diameter of the beam on the surface of the specimen, but a practical resolution depends on the properties of the specimen, the preparation technique and many instrumental parameters such as beam intensity, accelerating voltage, scanning speed, and distance of the lens from the specimen's surface and the angle of the specimen with respect to the detector. Optimising these parameters into a desirable resolution can be achieved.

Unlike a scanning electronic microscope, a field emission scanning electron microscope produces clearer, less electrostatically distorted images. In this doctoral work both SEM and FESEM were used to analyse the morphology and elemental mapping of the sample. The powder samples were either dispersed in ethanol or directly loaded onto an aluminium holder using carbon conductive tape for SEM observation. The pallet sintered samples were hot mounted onto Bakelite and then

polished and carbon coated for SEM/FESEM analysis. JEOL 7001F field emission SEM with Bruker EDS detection system operating at 30Kev had been used in this work.

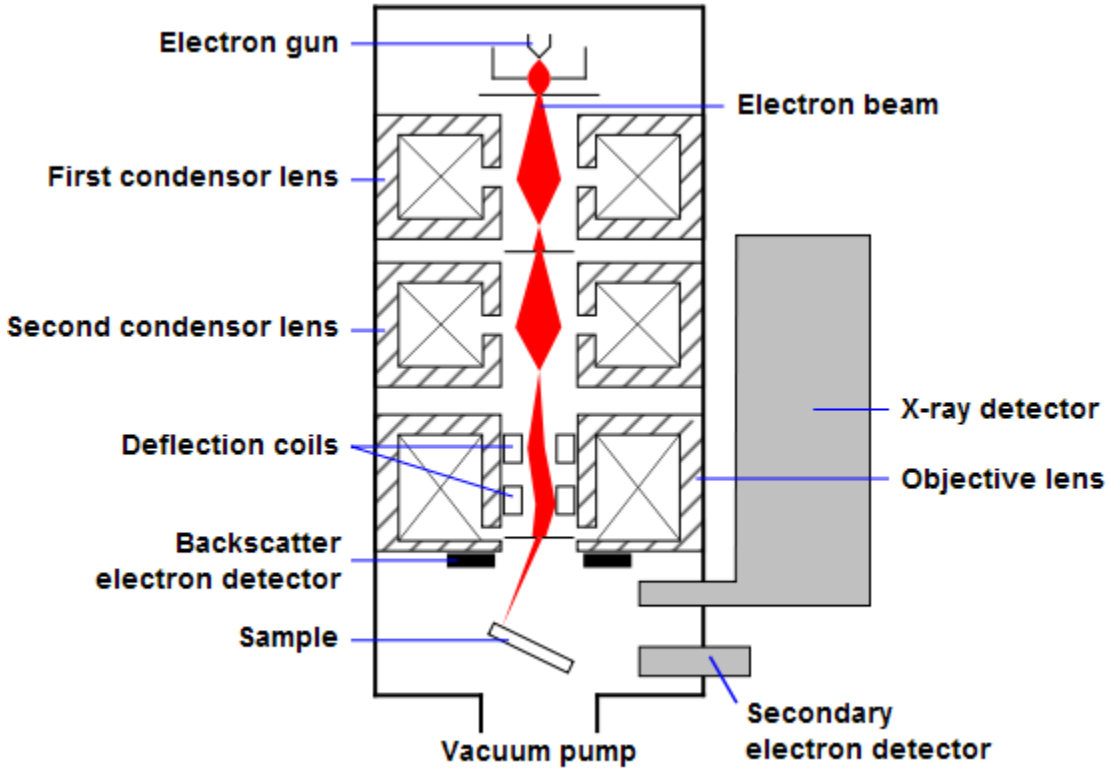

Figure 3.6: Schematic diagram of Scanning Electron Microscope

3.6.3 Energy-Dispersive X-ray Spectroscopy (EDS):

This is an analytical technique used for elemental analysis or chemical characterisation of a sample. Each element has a unique atomic structure that allows for a different set of peaks on its X-ray spectrum. High-energy charged particles such as electrons or protons or an X-ray beam is focused onto the sample to stimulate the emission of characteristic X-rays from the sample. In an unexcited state, an atom

within the sample contains electrons at a discrete energy level, but when an incident beam bombards an atom, an electron in an inner shell is ejected creating an electron hole. An electron from an outer, higher energy shell then fills the hole, and the difference in energy between the higher energy shell and the lower energy shell may be released in the form of an X-ray. The number and energy of X-rays emitted from a specimen can be measured by an energy-dispersive spectrometer. Because the energy of the X-rays is characteristic of the difference in energy between the two shells, and of the atomic structure of the element from which they were emitted, this enables the elemental composition of the specimen to be measured [100].

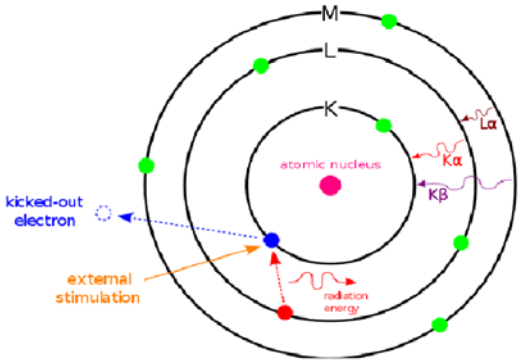

Figure 3.7: EDS phenomena

An EDS system consists of three basic components: an X-ray detector, a pulse processor, and analyser, each of which must work together to achieve optimum results. In practice, an X-ray detector first detects and converts X-rays into electronic

signals, the pulse processor measures the electronic signals to determine the energy of each X-ray detected, and then the analyser displays and interprets the X-ray data.

3.6.4 Transmission Electron Microscopy (TEM):

TEM is a microscopy technique that utilises a high-energy electron beam (e-beam) that is transmitted through an ultra-thin specimen to image the internal structure of a specimen by collecting the signal of the interaction between the specimen and the e-beam. TEMs are capable of imaging at significantly high resolution, owing to the small de Broglie wavelength of electrons. Theoretically, the maximum resolution, *d*, that can be obtained with a light microscope has been limited by the wavelength of the photons that are being used to probe the sample, λ and the numerical aperture of the system, [101]

$$d=\lambda/2n\ Sin\alpha \qquad (3.3)$$

The wavelength of electrons is found by equating the de Broglie Equation to the kinetic energy of an electron, but an additional correction must be made to account for the relativistic effects, because in TEM an electron's velocity approaches the speed of light, *c*

$$\lambda_e \approx \frac{h}{\sqrt{2m_0E\left(1+\frac{E}{2m_0c^2}\right)}} \qquad (3.4)$$

Where, *h* is Planck's constant, m_0 is the rest mass of an electron and *E* is the energy of the accelerated electron.

As electrons pass through a sample, they are treated as being wave-like rather than particle-like, and because the wavelength of high-energy electrons is a fraction of a nanometer and the spacing between atoms in a solid are only slightly larger, the atoms act as a diffraction grating for the electrons. Some electrons will be scattered in particular directions while others continue to pass through the sample without being means that the image on the TEM screen will be a series of spots where each spot corresponds to a satisfied diffraction condition of the sample's crystal structure. If the sample is tilted, the same crystal will stay under illumination, but different diffraction conditions will be activated and different diffraction spots will appear or disappear.

TEM was performed using JEOL 2011 200 Kev Instrument with Jeol eds detection system. TEM samples (EDAMM processed and samples produced by reactive ball milling) were prepared by dispersion of powders onto holey carbon support films.

3.6.5 Dielectric constant measurement: Agilent 4294A was used in this experiment to perform dielectric measurement. The equipment is designed for accurate dielectric constant and loss tangent measurements. It employs the parallel plate method, which sandwiches the material between two electrodes to from a capacitor. Adjustment to insure parallel electrodes is required when using .

CHAPTER 4: RESULTS

4.1 Introduction: This chapter presents and discusses the experimental results obtained from complex oxides processed by EDAMM and controlled ball milling, and via subsequent hot compaction. These results include XRD and subsequent phase analysis using the ICCD PDF database. Selected FESEM and TEM images are also presented in this chapter. The results presented for each complex ceramic material are also interpreted and discussed.

4.2 Synthesis by EDAMM

For the samples investigated, EDAMM was the fastest synthesis route for oxides prepared from elemental ingredients that only required a fraction of the time compared to conventional synthesis methods. The EDAMM technique offers an exciting opportunity to synthesise a range of new and existing materials to be used in a variety of energy storage applications that include rechargeable lithium batteries, hydrogen fuel cells, and super capacitors.

4.2.1 Synthesis of $MgAl_2O_4$

4.2.1.1 XRD results:

Fig 4.3 shows an XRD output from premixed MgO 28.30wt% + Al_2O_3 71.70 wt% (Figure 4.1a) that was discharge milled in argon, nitrogen and helium under DC (Figure 4.1b) and AC (Figure 4.3c) for 15 min. In all X-ray patterns, the strongest peaks can be indexed to the cubic spinel phase: $MgAl_2O_4$. There were also weak

peaks indexed to a small fraction of un-reacted Al_2O_3 and MgO phases.

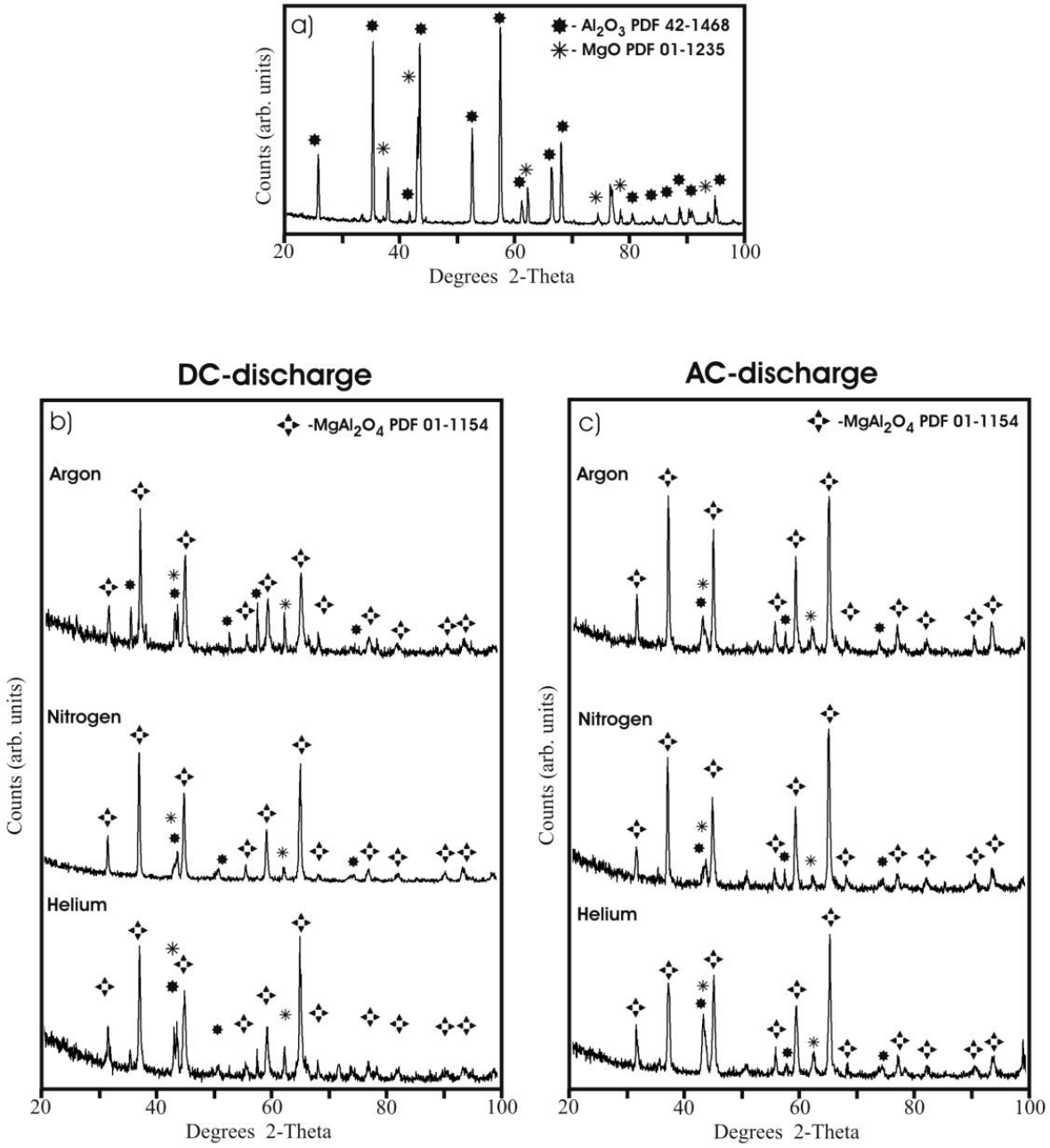

Figure 4.1 XRD patterns of (a) premixed Al_2O_3 + MgO starting powders, (b) powders produced by EDAMM in argon, nitrogen and helium using (b) DC and (c) AC discharges.

Figure 4.2 shows the results of EDAMM of samples milled in oxygen for 15 min. Figure 4.2 a) shows the EDAMM results from premixed Al_2O_3 + MgO. Figure 4.2b)

shows EDAMM results from premixed Al + Mg elemental powders. All the X-ray patterns showed the same set of XRD peaks indexed to the $MgAl_2O_4$ phase, but all the peak positions had shifted to a lower angle compared to PDF 01-1154 which was associated with equilibrium $MgAl_2O_4$. This shift in the XRD peaks indicated the non-stoichiometric character of the $MgAl_2O_4$ phase after milling in oxygen. The calculated lattice parameter of $MgAl_2O_4$ phase after EDAMM from oxides and metals was the same 0.834 nm while PDF 01-1154 stoichiometric value was 0.8075 nm.

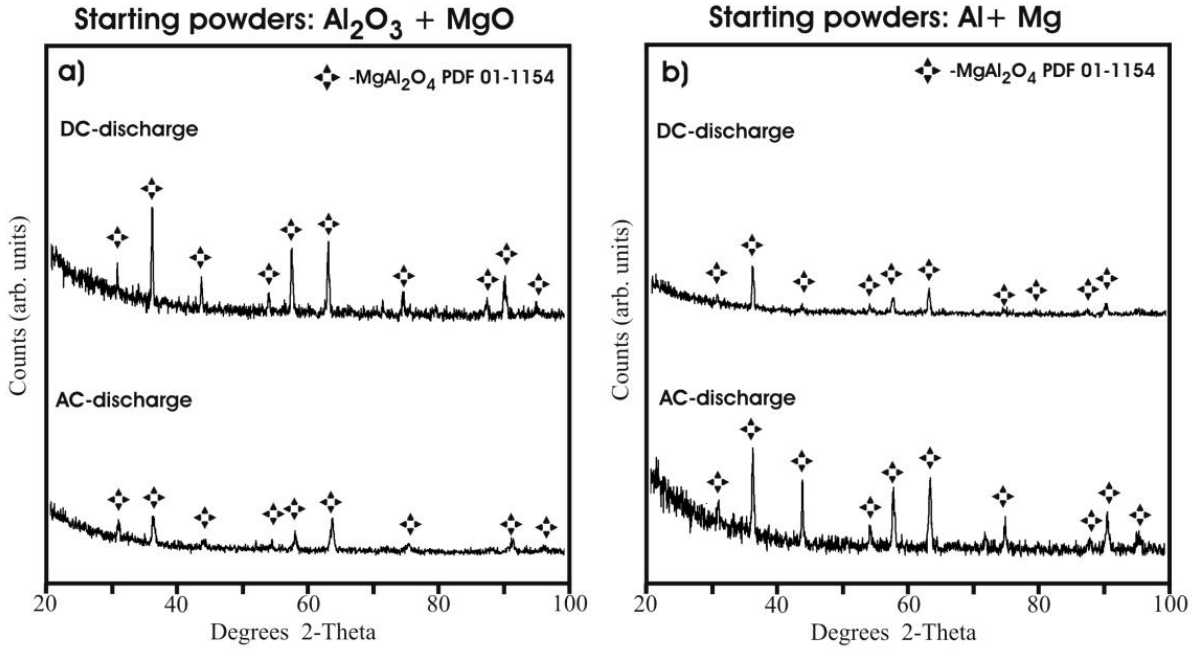

Figure 4.2 XRD patterns of powders produced by EDAMM in oxygen from (a) premixed Al_2O_3+MgO and (b) premixed Al+Mg

4.2.1.2 Scanning electron microscopy

Figure 4.3 shows secondary electron images of particles of powdered $MgAl_2O_4$ after EDAMM in (a) helium, (b) argon, (c) nitrogen and (c) oxygen. A DC milling mode was used. The size of the powder particles after EDAMM in helium and argon

appeared to be almost the same as the particle size range 10- 80 micrometres (Fig 4.3 a, and b). EDAMM in nitrogen resulted in agglomerated particles with sizes close to or above 100 micrometres (Figure 4.3 c). Very large agglomerated particles with sizes larger than 500 micrometres were formed after EDAMM in oxygen (Figure 4.3 d).The distribution of the reaction products within individual powder particles was further examined using an EDS local area analysis. It appears that the distribution of magnesium, aluminium and oxygen was close to stoichiometric composition of $MgAl_2O_4$, although some contamination occurred which was believed to be associated with the mill base or plunger. Measurements from several spots indicated an average value of Fe contamination as follows: after EDAMM in nitrogen 3 wt % Fe, argon 5 wt %, helium 4 wt % and oxygen 24 wt %. The high level of Fe contamination during EDAMM in oxygen was probably caused by excessive oxidation of Fe electrodes; this can be eliminated by replacing the Fe electrodes with graphite electrodes.

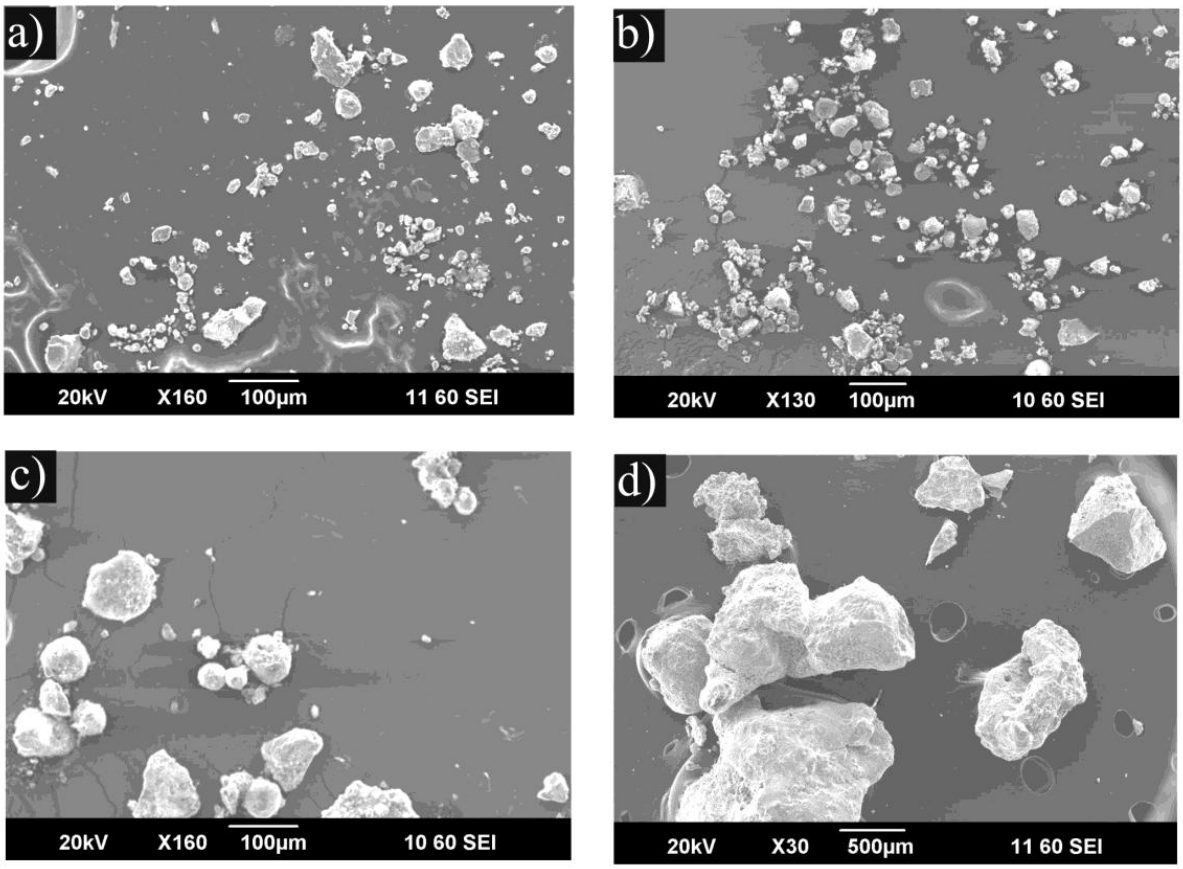

Figure 4.3. Scanning electron micrographs of $MgAl_2O_4$ after EDAMM in (a) helium, (b) argon, (c) nitrogen and (c) oxygen using DC discharges.

4.2.1.3 Dielectric properties: The powder processed in EDAMM in an oxygen atmosphere shows higher dielectric constant and dielectric loss than powders processed in other atmospheres. This occurred because spinel $MgAl_2O_4$ processed in oxygen is more homogenous than when formed by processing in another atmosphere.

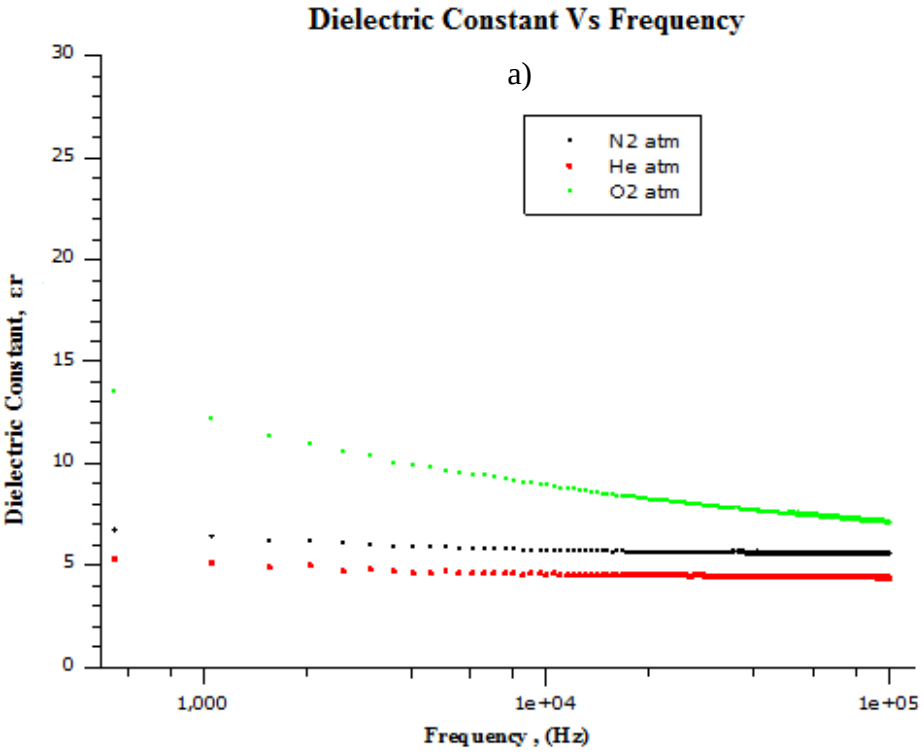

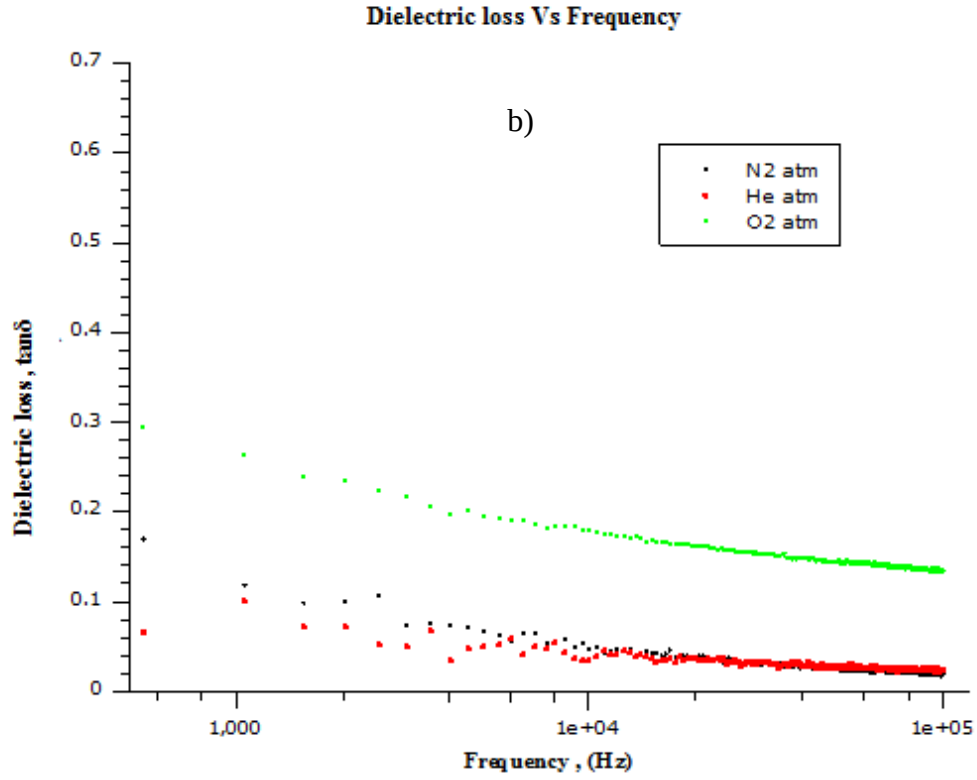

Figure 4.4: a) Dielectric Constant Vs Frequency at different atmosphere, b) Dielectric Loss Vs Frequency at different atmosphere.

4.2.1.4. Discussion

EDAMM combines the benefits of producing fine, highly reactive particles via mechanical milling [102], with an interaction between accelerated ions and powder particle surfaces resulting from the use of electric discharges. During EDAMM, powders are subjected to a localised and intense reaction area characterised by the formation of an electrical discharge and/or plasma with parallel mechanical mixing/milling actions. This process is different from the MA processes previously used for material processing. EDAMM is also different from the popular spark plasma sintering (SPS) used to rapidly sinter ceramic materials and other thermal plasma techniques that have used high intensity arcs (ac or dc) and high frequency discharges (RF and microwave) to synthesise various materials. The phenomena occurring in conventional plasma processes are very complex and not yet fully understood, as is the physics and chemistry of the dynamic plasma generated during the EDAMM process. Moreover, in the current system the powder particles are inside the plasma and in constant motion which makes the process even more complex and so comprehensive theories and models of EDAMM processes are still a long way off. Nevertheless, in the current investigation some fundamental dependencies on processing parameters are established. For instance, Figures 4.1b and c show that the XRD peaks related to an untransformed fraction of Al_2O_3 and MgO were very weak in XRDs from samples milled in nitrogen, but much stronger from samples milled in helium and argon. It can be assumed that the peak intensity is generally proportional to the volume of the phase present in the sample.

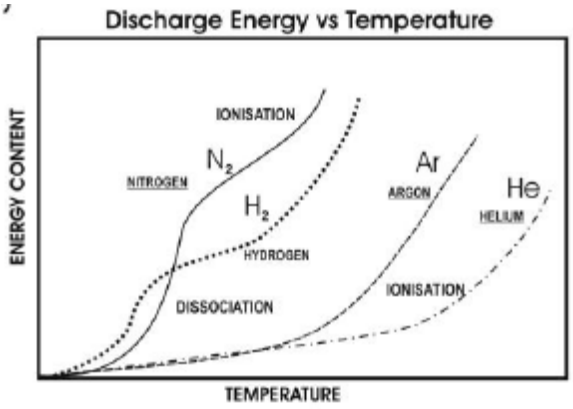

Figure 4.5: Relationship of discharge energy vs discharge temperature.

The plot in Figure 4.5a shows that the discharge temperature in nitrogen was much lower than in argon and helium gases, and the XRD patterns from samples subjected to AC discharges had lower intensities of XRD peaks related to un-reacted Al_2O_3 and MgO phases than the DC discharges. While the temperature associated with an AC discharge is generally lower than for a DC discharge of similar voltage and current, by implication, a lower discharge temperature appears to be better for generating of solid-solid reactions in synthesis of the $MgAl_2O_4$ phase. Although the reactions occurring during EDAMM were poorly understood, the first step in plasma processing is to produce plasma by ionisation where primary ions of a carrier gas are produced, which then transfer excitation and ionisation to powder particle surfaces to produce ions and radicals - the reactant precursors. The plasma flow of gas ions, free radicals and reactant ions bombard the powder surfaces with high-energy and cause local ion implantation. The interaction between the particle surface and the arriving radicals leads to the nucleation and growth of new phases by deep penetration of ions and subsequent diffusion. This localised low heating condition also results in the crystallite size of the reaction products, as shown by the XRD patterns after EDAMM with undeveloped peaks that indicate small crystal sizes – Figure 4.2.

Although the processes that occurred during EDAMM are not well understood experimental results obtained so far indicate that a range of functional oxides can synthesise within minutes.

This result represents a significant advantage over conventional synthesis techniques that are complicated and time consuming. Moreover, EDAMM may facilitate the production of functional oxides for use in energy storage applications that would previously have been thought as impossible to synthesise or to require time consuming preparation.

4.2.3 Synthesis of $CaCu_3Ti_4O_{12}$ (CCT)

4.2.3.1. XRD analysis:

Figure 4.6a) shows an XRD pattern obtained from the premixed starting powders. Figure 4.6b) represents an outcome of EDAMM for 10 minutes in an argon atmosphere, where the absence of XRD peaks indicates the formation of nano-grained microstructure (described in TEM results section in this paper). After 10 minutes of milling in argon, an x-ray diffraction pattern (Figure 4.6c) shows well-developed XRD peaks that can be indexed to the pure Cu phase (PDF001-1241). This implies that extending the milling process in argon caused a reduction of CuO which resulted in the formation of Cu. Figure 4.6d) shows the XRD pattern obtained from the sample milled for 10 min and sintered at 1000°C for 24 hours. Here, all the XRD peaks can be indexed to the $CaCu_3Ti_4O_{12}$ phase (PDF021-0140), thus during sintering, the back-oxidation and formation of homogenous $CaCu_3Ti_4O_{12}$ was observed. The estimated crystal sizes based on the Scherrer formula of the CCT after sintering synthesised in Argon atmosphere were as follows; using the (2 2 0), (3 2 1), (4 0 0), (4 2 2), (4 4 0) peaks respectively; 53.77nm, 11.86 nm, 50.88 nm and

71.44 nm, 41.41 nm, (average 54.37 nm). The variations in results for the different peaks can be affected by a number of factors. These include lattice strain, which is assumed to be fairly small for oxide ceramics, and also by the presence of extended defects such as dislocations in layered materials, antiphase boundaries and stacking faults. Stacking faults, in particular are commonly occur perovskite layered structure [103, 104].

By maintaining the same process parameters i.e. impulse mode, electrical condition and gas flow rate, the premixed powder was EDAMM in an oxygen atmosphere for 10 minutes (Fig 4.6e). The diffraction pattern was indexed to $CaCu_3Ti_4O_{12}$ (PDF 021-0140). Grain size estimates applying the Scherrer formula for this sample indiced values of greater than 100 nm, consistent with SEM observations presented in Sect. 4.2.3.3.

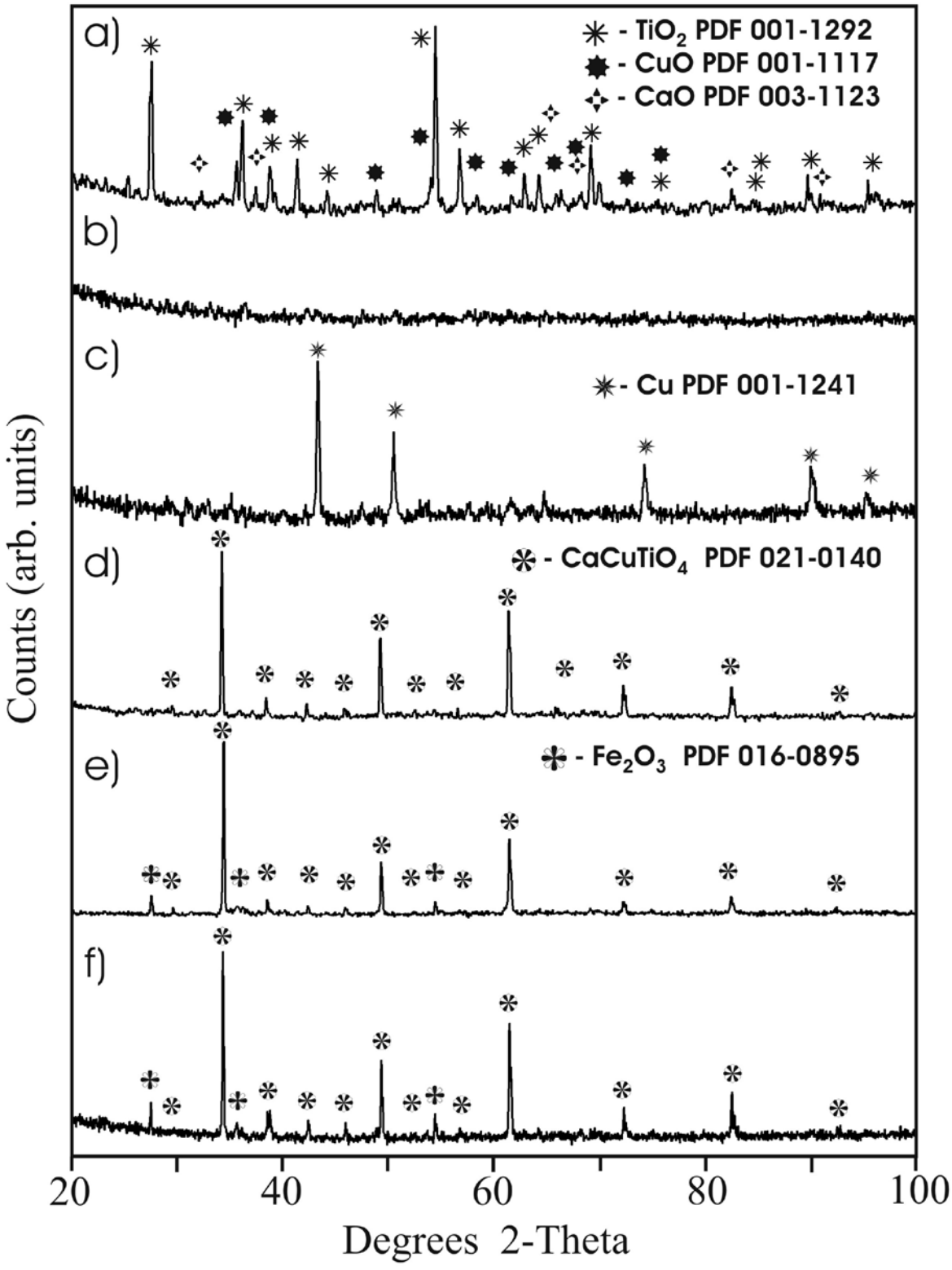

Figure 4.6 XRD patterns of (a) premixed TiO_2+CuO+CaO starting powders, (b) sample produced by EDAMM after 5 min in argon (c) after 10 min (d) after sintering for 24 hours (e) sample produced by EDAMM after 10 min in oxygen (f) sintering for 24 hours after O_2 milling.

During milling in oxygen plasma, a one-step transformation to the CCT phase from premixed powders occurred, and these grains were fully developed after sintering. All the XRD peaks after EDAMM in oxygen for 10 minutes and sintering at 1000^{o}C for 24 hours were also indexed to $CaCu_3Ti_4O_{12}$ as shown in Figure 4.6f. The CCT prepared by this process showed a well-developed crystalline structure but in both cases, these were trace amounts of Fe_2O_3. This was believed to be a result of contamination associated with the formation of debris from the mill base and plungers, and subsequent oxidation during EDAMM processing in oxygen plasma.

4.2.3.2 TEM analysis:

Preliminary TEM analysis of the CCT sample after EDAMM processing for 10 minutes (Fig 4.7) in argon confirmed the formation of a fine nanostructured product, previously indicated by broadened XRD peaks (4.6c). The microstructure shown in the TEM bright field image consists of nano-crystals that are ~ 5nm in diameter on average. The inset selected area electron diffraction (SAED) pattern of the area (Fig 4.7) contains very diffused spotty rings that are consistent with the formation of nano-crystalline or mixed nano-crystalline/amorphous products. The region in the figure was located over a hole in the wholly carbon support. The diffused diffraction rings of small dots are consistent with the nano-crystalline or mixed amorphous/nano-crystalline character of this product. Moreover, the microstructure revealed in the associated TEM image also includes nano-crystals ~5 nm in average diameter.

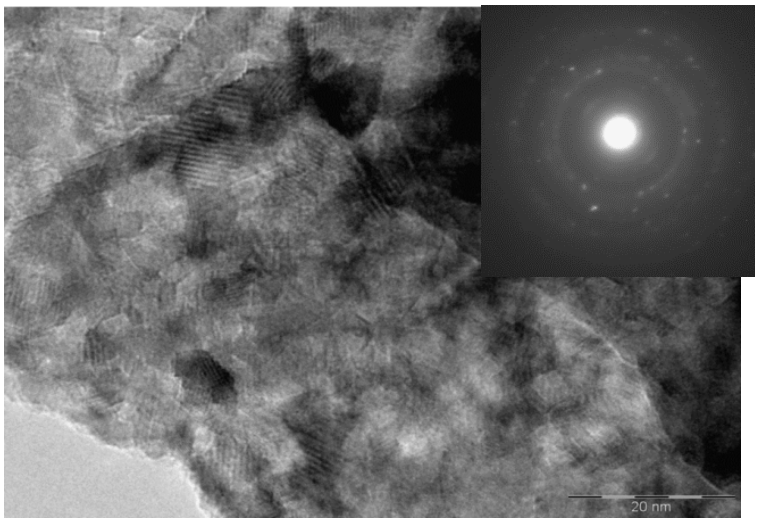

Figure 4.7: TEM of CCT revealing fine nano-crystals in as milled sample, ~5nm size, Inset SAED pattern contained very fine spotty rings plus extremely diffuse diffraction contrast

4.2.3.3 FESEM analysis of sintered products:

Figure 4.8 shows SEM backscattered images of sintered samples that were prepared by EDAMM processing in (a) argon and (b) an oxygen atmosphere, followed by pressing and sintering in air at 900ºC. Unlike the as-milled samples, the sintered samples showed significant coarsening and densification, with product grain sizes now in the sub-micron range. Inspection of micrographs shown in Figure 4.8a) and 4.8b indicate the differences in grain sizes from region to region.

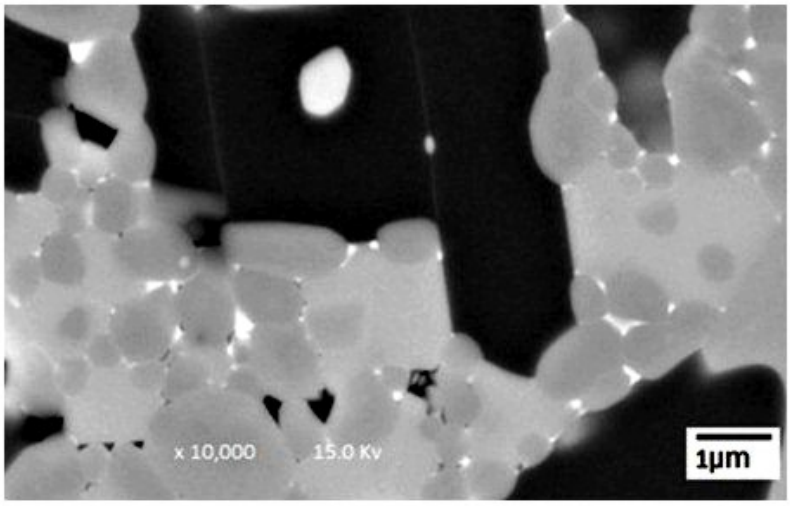

Figure 4.8a): SEM image of CCT processed in Ar, sintered at air for 900°C.

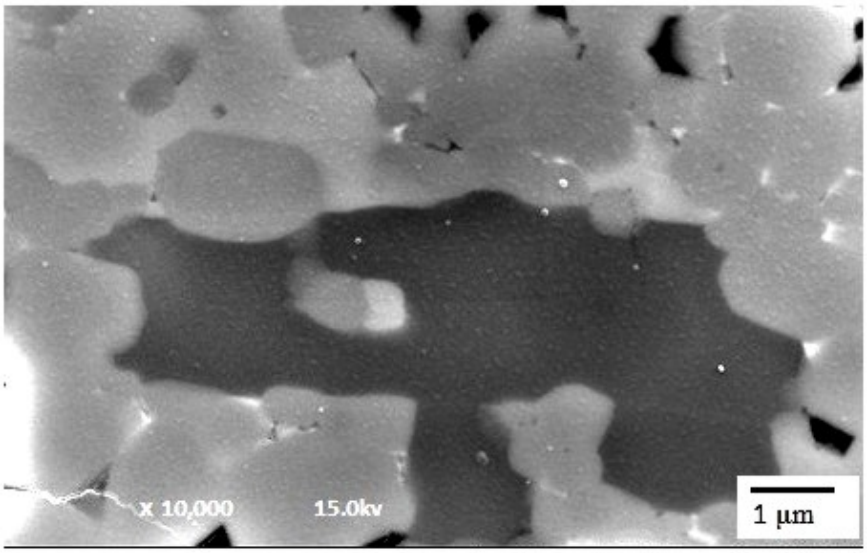

Figure 4.8b): SEM image of CCT processed in O_2, sintered at air for 900°C

EDAMM processing in an Ar atmosphere was believed to facilitate the reduction of CuO to Cu which, during sintering, turned to CuO again. Most of these CuO particles sit on grain boundaries, as indicated by the bright regions in Figure 4.8a (and confirmed by EDS spot analysis).

4.2.3.4 Dielectric properties:

The temperature dependencies of the permittivity (Ɛr) and dielectric loss (tanδ) for the samples synthesised from EDAMM processing in Ar and O_2 plasma atmosphere are shown in Figures 4.9a) and 4.9b) respectively, show that the temperature greatly influenced on the dielectric properties of CCT, indeed the dielectric behaviour of both samples were almost similar. As the temperature decreased, there was a step-like decrease of Ɛr (T) in both samples, but as the temperature increased, the dielectric constants shifted to higher values while the DC resistance decreased. This phenomenon is consistent with the rapid drop in the dielectric constant at low temperatures due to the carrier freezing in the semi-conducting region within the crystal.

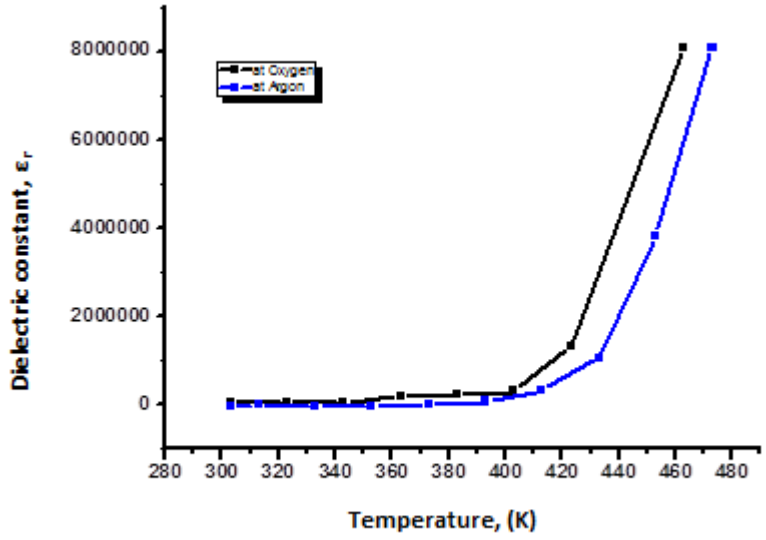

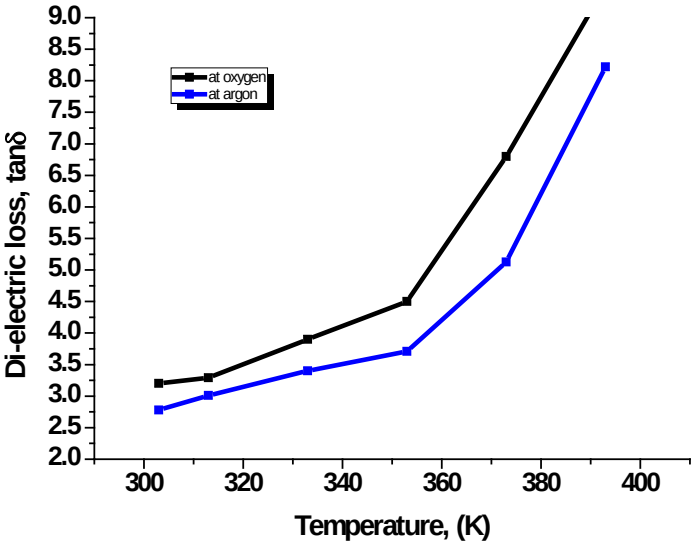

Figure 4.9 a) Temperature effect on dielectric constant at 50 Hz. b) Temperature effect on dielectric loss at 50 Hz.

The frequency dependence of the dielectric constant for $CaCu_3Ti_4O_{12}$ ceramics at room temperature after EDAMM in argon and oxygen is shown in Figure 4.11. The frequency used in this paper was up to 100 KHz. The nature of change of the dielectric constant with frequency decreased monotonically whereas the dielectric loss value decreased initially, and then remained constant with variations in

frequency. This behaviour by tanδ is depicted in the model proposed by Goswami and Goswami [105].

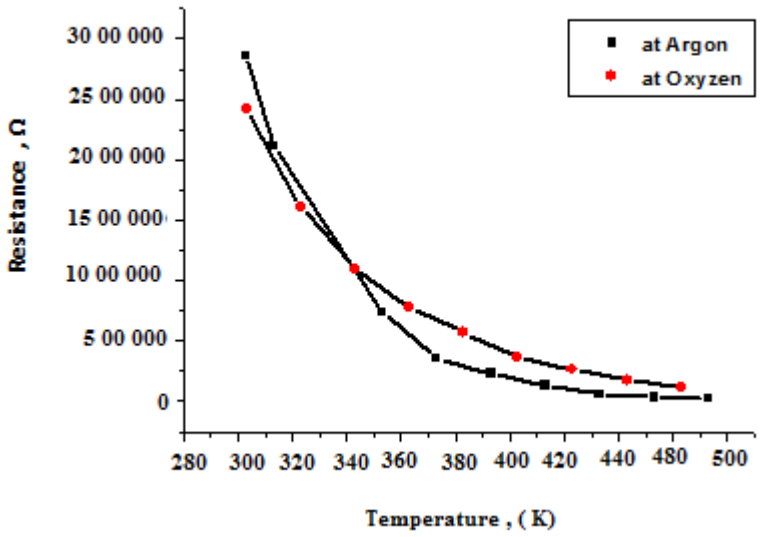

Figure 4.10: Temperature effect on DC resistance at 50 Hz.

Variations in the dielectric constant with frequency for CCT processed in O_2 plasma was higher than CCT processed in Ar. Similar trends occurred in the case of dielectric loss.

Therefore pallets of CCT that were prepared through the EDAMM method have a very high dielectric constant and low dielectric loss, which is appropriate for many applications such as a super capacitor.

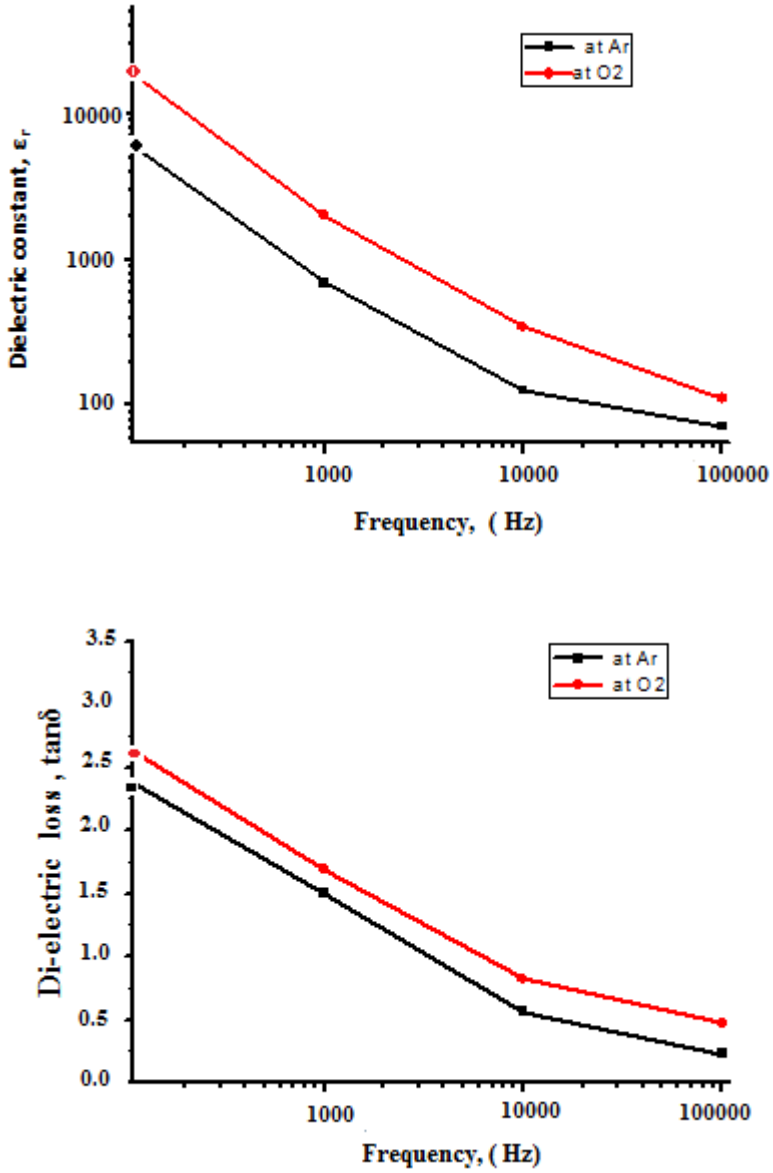

Figure 4.11: Frequency dependence of dielectric permittivity and dielectric loss of CCT processed in Ar and O_2 atm.

A summary of the dielectric properties of the CCT samples is shown in Table 4.1. Here, the CCT processed in oxygen plasma has a higher dielectric constant (ε_r = 48018) value than CCT processed in argon plasma (ε_r =13000) at 50 Hz, while the capacitance and dielectric loss have similar values. However, the CCT pellet DC resistance measured at 50 Hz for the sample processed in oxygen plasma was lower

than the sample processed in argon plasma. The CCT glued sample has a low dielectric constant (ε_r=136) and low DC resistance.

There are many materials with high dielectric constants in nano-crystalline form, but processing them at high temperatures may cause recrystallisation and a loss of their beneficial properties [106]. In these cases, polymer glue can used to consolidate the nano-crystalline powder. A review of published papers shows that the dielectric constant of polymer-ceramic powders ranges from 49-86 [106], whereas in our experiment the glued sample had a comparatively higher dielectric constant Ɛr= 136.

Table 4.1: Comparisons of properties at different conditions

Sample	EDAMM in Ar	EDAMM in O2	Glued Sample
DC resistance, Ω	2.7 MΩ	2.03 MΩ	1.6 MΩ
Dielectric Constant, ε_r	13,000	48,018	136
Capacitance,C	3.68 nF	7.1 nF	14.04 nF
Dielectric loss, tanδ	2.5	3.11	0.54

4.2.3.5 Discussion:

Assuming a Debye-like relaxation described by the model in [107] our dielectric measurement data for this sample was found to be in agreement with this model and indicates that the dielectric response in such a material was associated with mobile charge carriers inside the grain. However, the charge carriers were probably responsible for a dielectric response due to the presence of Cu^+ inside the grains [107]. Backscattered images combined with EDS analysis from the sample EDAMM processed in O_2 revealed that many of the grain boundaries were rich in copper, and presumably conductive. This enrichment of the grain boundaries by Cu occurs via the following mechanisms:

1. The O_2 plasma is better at transforming from a starting powder to CCT because some of the starting CuO powder was reduced to Cu.

2. During subsequent processing, much of the Cu reoxidised, although some grain boundaries were not heated enough to become reoxidised.

3. During subsequent hot pressing a sample pellet was produced which contained grain boundary copper.

CCT processed in O_2 showed a higher dielectric constant than CCT processed in Ar, as Table 1 shows. The explanation can be given in terms of the larger grain size of the sample processed in O_2 where the density of the current path within small grain was less than the larger grains, which indicated that larger grains have a larger density current path. Because CCT processed in O_2 has a larger grain size, it may affect the origin of the high dielectric constant [108], because the content of Cu increased, there was a subtle increase in the grain size [109]. CCT processed in O_2 plasma has areas dominated by Cu, making the phenomena of a large grain size cause larger density of the current path.

4.2.4 Synthesis of $Bi_5Ti_3FeO_{15}$

4.2.4.1 XRD studies of $Bi_5Ti_3FeO_{15}$:

The crystal structure of three samples was investigated using XRD with Cu Kα radiation, but to identify the crystalline phases of each sample, the diffraction peaks shown in Figure. 4.12 were analysed based on the powder XRD patterns. The XRD analysis revealed that the sample obtained by sintering from elemental metal contained single $Bi_5Ti_3FeO_{15}$ (ICDD PDF 38-1257) and the strongest diffraction peak of BTF ceramic was (119), which accords with the highest diffraction peak in the Aurivillius phases [110]. There was also significant peak broadening after synthesising from EDAMM, and after sintering the peak widths become narrower, which indicated a good crystalline structure. Quantitative crystallite size estimates were not made because the size ranges were above that applicable to Scherrer formula.

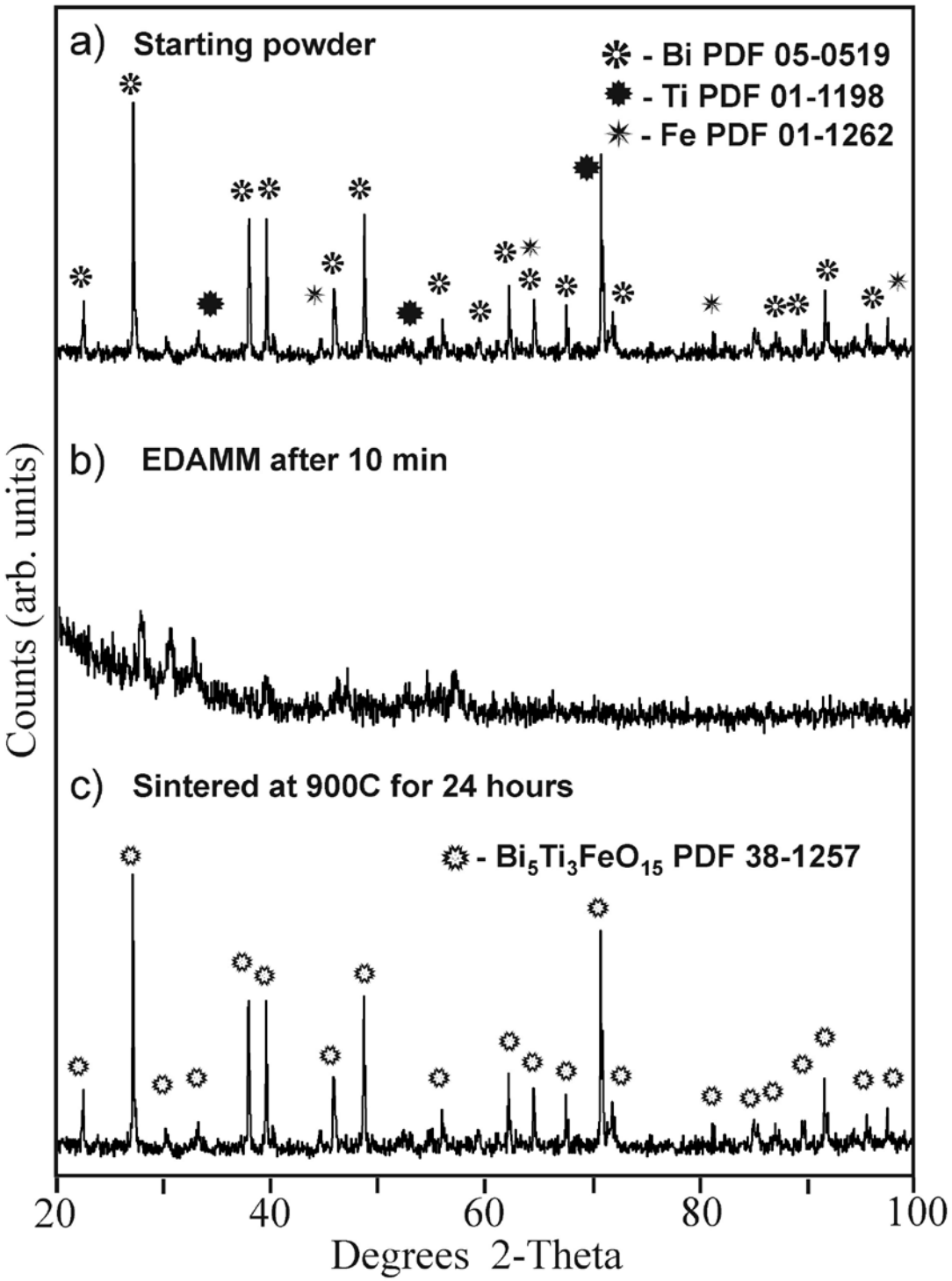

Figure 4.12: XRD patterns of a) Bi+Ti+Fe starting powders, b) sample produced by EDAMM after 10 mins in oxygen atmosphere c) sintering for 24 hours after O_2 milling.

The XRD analysis revealed that the sample obtained by sintering from elemental oxides contained $Bi_5Ti_3FeO_{15}$ (ICDD PDF 82-0063) and $Bi_2Fe_4O_9$ (PDF 20-0836).

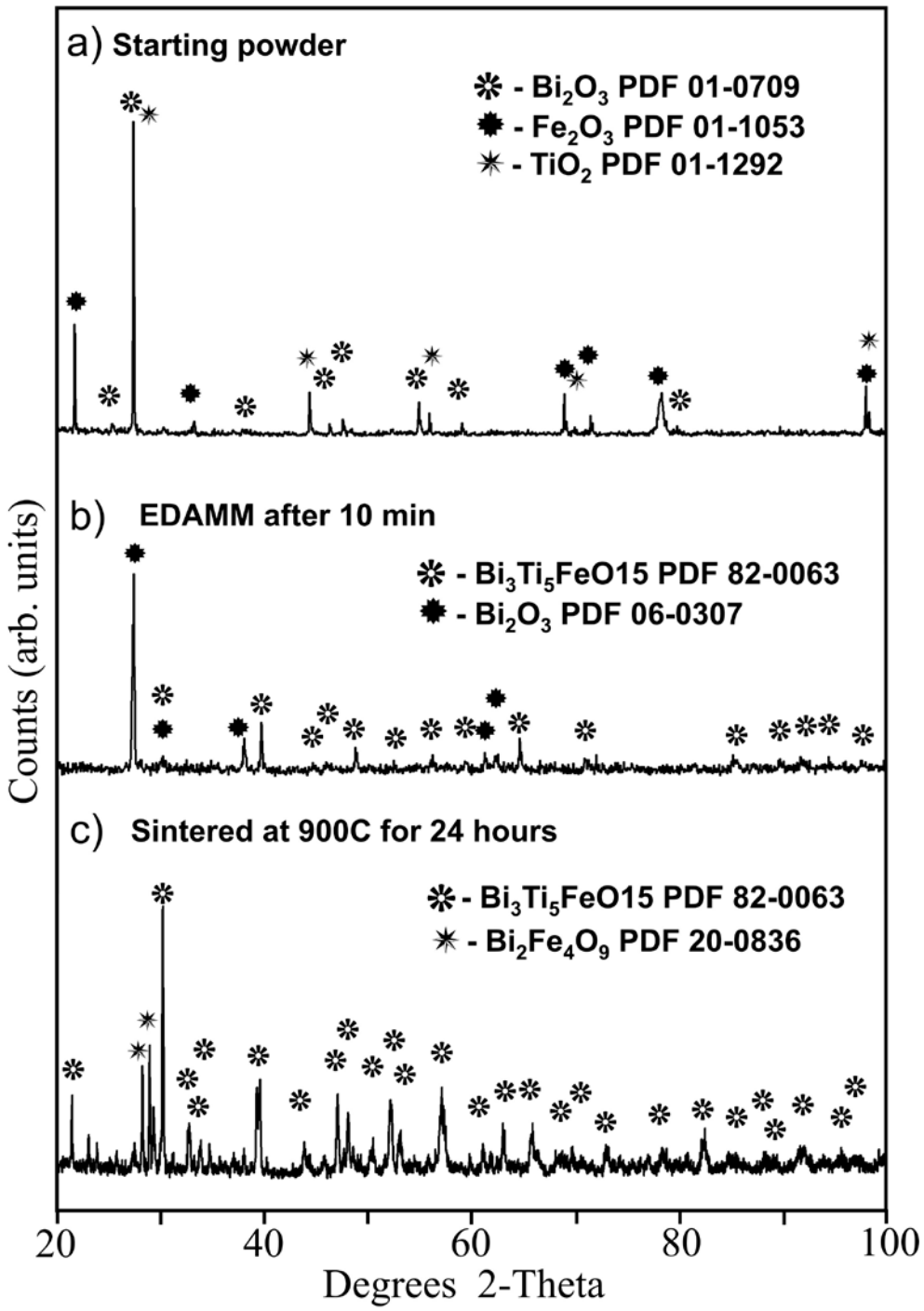

Figure 4.13: XRD patterns of a) Bi_2O_3+TiO_2+Fe_2O_3starting powders, b) sample produced by EDAMM after 10 mins in oxygen atmosphere c) sintering for 24 hours after O_2 milling.

4.2.4.2 TEM analysis:

As with CCT, preliminary TEM investigations revealed rapid microstructural refinement during the early stages of EDAMM processing of powders in oxygen. Figures 4.14 and 4.15 show the TEM results obtained from the $Bi_5Ti_3Fe_{15}$ that were EDAMM processed for 2 mins and 5 mins in O_2 respectively.

After 2 mins of EDAMM processing, the elemental powders had broken up and agglomerated into composite particles containing predominantly relatively large crystals, as indicated by the spotty SEAD patterns insets in Fig 4.14 (a and b), and by the contrasting lattice fringe in Figure. 4.14c). After 5 mins of EDAMM processing, a mixture of spotty rings and much diffused diffraction contrast was observed (Figure 4.15 a)) with HTREM, while Figure 4.15(c and d) indicated a mixed product consisting of a mixture of crystals (~10-40 nm average diameter) and an amorphous phase.

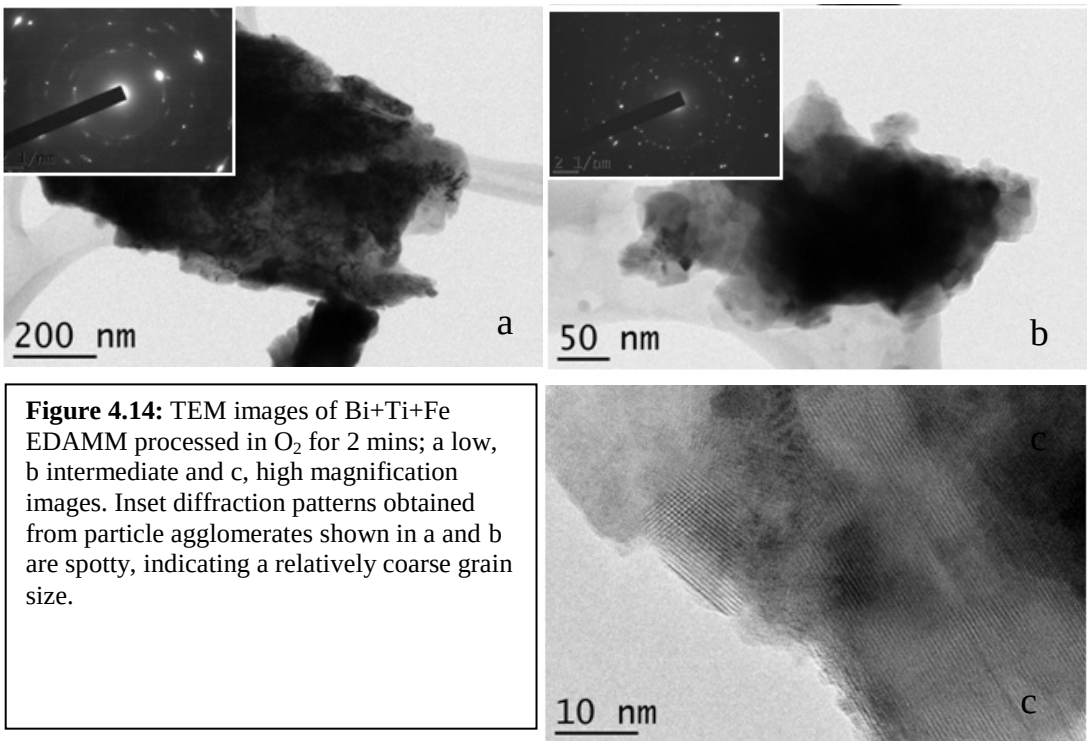

Figure 4.14: TEM images of Bi+Ti+Fe EDAMM processed in O_2 for 2 mins; a low, b intermediate and c, high magnification images. Inset diffraction patterns obtained from particle agglomerates shown in a and b are spotty, indicating a relatively coarse grain size.

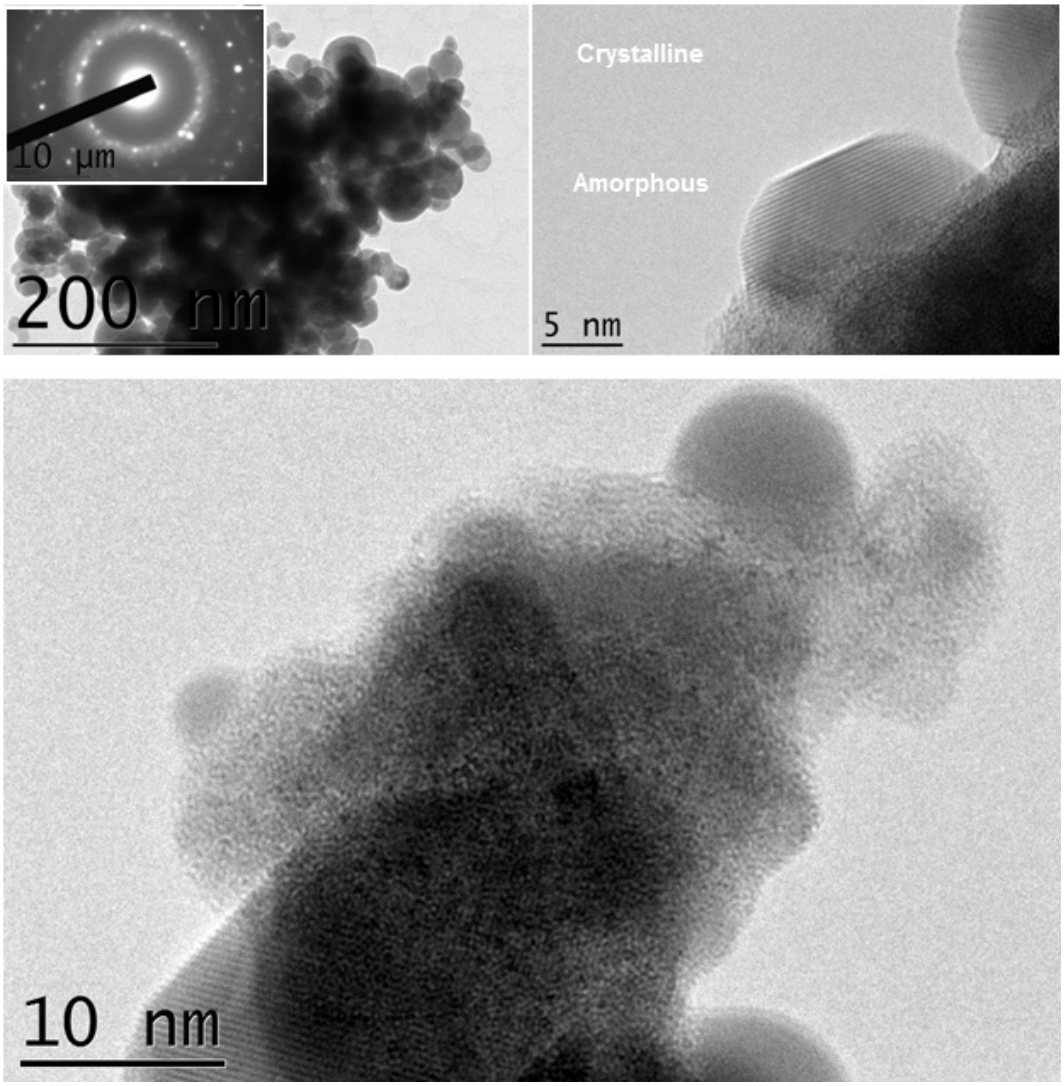

Figure 4.15: TEM images of Bi+Ti+Fe EDAMM processed in O_2 for 5 mins. Inset SAED pattern obtained from region in (a) indicates a mixed crystalline (spots) and amorphous (diffuse ring) structure. HRTEM images (b) and (c) revealed contrast consistent with the formation of the two distinct structures, as indicated

4.2.4.3 FESEM analysis of sintered powders:

The evolution of the microstructure in the $Bi_5Ti_3FeO_{15}$ products was investigated using SEM, and shown in Figures 4.16 - 4.18. All the micrographs revealed a distinct plate-like morphology of a phase that was identified by XRD to be $Bi_5Ti_3FeO_{15}$, which was typical of layered compounds belonging to Aurivillius phases. The samples synthesised from elemental oxides showed a product consisting of dense aggregates of both rounded and elongated plates and platelets. The more equiaxed

and clearly visible platelets are between 1-3 μm, whereas the samples synthesised from elemental metals were more homogenous with a few plate-like particles.

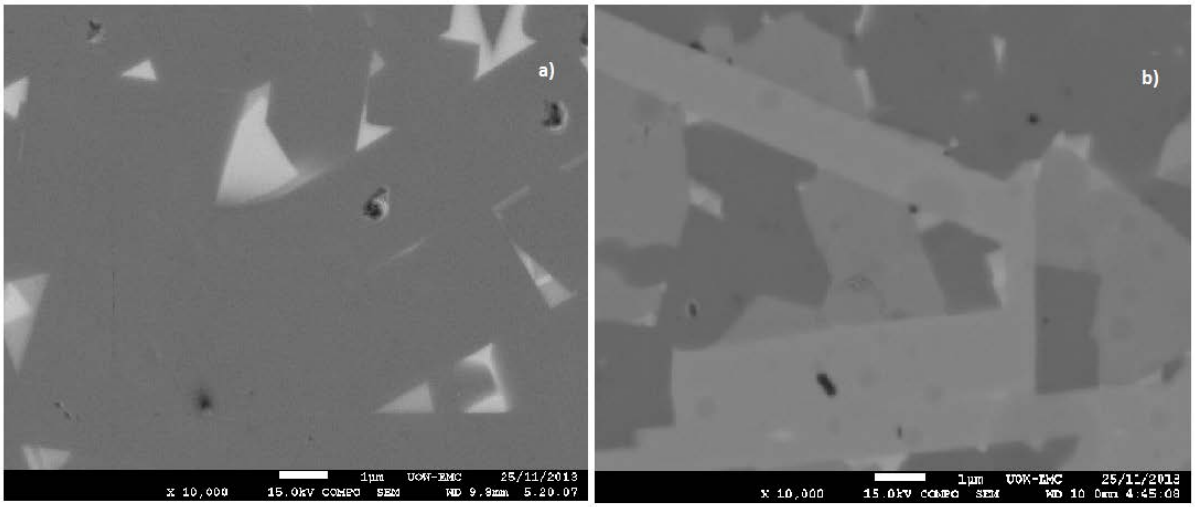

Figure 4.16 : a) from elemental metal. b) from elemental oxides.

4.2.4.4 EDS analysis:

The EDS spectra shown in Figure 4.17 and Figure 4.18 and Table 4.2 and Table 4.3 confirmed the presence of constitute elements in the sample with a standard analysis indicating a ratio of Bi , Ti , and Fe that were very close to the stoichiometry of $Bi_5Ti_3FeO_{15}$. The BTF pellet from metal was more homogenous than the BTF pellet from oxide pellet. As Figure 4.17 shows there are different regions in the oxide pellet. An EDS analysis of the pellet prepared from the oxides' starting powder, and then XRD analysis confirmed there were some bismuth iron oxide particles in the BTF oxide pellet.

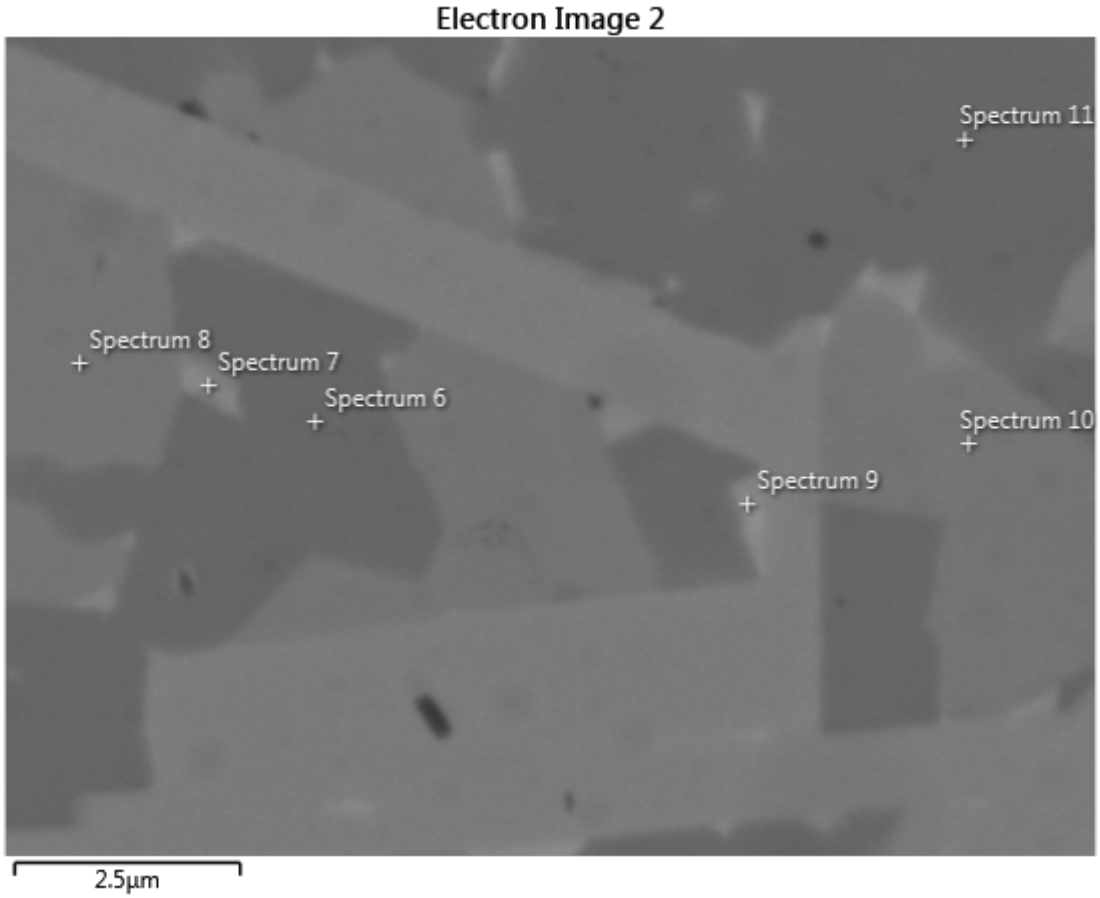

Figure 4.17 : EDS spectrum analysis of BTF pellet prepared from elemental oxides.

Table 4.2: Spot analysis of BTF pellet prepared from elemental oxides

	Bi (wt%)	Fe (wt%)	O_2 (wt%)	Ti (wt%)	Mn (wt%)	Cr (wt%)	Al (wt%)
Spectrum 6	60.4	14.6	11.8	8.7	1.7	1.5	1.3
Spectrum 7	72.2	10.1	10.2	3.9	1.2	1.6	0.9
Spectrum 8	87.1	2.3	8.5	1.1		1.0	
Spectrum 9	81.2	4.5	9.4	2.6	0.8	0.8	0.6
Spectrum 10	68.8	5.2	10.5	8.7	1.1		
Spectrum 11	60.7	15.6	11.6	7.1	1.6	1.6	

The EDS shown in Figure 4.18 confirms that the pellet prepared from elemental metal and sintered for 24 hours at 900ºC had a more homegenous structure consisting of $Bi_5Ti_3FeO_{15}$ with BiO_2 particles.

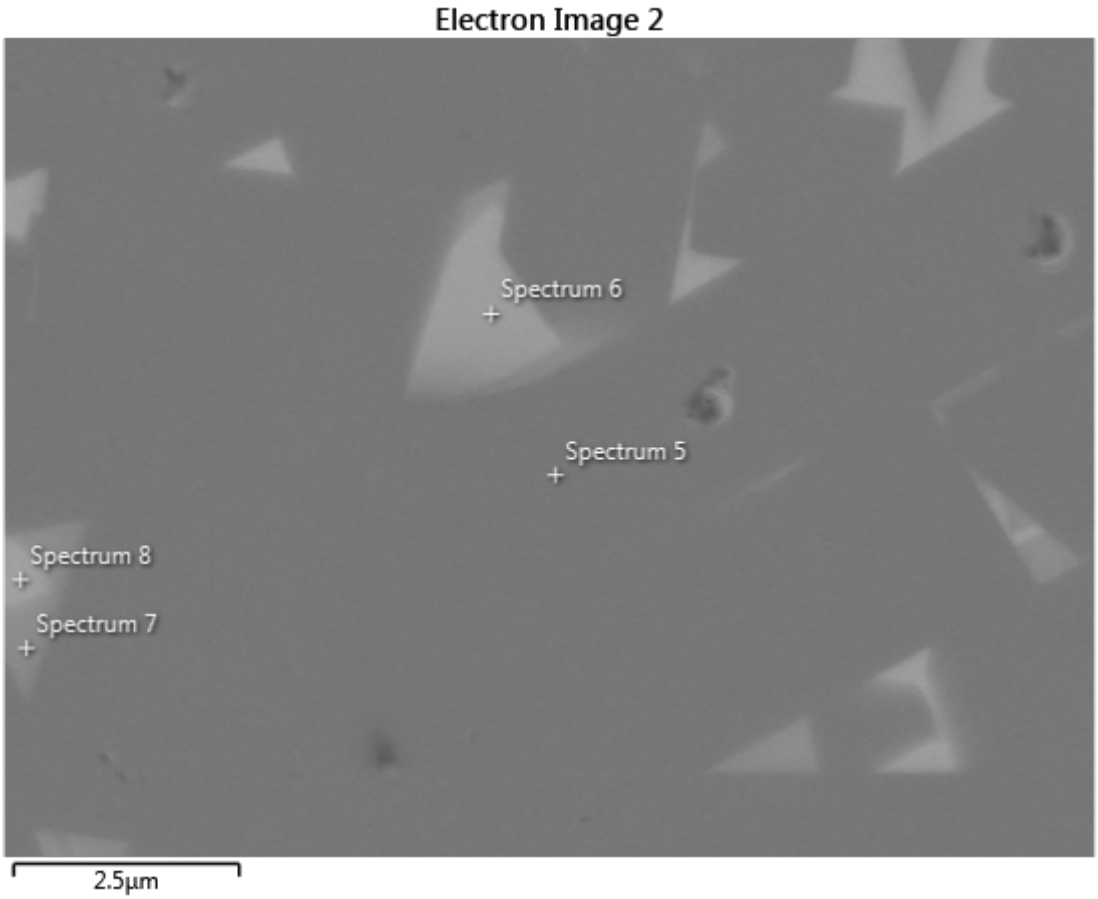

Figure 4.18 : EDS spectrum analysis of BTF pellet prepared from elemental metals.

Table 4.3: Spot analysis of BTF pellet prepared from elemental metals

	Bi (wt%)	Fe (wt%)	O_2 (wt%)	Ti (wt%)	Mn (wt%)	Cr (wt%)
Spectrum 5	59.8	15.2	11.3	9.8	2.2	1.5
Spectrum 6	84.3	3.8	8.1	2.1		1.6
Spectrum 7	75.4	8.0	11.2	4.2	1.3	
Spectrum 8	87.1	2.3	8.5	1.1		1.0

4.2.4.5 Dielectric properties:

The dielectric properties of the material were characterised with dielectric constants (ε_r) and the loss tangent (tanδ), with the results being shown in Figures 4.19-4.23. The effect of frequency and temperature on dielectric constant is shown in Figure 4.21, where it is evident that ε_r decreased monotonically when the frequency increases [110], but in the high frequency region, the dielectric constant of both samples shows a similar pattern in Figure 4.19 and Figure 4.20. The sample prepared from elemental metal had a higher dielectric constant than the sample prepared from elemental oxides; this can be interpreted in terms of space charge polarisation that arises due to the inhomogeneous dielectric structure of the material. FE-SEM imaging and EDS analysis has shown that samples prepared from elemental metal were more homogenous than samples prepared from elemental oxides. In the low frequency region, the dielectric constants were very high and increased with increasing temperature, whereas in the high frequency region, there was a maximum

in the temperature dependence of ε_r at 480 K (Figure 4.19 and Figure 4.20).

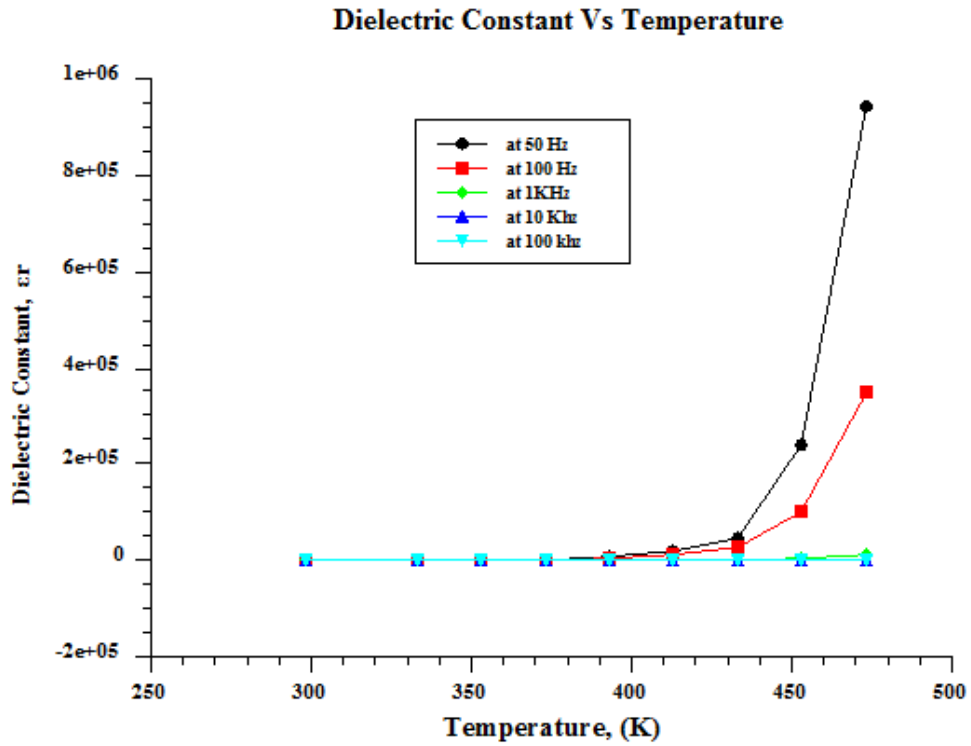

Figure 4.19: Variation of dielectric constant with temperature for elemental metal starting powder samples.

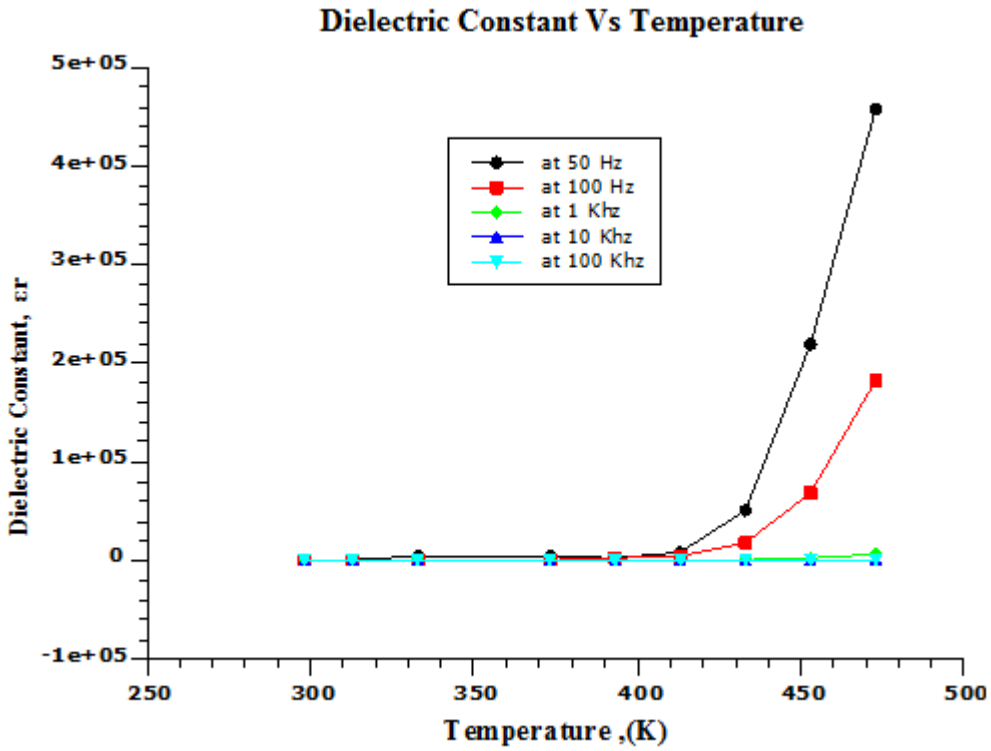

Figure 4.20: Variation of dielectric constant with temperature for elemental oxide starting powder samples.

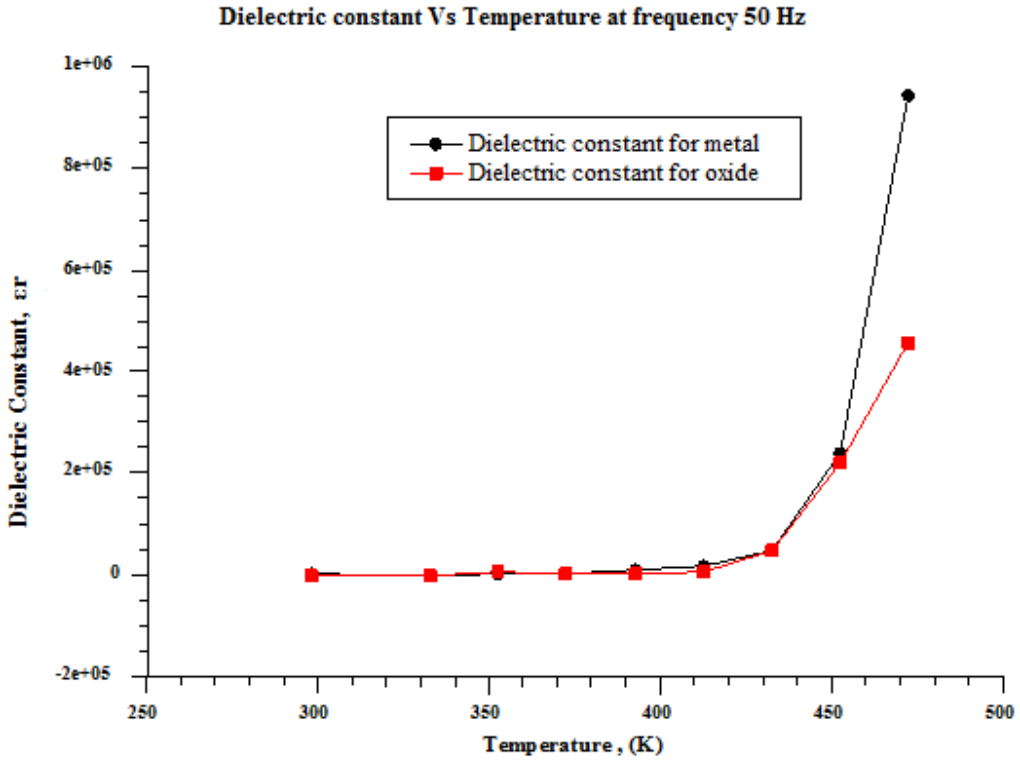

Figure 4.21: Comparison of dielectric constant between metal pellet and oxide pellet at temperature variation.

The dependency of dielectric losses (tanδ) on the frequency, as shown in Figure 4.22, indicated that tanδ decreased as the frequency increased.

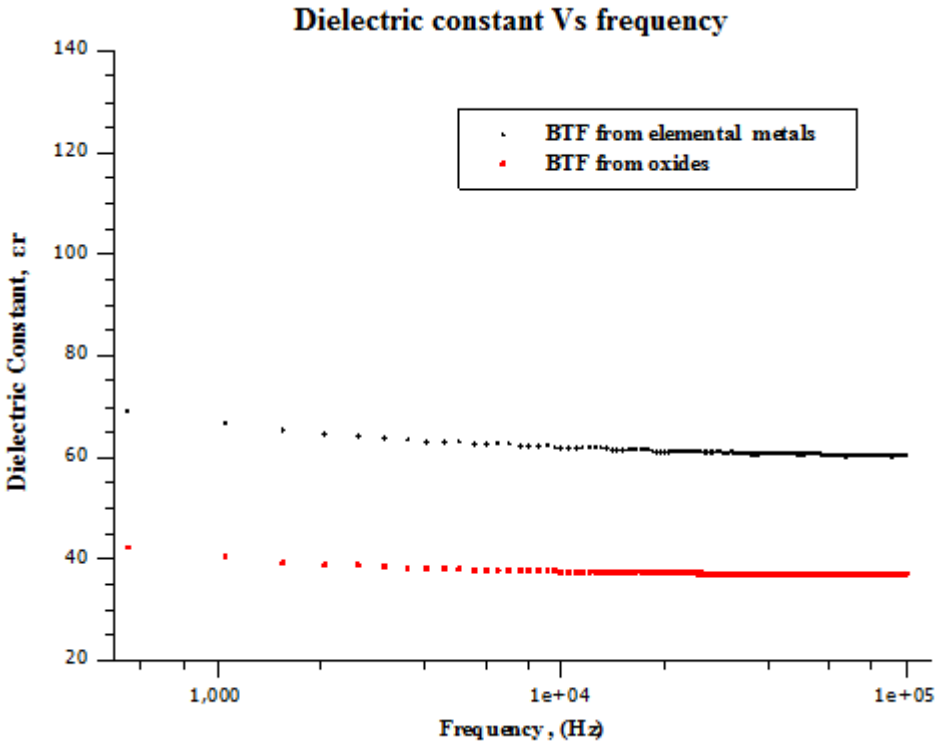

Figure 4.22: Variation of dielectric constant as a function of frequency.

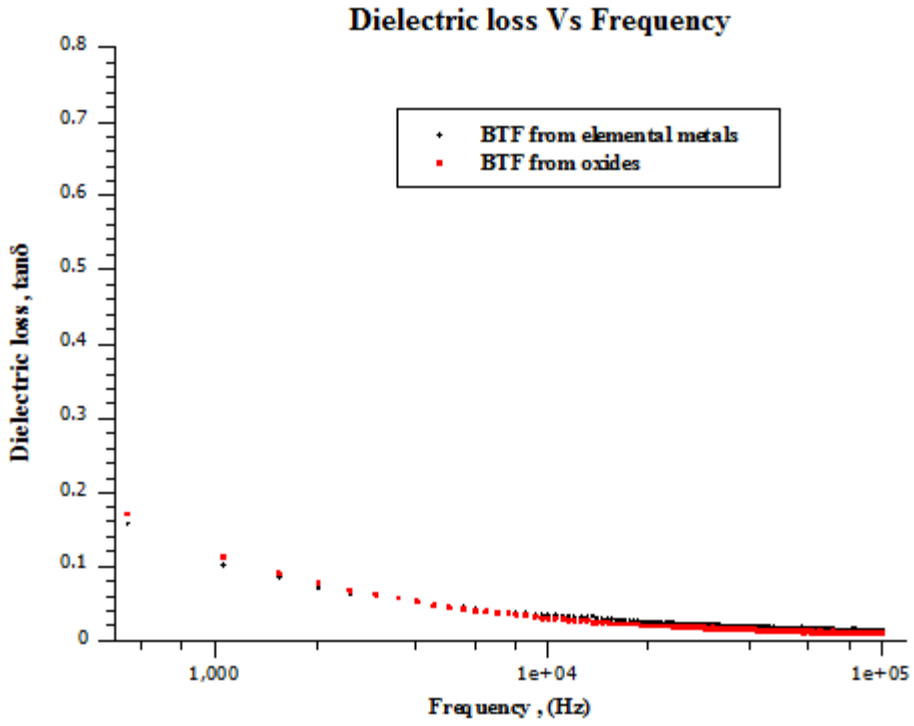

Figure 4.23: Variation of dielectric loss as a function of frequency.

4.2.4.6 Discussion:

A comparison of the dielectric property between the oxide pellets and metal pellets indicated that the BTF of metal pellets had good dielectric properties (Figure 4.20). The large grain dispersion, densely packed with grains, and the location of particular grains in relation to other grains could be where the dielectric constant of BTF prepared from elemental oxides decreased. Moreover, the two-phase nature of the materials was also responsible for the decrease in dielectric constant [111].

4.2.5 .Synthesis of $BaLa_2Ti_4O_{12}$ (BLT) :

To use ceramic materials for practical applications, they should possess low dielectric losses in wide frequency ranges at a given value of permittivity. $BaLa_2Ti_4O_{12}$ is a stable phase in the ternary equilibrium system of $BaO\text{-}TiO_2\text{-}La_2O_3$, as shown in **Figure 4.24** and it has a low dielectric loss over a wide frequency range. A high value of permittivity (ε), low values of dielectric loss (tanδ), and minor changes within a wide temperature range are also features of the dielectric properties of BLT.

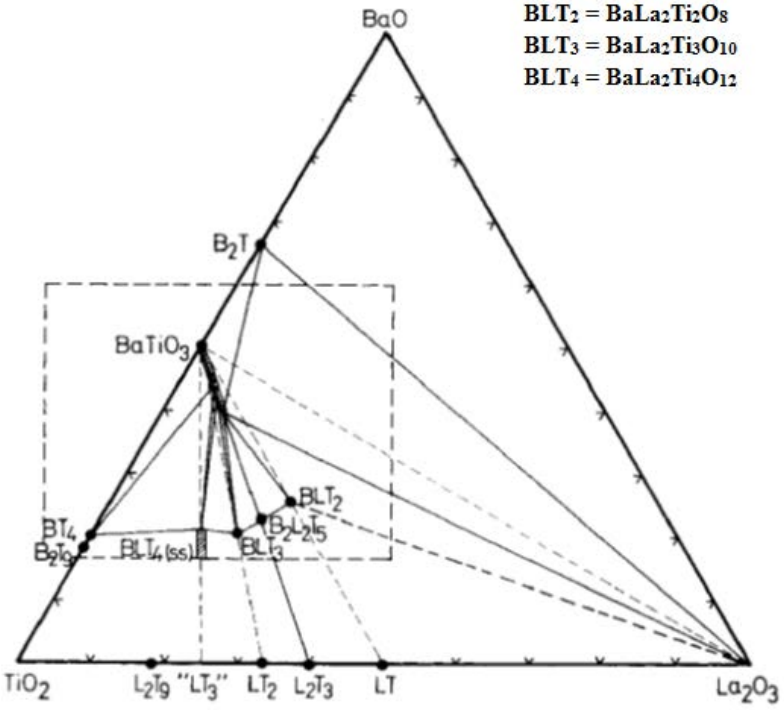

Figure 4.24 : Ternary system of BaO-La_2O_3-TiO_2 at 1300°C

4.2.5.1 XRD analysis:

Figure 4.25 a) shows the X-ray patterns obtained from, premixed BaO (19 wt %) + La_2O_3 (41 wt %) + TiO_2 (40 wt %) and b) the premixed sample after EDAMM processing in argon for 10 mins and, (c) the sample after sintering at 900°C for 24 hours. All the XRD peaks observed after EDAMM can be indexed according to the single-phase perovskite with a $BaLa_2Ti_4O_{12}$ composition (PDF 50-1843). The lack of evidence for additional phases (Figure 4.25 c) indicates that under the previously mentioned sintering conditions, the solid state reactions were substantially completed [112-117] and BLT is the major product phase. The estimated crystal sizes of the BLT after sintering were as follows; using the (110), (111), (200), and (211) peaks respectively; 32.47 nm, 10.66 nm, 15.16 nm and 11.3 nm (average 17.39 nm). As

discussed in Section 4.2.3.3 variations in estimated crystallite size may be associated with the presence of extended defect structures in the sintered sample [103].

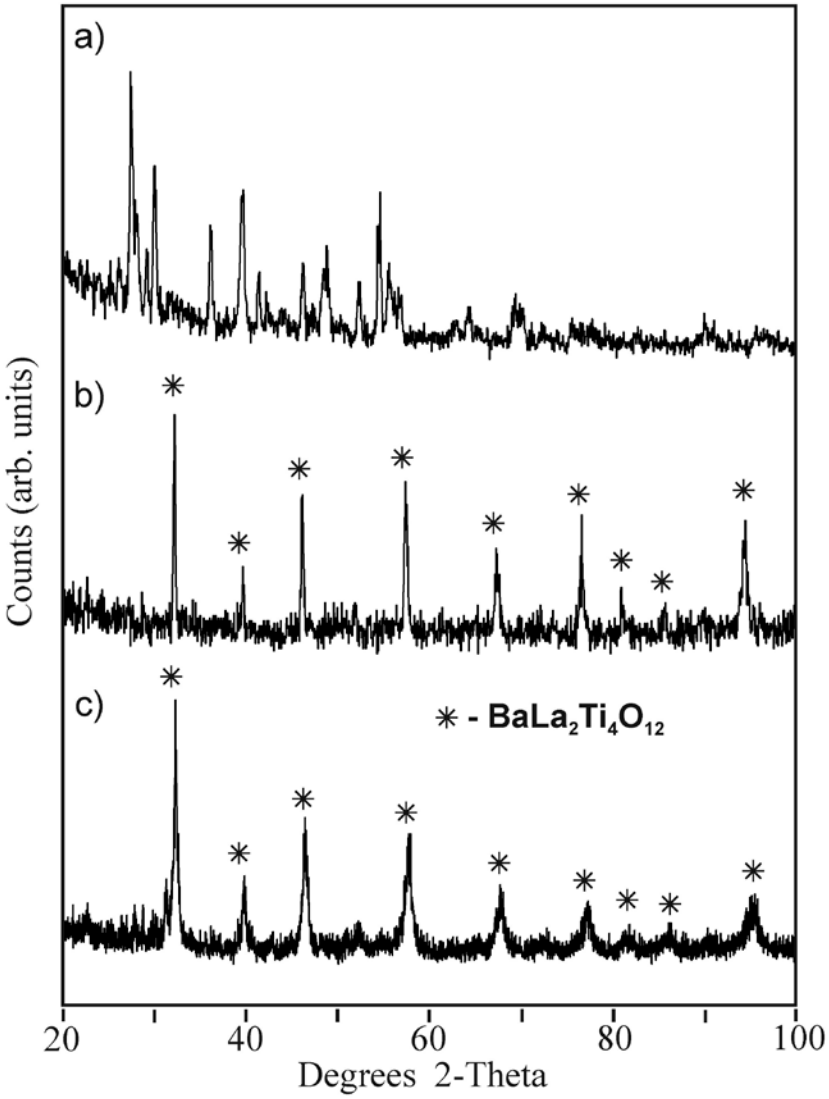

Figure 4.25: XRD patterns obtained from (a) premixed BaO+ La_2O_3+ TiO_3 powders ,(b) produced by EDAMM processing of this sample in argon using AC discharges for 10 minutes and (c) After sintering at 900ºC for 24 hours

4.2.5.2 SEM analysis:

FESEM investigations in backscattered (BSE) mode coupled with EDS mapping and quantitative EDS analyses can help detect small amounts of any secondary phases. SEM investigations revealed a coarse and dense microstructure with large grains. The composition of the sample was analysed by EDS, which revealed that the dark region between the grains was rich in TiO_2 (Figure 4.26).

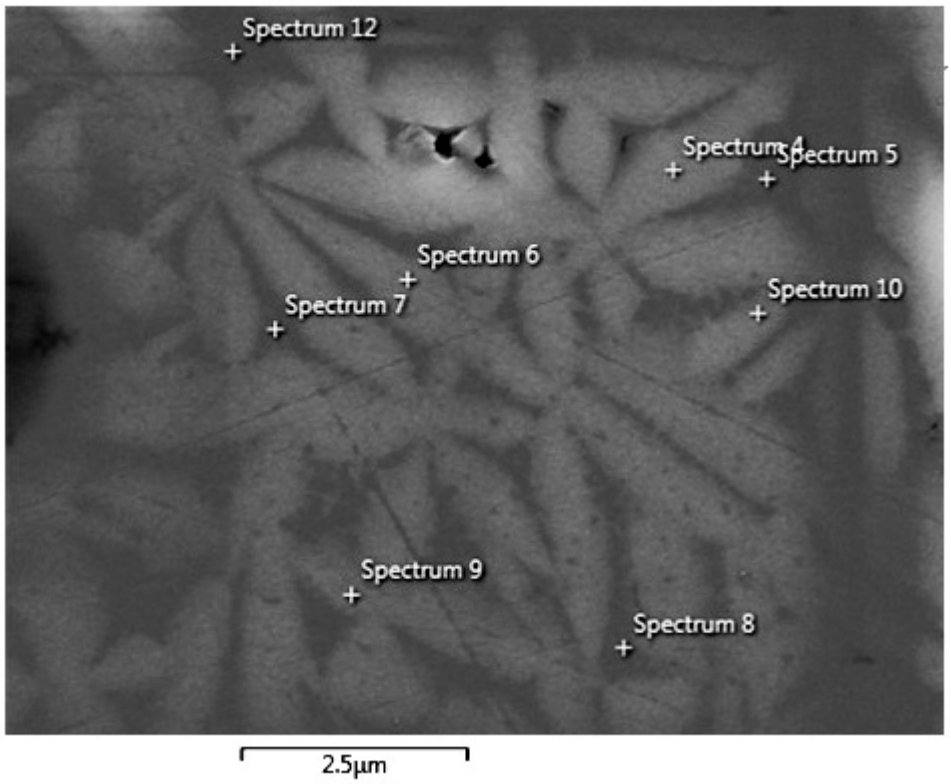

Figure 4.26: EDS spot analysis analysis of BLT pellet prepared from oxides (backscattered electron image).

Table: 4.4 Spot analysis of BLT pellet

	La (wt%)	O_2 (wt%)	Ti (wt%)	Ba (wt%)	Fe (wt%)	Mn (wt%)	Al (wt%)
Spectrum 1	40.3	24.8	19.8	10.6	2.8		
Spectrum 2	41.3	25.2	19.9	10.3	2.9		
Spectrum 3	40.5	24.5	19.8	11.4	2.9		
Spectrum 4	44.5	25.2	19.0	8.9	2.4		
Spectrum 5	29.6	27.5	24.3	13.0	4.3	0.6	0.5
Spectrum 6	42.3	25.3	19.0	10.2	2.6		
Spectrum 7	28.8	26.7	23.9	14.9	4.3	0.6	0.6
Spectrum 8	36.9	25.0	21.6	12.4	2.8	0.8	0.5
Spectrum 9	42.9	24.6	19.7	9.4	2.5	0.6	0.3
Spectrum 10	41.8	25.7	19.7	9.7	2.7		0.4
Spectrum 11	40.0	25.8	20.5	10.8	2.6		0.3
Spectrum 12	30.9	28.3	23.6	11.6	4.3	0.9	0.6

4.2.5.3 Dielectric properties:

The frequency dependent dielectric constant and relaxation nature of dielectric losses in the $BaLa_2Ti_4O_{12}$ compound at room temperature are shown in Figures 4.27 and 4.28 respectively. The dielectric constant and dielectric losses had a constant value over frequency ranges from 50 hz to 100 Khz which was a typical trend observed by other investigators. The value was 23.5 at 50Hz.

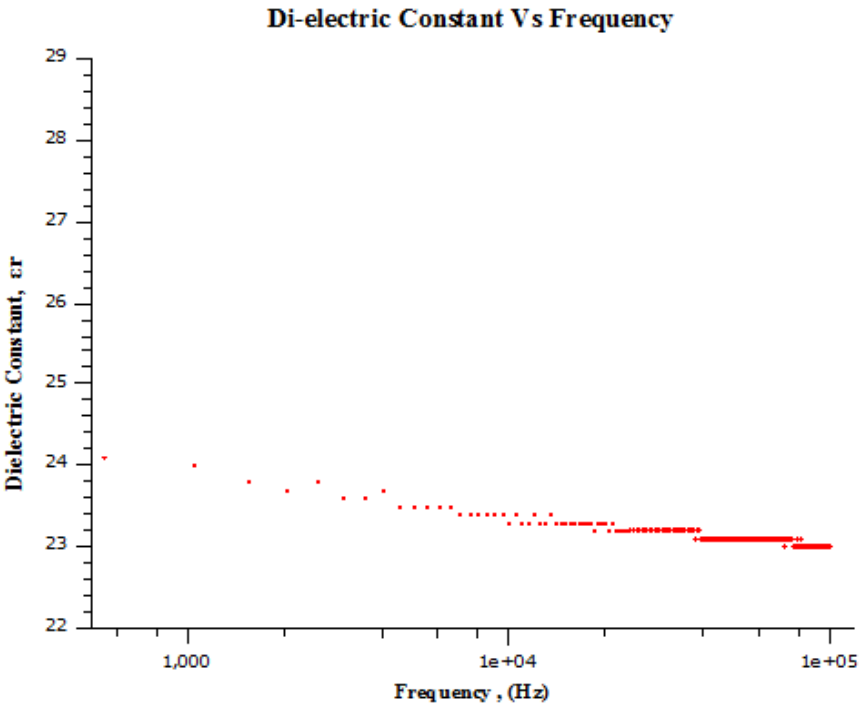

Figure 4.27: Variation of dielectric constant as a function of frequency

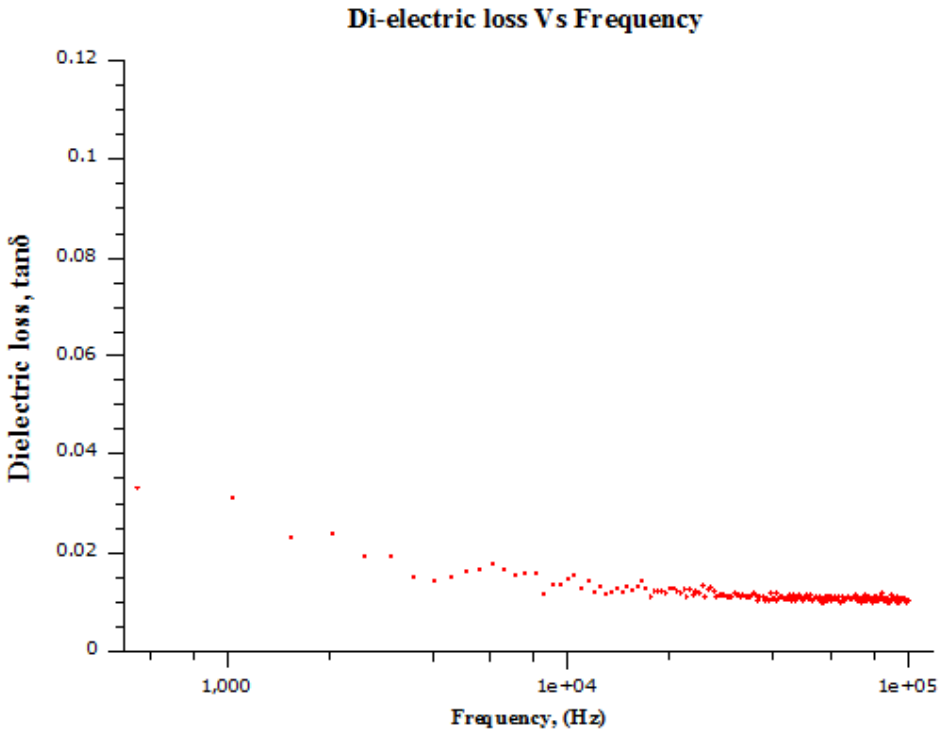

Figure 4.28: Variation of dielectric loss as a function of frequency

4.2.5.4 Discussion:

The BLT structure was like a single-phase perovskite, with a tendency to transition from tetragonal to cubic with an increase in the addition of La of this phase [118]. In this investigation, the dielectric properties were studied as a function of frequency.

The BLT ceramics under investigation were insulators with homogenous defects, which will be discussed as follows: BaO. La_2O_3 and $4TiO_2$ compound with 1:2:2 stoichiometric ratios were synthesised by EDAMM. It is well-known that low donor-doped $BaTiO_3$ ceramics are semi-conducting but at higher doping levels the donor charge compensation mechanism changes and doped $BaTiO_3$ ceramics sintered in air become insulating, and the material becomes a strong dielectric [41, 119] . The charge balance compensation mechanism when Ba^{2+} is replaced by La^{3+} is:

$$Ba^{2+} = La^{3+} + e^{-} \qquad (4.1)$$

At higher contents of La , the replacement of Ba^{2+} by La^{3+} occurs and is associated with the creation of titanium vacancies.

$$Ba^{2+} + \frac{1}{4}\,Ti^{4+} = La^{3+} + \frac{1}{4}\,\square\,Ti \qquad (4.2)$$

At higher doping levels, the donor charge compensation mechanism changes and doped $BaTiO_3$ ceramics sintered in air become insulating.

An excessive amount of TiO_2 as evidenced by the EDS results in Figure 4.25 was believed to be responsible for a reactive liquid phase that formed during sintering. During sintering, liquid $Ba_6Ti_{17}O_{40}$ was formed [120], $BaTiO_3$ grains dissolved in this liquid phase, which enhances the mass transport of La^{3+}. There is rapid grain growth with low La- doping levels, whereas, the La^{3+} - donor ions inhibit grain

growth, which is related to the oxygen partial pressure of the sintering atmosphere. According to the thermodynamic model, it can be expressed by the following format (eqn 4.3) [120]

$$lgp(O2) = \frac{A}{xc} + B \qquad (4.3)$$

Where p (O_2) is the oxygen partial pressure, A is the stored surface energy at the phase boundary, x_c is the critical donor concentration, and B is the free energy of oxygen release during anomalous grain growth. Donor concentration is related to the oxygen partial pressure while A and B are constant.

Since the EDAMM experiment was carried out in a reducing atmosphere and the concentration of La was high, the grain size of BLT was expected to be relatively small for the reasons given above. The concentration of oxygen vacancies is related by following the formula:

$$[V_o^{gg}] = \left[La_{Ba}^{g}\right]^{-n} \qquad (4.4)$$

The concentration of oxygen vacancies decreased with the increase of La concentration. Oxygen deficiency can occur at a high temperature (>900°C, in air) or reducing atmospheres, [121, 122] according to:

$$2O_o^x = O_2(\mathrm{g}) + 2V_o^{-} + 4\mathrm{e}' \qquad (4.5)$$

The concentration of La was higher in this experiment which reduced the oxygen vacancies, which, in turn changed the property from semi-conducting to insulating. The TiO_2 rich region shown in Figure 4.25 was very important because it shows a combination of properties such as high dielectric constant and low losses [123-126] .

The insulating grain boundary regions could be the reason for these dielectric properties [120]. Oxygen loss during sintering in air was very common in these materials which include oxygen-deficient semi-conducting grain interiors and

oxidised insulating grain boundary regions. Lanthanum also helps in the loss of oxygen at high temperatures [120] .

4.3 Synthesis by Magneto-Ball Milling

4.3.1 Synthesis of $MgAl_2O_4$

The aim of this chapter is to investigate the formation of spinel $MgAl_2O_4$ from precursor powders made by magneto-ball milling samples formed from two different starting mixtures: (i) MgO and Al_2O_3 and (ii) MgO and Al elemental powder. After magneto-milling, the samples were processed by reactive sintering. Both of these starting powders were followed by impact and shear ball milling. Unlike impact and shear ball milling, there were no significant variations in the XRD and SEM analysis, but in the study of dielectric property, there were some variations in the impact and shear ball milling sample. The process parameters used for magneto-ball milling are given in Table 4.5:

Table 4.5: Process conditions for Magneto-ball milling

Sample name	Compositions (Wt%)	Milling Time (hrs)	Milling Speed (rpm)	Ball-powder ratio	Atmosphere	Pressure (Mpa)
MgO+Al	MgO = 42.762% ; Al= 22.421%	120	100	1: 20	Oxygen	110
MgO + Al2O3	MgO = 28.33 % ; Al2O3 = 71.67 %	120	100	1: 20	Oxygen	110

Based on the XRD results, the milling mechanism in impact/shearing did not significantly affect the reaction mechanism to form $MgAl_2O_4$. To investigate the results of dielectric properties, various results were found and are discussed in the following sections.

4.3.1.1 XRD studies:

Fig 4.29a) shows the XRD results obtained from the premixed starting powders of MgO and Al. Fig 4.29b) shows the XRD results after 120 hours of milling and show

how peak broadening indicates a reduced grain size compared to the starting powder. After this sample was sintered for 24 hours in air the x-ray diffraction pattern (Figure 4.29c) shows the presence of well-developed XRD peaks that can be indexed to the $MgAl_2O_4$ spinel phase (PDF 01-1154).

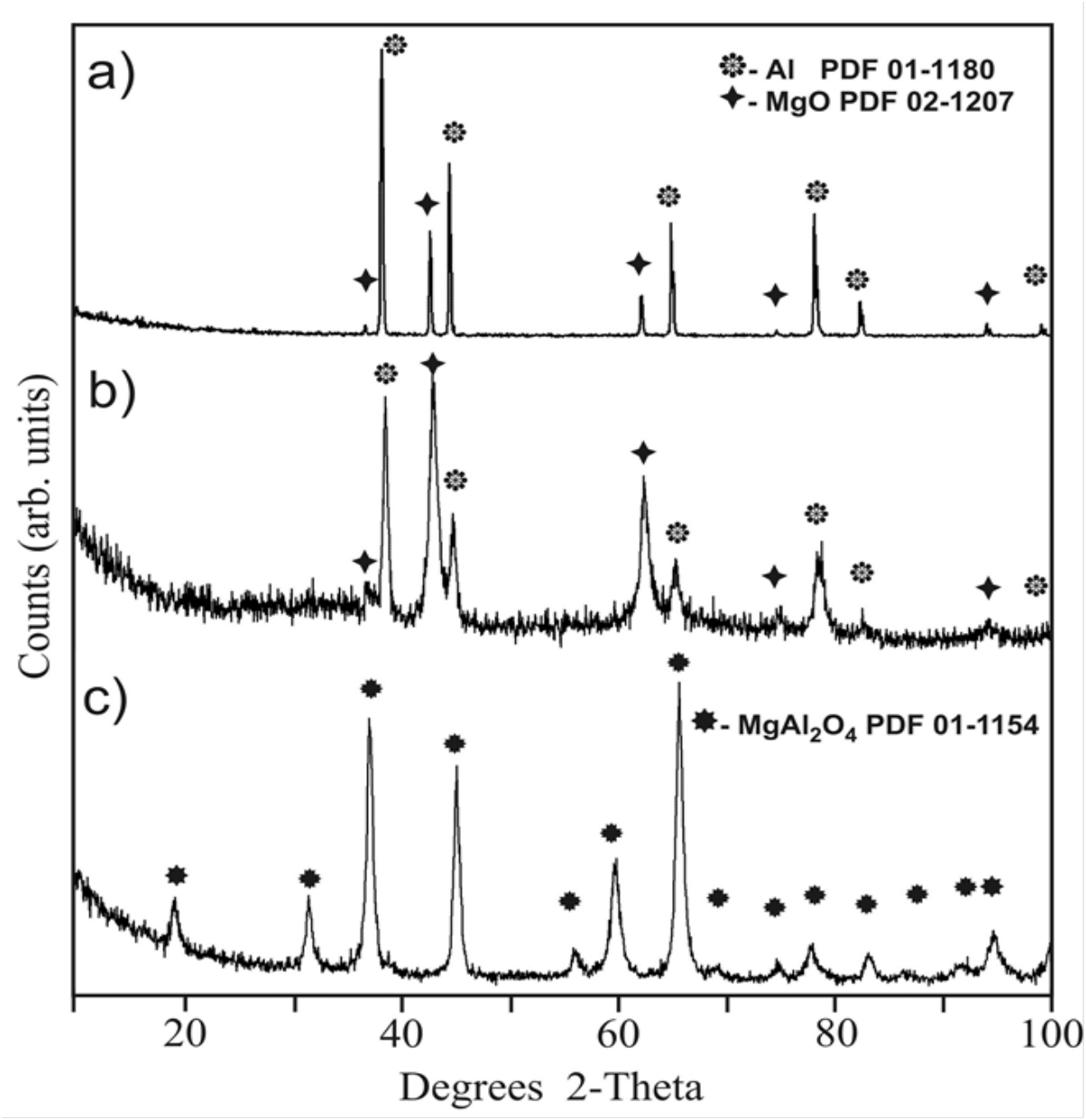

Figure 4.29: XRD results from a) MgO+Al starting powders, b) after 120 hours ball milling and c) sintered the ball milled sample at 900ºC for 24 hours.

Figure 4.30a) shows the XRD results obtained from premixed and sintered starting powders of MgO and Al_2O_3. No reaction occurred after these starting powders were sintered directly (Figure 4.30b)), but after 120 hours of ball milling the grain sizes of the starting powder decreased, as shown by the significant peak broadening (Figure 4.30). After sintering, the ball milled powders for 24 hours in air the spinel produced with XRD peaks were indexed according to the phase $MgAl_2O_4$ (PDF 01-1154), as shown in Figure 4.30d). Additional phases associated with the starting powders (MgO and Al_2O_3) were also observed and indicated the transformation to 100% $MgAl_2O_4$ spinels was incomplete.

.

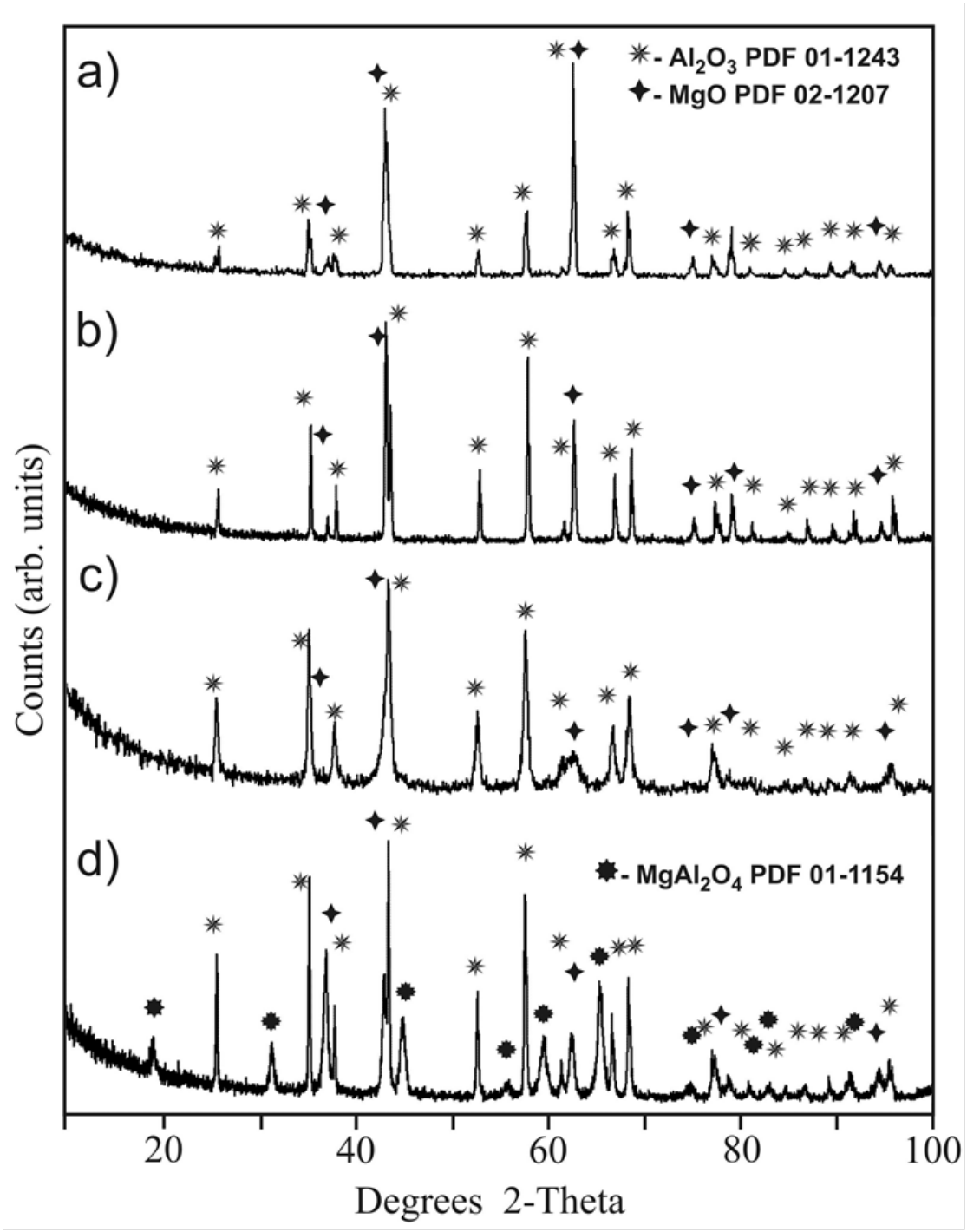

Figure 4.30 XRD results obtained from a) starting powder of $MgO+Al_2O_3$,b) Directly sintered starting powder, c) powder after 120 hours ball milled and d) ball milled powder after sintering at 900ºC for 24 hours.

The estimated crystal sizes of the $MgAl_2O_4$ spinel structure prepared from MgO+Al starting powders were as follows; using the (111), (2 2 0), (5 1 1), (4 4 0) peaks

respectively ; 28.68 nm, 11.74 nm, 15.63 nm and 27.815 nm (average 20.96). The estimated crystal sizes of $MgAl_2O_4$ spinel prepared from MgO and Al_2O_3 were found using the (111), (2 2 0), (5 1 1), (4 4 0) peaks respectively; as 53.15 nm, 12.41 nm, 12.57 nm and 20.71 nm (average, 24.71 nm). This indicates that the spinel structure $MgAl_2O_4$ produced from MgO+Al soft materials had a slightly more refined nano-structure than that formed by milling the $MgO+Al_2O_3$ hard materials.

4.3.1.2 SEM analysis:

The backscattered images of Figure 4.31 and Figure 4.32 shows the micrograph of $MgAl_2O_4$ spinel structure of ball milled samples of MgO + Al and MgO + Al_2O_3 respectively. The milled and sintered MgO + Al sample has a denser structure than the $MgO+Al_2O_3$. Fe contamination has been analysed by EDS. Table 4.6 and Table 4.7 summarises semi-quantitative estimates of elemental compositions obtained from large areas of both samples. The Fe contamination in the sample produced from $MgO+Al_2O_3$ is higher in both weight and atomic ratio than the sample produced from MgO+Al.

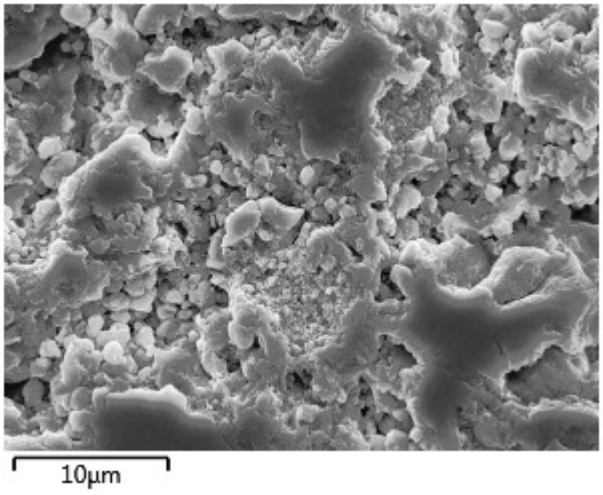

Figure 4.30: SEM analysis of $MgAl_2O_4$ from MgO+Al.

Table 4.6: EDS analysis of $MgAl_2O_4$ from MgO+Al.

Elements	Wt%	At%
O	44.22	56.42
Mg	17.98	15.09
Al	37.55	28.40
Fe	0.13	0.05

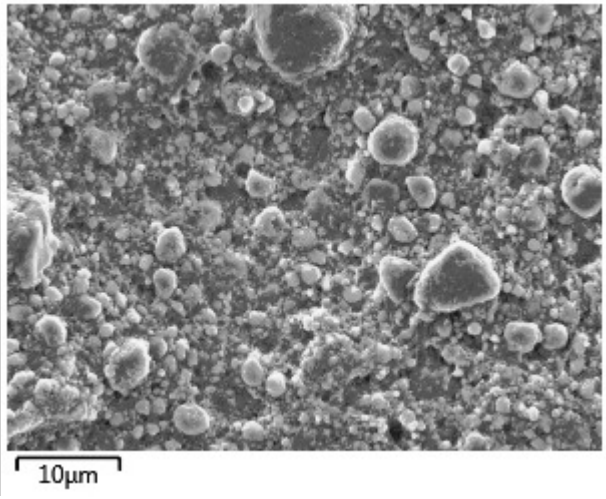

Figure 4.31: SEM analysis of $MgAl_2O_4$ from $MgO+Al_2O_3$

Table 4.7: EDS analysis of $MgAl_2O_4$ from $MgO+Al_2O_3$

Elements	Wt%	At%
O	37.15	49.64
Mg	7.37	6.48
Al	55.30	43.81
Fe	0.18	0.07

4.3.1.3 Dielectric properties:

The dielectric properties of spinels depend on several factors, including the method of preparation, chemical composition, and grain size. Because the starting powders of MgO+Al and Al_2O_3 + MgO were in impact mode, the dielectric constant was almost similar, whereas in shear mode, the starting powder of Al_2O_3 + MgO had a higher dielectric constant than the MgO+Al starting powder. This can be explained by the excessive amount of MgO and Al_2O_3 where the dielectric constant of MgO and Al_2O_3 are higher than the $MgAl_2O_4$ spinel [127]. When shear and impact ball

milling are compared, the dielectric constant was higher in shear-milling mode because the samples sintered after shear-milling had less iron contamination from the milling cell and the final powder was more homogenous. The results presented in Figure 4.33 indicate that the dispersion was sharp at lower frequencies and almost levelled off at higher frequencies. This behaviour may be due to the existence of interfacial polarisation [128] because the normal dielectric behaviour of spinel was explained by the Maxwell-Wagner interfacial type of polarisation, which agrees with Koop's theory [129]. According to the Maxwell-Wagner model, the dielectric structure of a spinel material is assumed to derive from two layers; the first being a conducting layer that consists of large aluminate grains, while the other is a grain boundary which is poorly conducting. This bi-layered formation is influenced by high temperature sintering.

The variations of loss tangent (tanδ), with frequency for the differently prepared magnesium aluminate samples is shown in Figure 4.34. The general trend is a sharp decrease in dielectric constant with increase in frequency. The $MgO+Al_2O_3$ starting powder had a higher dielectric loss than MgO+Al as a starting powder, which means that depending on the processing method used, shear ball milling results in a higher dielectric loss.

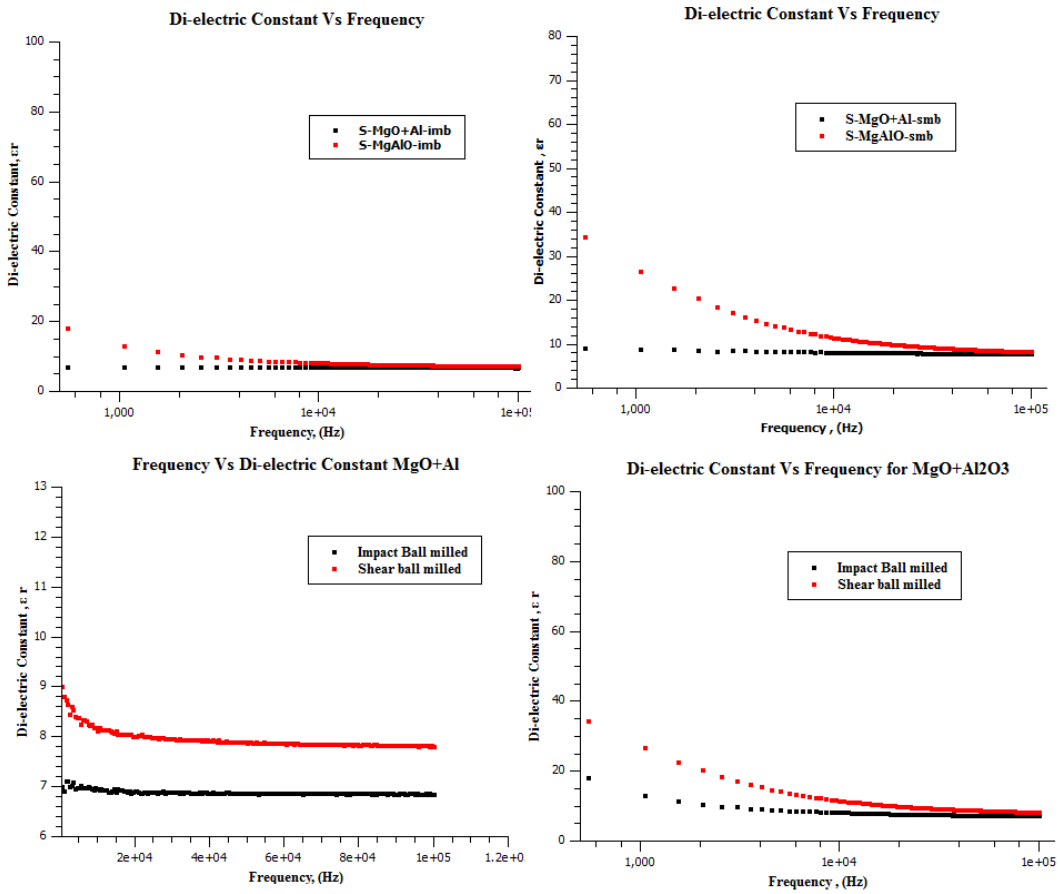

Figure 4.33 a) Dielectric constant Vs frequency in impact mode; b) in shear mode; c) comparison between impact and shear-milling for MgO and Al being as starting powder ; d) comparison between impact and shear-milling for MgO and Al_2O_3 being as starting powder.

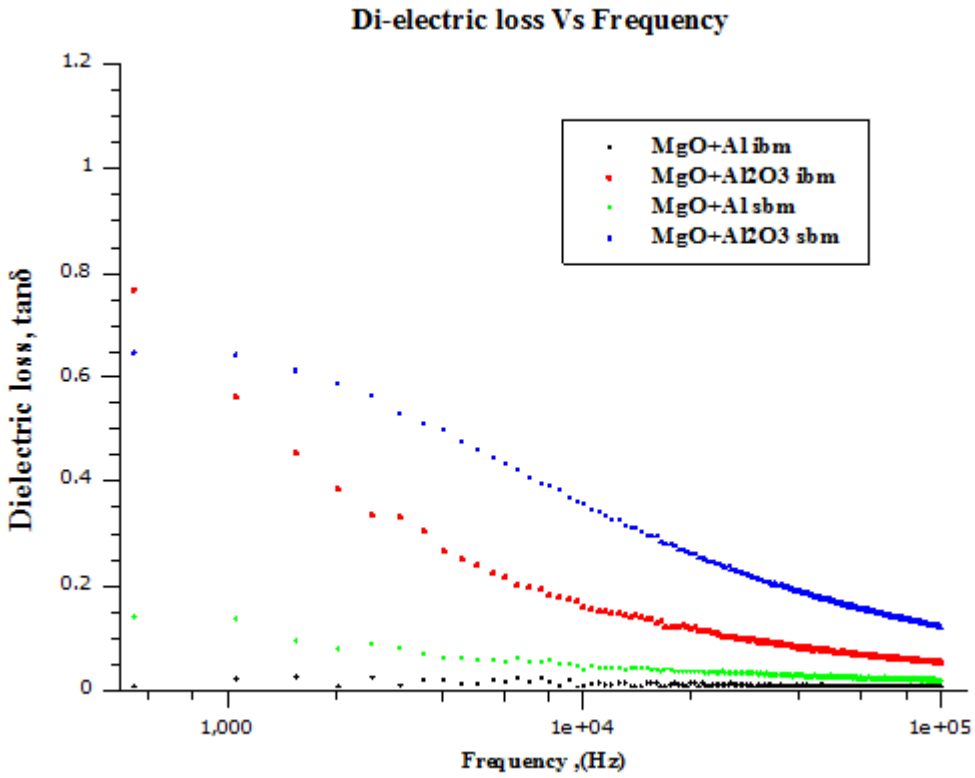

Figure 4.34: Dielectric loss Vs Frequency at impact and shear mode.

4.3.1.4 Discussion:

Schacht [130] proposed that at the interface between particles of MgO and Al_2O_3, small crystals with a spinel stoichiometry and structure are nucleated relatively easily on the surfaces of either MgO or Al_2O_3 grains, but once these initial spinel layers form, the subsequent growth or thickening of the spinel product becomes much more difficult because the two reactants, MgO and Al_2O_3, are then separated by a rather impenetrable spinel layer. To continue the reaction, a complex counter-diffusion process is required where Mg^{2+} ions diffuse away from and Al^{3+} ions diffuse towards the MgO-$MgAl_2O_4$ interface and vice versa for the $MgAl_2O_4$- Al_2O_3 interface.

In this situation, spinel formation is particularly slow because ions such as Mg^{2+} and Al^{3+} diffuse slowly. Moreover, defects are required, particularly vacant sites into

which adjacent ions can hop. This can be promoted by dynamically maintaining high reaction interface areas and a short circuit diffusion path provided by the large number of defects such as dislocations and grain boundaries induced during ball milling.

The incomplete nature of this reaction can be attributed to the relatively high hardness of the starting powders of MgO (knoop hardness 370) and Al_2O_3 (knoop hardness 2100) [131]. The diffusion rate for the reaction of spinel structures is low for high hardness materials.

In balling milling mechanical activation occurs, which increases the interphase of the reacting phase that can enhance the reaction kinetics during subsequent annealing [132]. In this experiment, the spinel phase increased to a great extent while traces of MgO and Al_2O_3 were observed after subsequent annealing. The fast disappearance of MgO diffraction lines was caused by a mechanical activation on the reaction rate as a result of better reactivity of the initial materials. Mechanical activation increases the interface of the reacting phases, which may enhance the reaction kinetics during subsequent annealing. The absence of MgO and Al on the XRD patterns after sintering indicated that during mechanical activation, a homogenous powder mixture was achieved. As Figures 4.29b) and 4.29c) shows the XRD peaks decreased in intensity as the milling time increased, while their width increased after annealing at 900ºC for 24 hours. This occurred because the size of the crystallite after annealing was lower for the sample milled for a longer time. During milling, the density of dislocation increased as a result of more nucleation sites being available during crystallisation upon annealing, which in turn led to a smaller sized final crystallite [132]

4.3.2 Synthesis of $CaCu_3Ti_4O_{12}$ from CaO , CuO_2 and TiO_2

Fine $CaCu_3Ti_4O_{12}$ (CCT) powders were prepared by the Uni-Ball-Mill method using CaO, CuO and TiO_2 as raw materials. Stoichiometric proportions of this powder were mixed according to the formula $CaCu_3Ti_4O_{12}$. The processing conditions used for magneto-ball milling are given in Table 4.8. The powder was cold pressed into 4mm diameter by 1~1.5 mm thick pellets, which were then sintered at 900˚C in air for 24 hours.

Table 4.8: Magneto-ball milling used for preparation of CCT powder precursor

Sample Name	Composition (wt%)	Milling Time (hrs)	Milling Speed (rpm)	Ball to powder ratio	Atmosphere	Pressure Kpa
$CaCu_3Ti_4O_{12}$	CaO = 9.143% CuO = 38.69% TiO_2 = 52.158%	120	100	1: 20	Oxygen	110

4.3.2.1 XRD analysis

To investigate the phase changes during magneto-ball milling synthesis, the milled product was examined by XRD analysis. Figure 4.34 and Figure 4.35 show the XRD results obtained from powder samples milled under impact (Figure 4.34) and shearing (Figure 4.35) for various milling times. The figures also show the results obtained for samples milled for 120 hours and then heat-treated at 900°C in a furnace under atmospheric conditions. The figures show that as milling progressed, the TiO_2, CuO, CaO_2 underwent grain refinement and an accumulation of stress, as evidenced in peak base broadening and height reduction and peaks shifting to lower angles. This reduction in peak intensity in the early stage of milling was drastic, whereas a rapid decrease occurred after 72 hours. The (101), (1 0 3), (2 0 0), (1 0 5), (2 1 3) plane reflection peaks of TiO_2; (1 1 1), (1 1 1), (0 2 0) peaks from CuO and (2 2 0)

from CaO disappear after 120 hours of milling. This prolonged milling resulted in the formation of a nano-structure.

After sintering at 900°C, these nanostructured grains were fully developed, and could be indexed to $CaCu_3Ti_4O_{12}$.

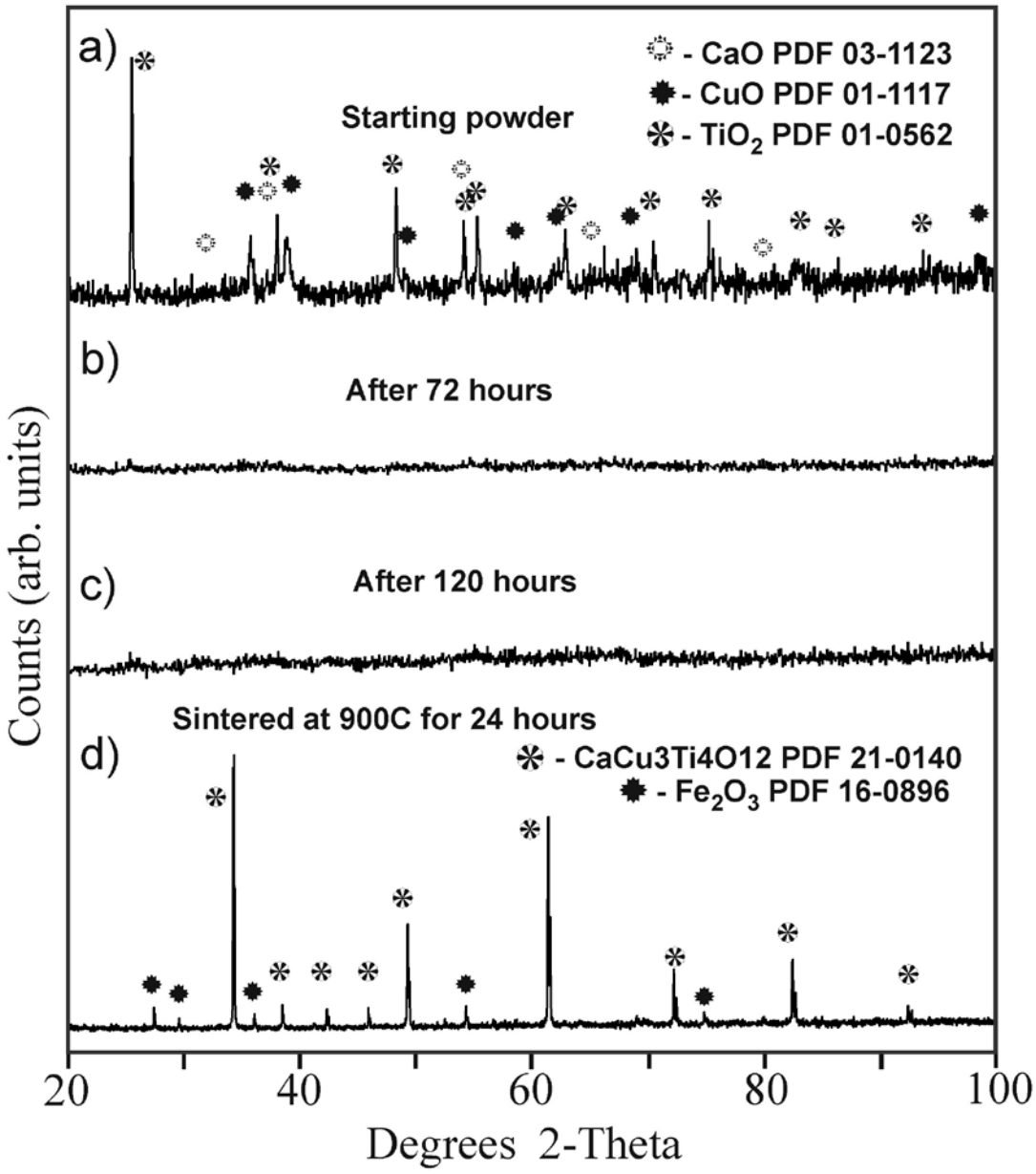

Figure 4.34: XRD results in impact mode from a) CCT starting powders, b) after 72 hours ball milling and c) after 120 hours d) sintered the ball milled sample at 900ºC for 24 hours.

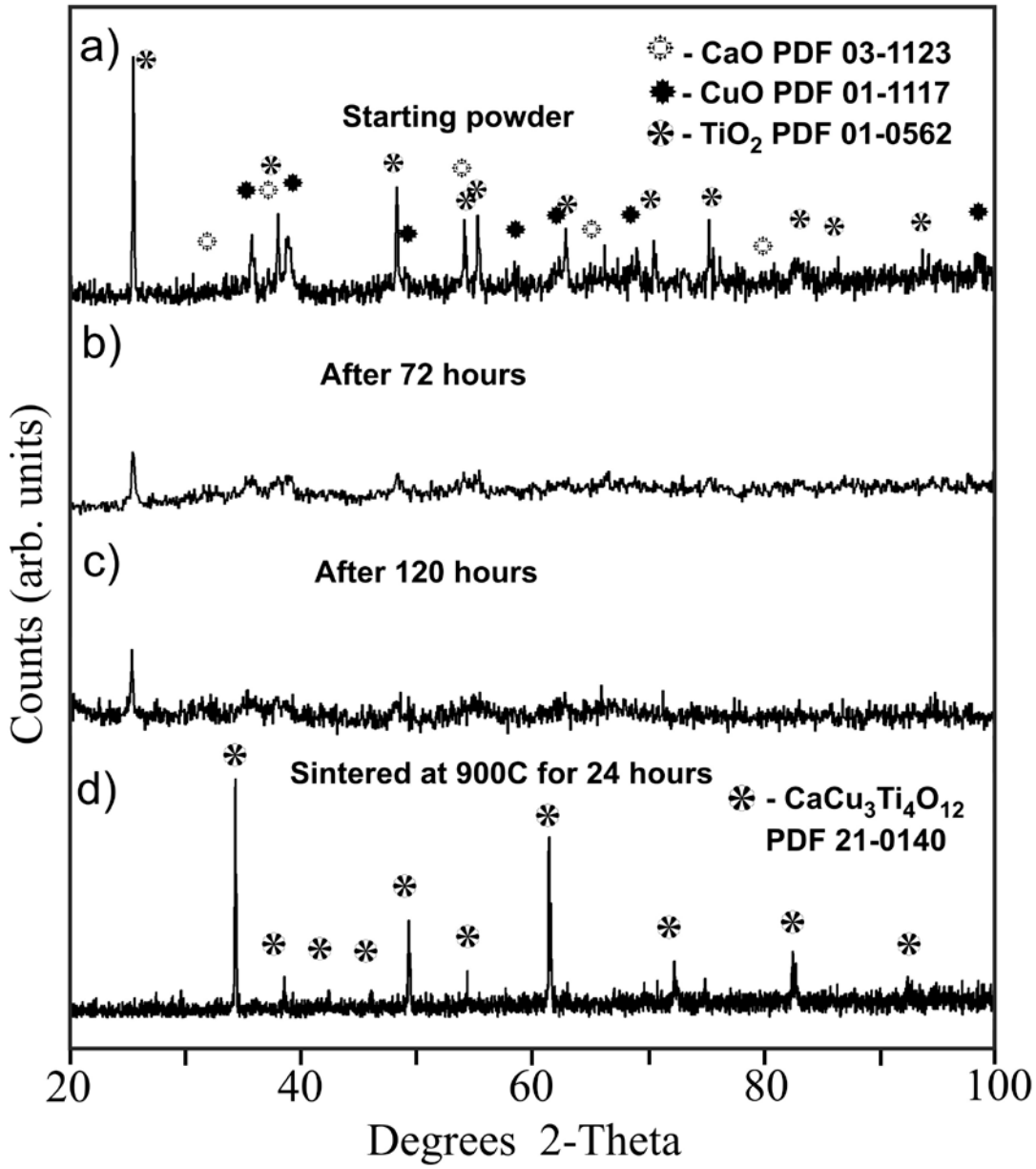

Figure 4.35: XRD results in shear mode from a) CCT starting powders, b) after 72 hours ball milling and c) after 120 hours d) sintered the ball milled sample at 900ºC for 24 hours.

4.3.2.2 Scanning electron microscopy (SEM):

Figures 4.36a) and b) show images (SEM backscattered images) of surface morphologies of small particles in impact and shear mode milling after 120 hours The morphology shown in Figure 4.37b) was more homogenous than Figure 4.37a)

impact milling [APPENDIX C]. The EDS analysis indicates that the dark spots in the CCT compound shown in Figure 4.37a) was a Ti rich region [APPENDICES A and B], where the morphologies of the impact sample are finer than the shear sample. This can be explained by the higher energy associated with impact ball milling. These fine particles assist faster and more reactive sintering that causes excessive shrinkage and grain growth. That is why CCT after sintering prepared by impact ball milling possessed the larger grains shown in Figure 4.37.

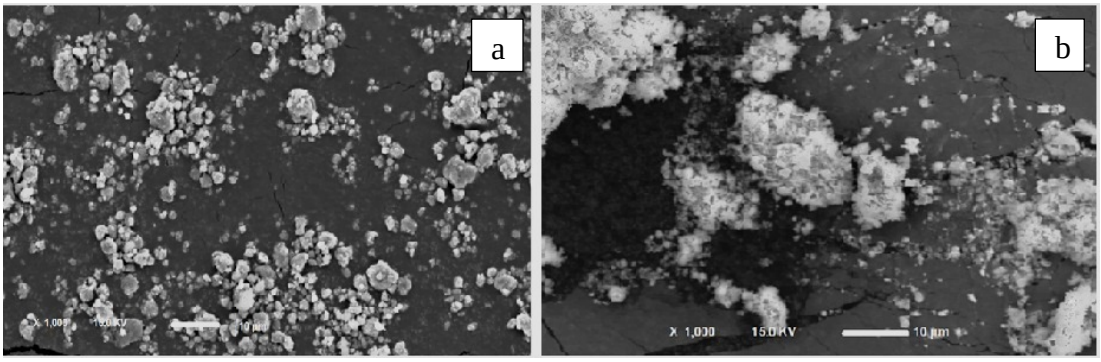

Figure 4.36: a) SEM of CCT after 120 hours milling in impact mode. b) CCT after 120 hours milling at shear mode.

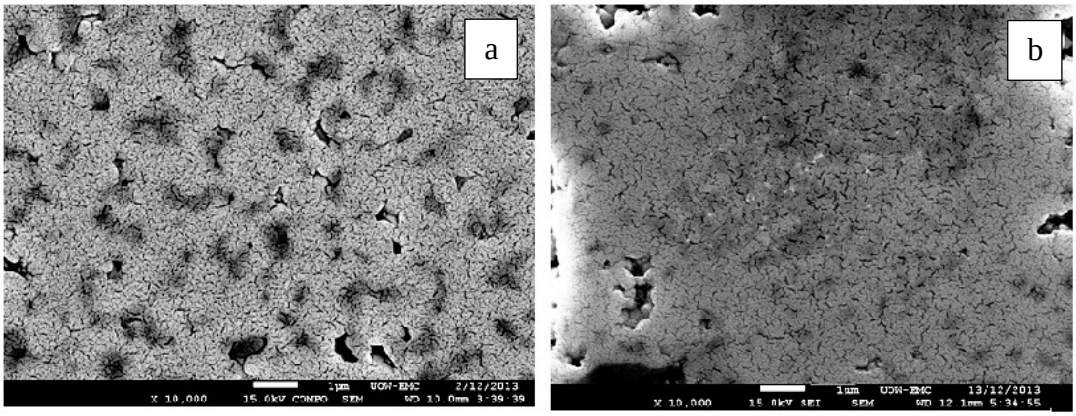

Figure 4.37 a) CCT sintered at 900° C after 120 hours in impact mode b) CCT sintered at 900° C for 24 hours after 120 hours in shear mode

4.3.2.3 Dielectric properties:

The dielectric constant (ε_r) and loss ($\tan\delta$) of $CaCu_3Ti_4O_{12}$ pellets, after being sintered at 900ºC for 24 hours and then milled for 120 hours in impact and shearing are shown in Figure 4.38. The dielectric constants and dielectric loss for all the samples decreased as the frequency increased in a range from 50 Hz to 100 Khz. Dielectric constant of shear ball milled for 120 hours showed better results than those impact-milled for 120 hours. After sintering the dielectric constant of impact-milled had higher dielectric constant than sheared milled followed by sintering.

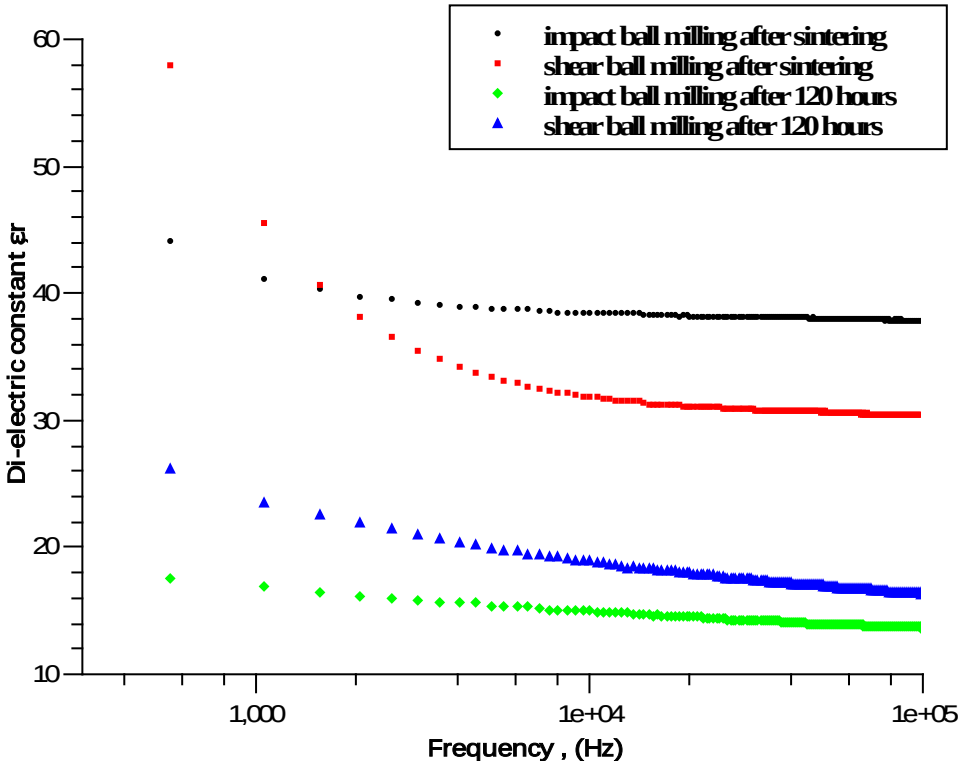

Figure 4.38: a) Variation of dielectric Constant Vs Frequency

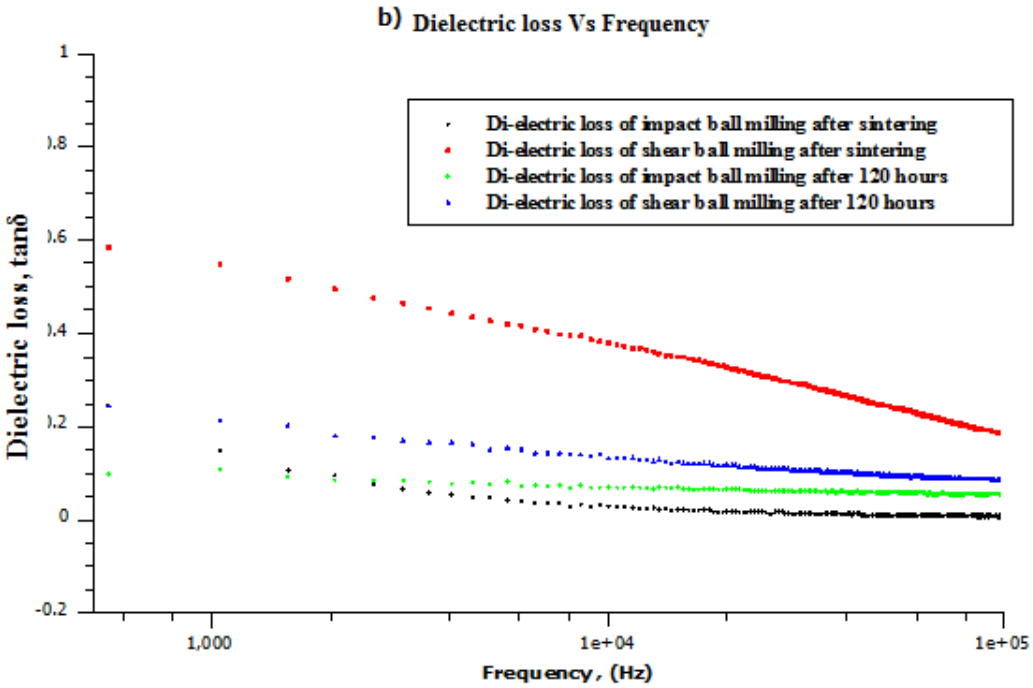

Figure 4.38: b) variation of Dielectric Loss Vs Frequency

4.3.2.4 Discussion

It is more or less commonly accepted that the dielectric properties of CCT are caused by an extrinsic mechanism, such as from an IBLC, which means semi-conducting grains with insulating grain boundaries [133-136]. During ball milling, MA occurred at room temperature, because the reactants were severely strained [74, 137]. It is generally assumed that this strain was due to the introduction of line and point defects and a reduction in the grain size because the diffusion pathway changes during milling from bulk diffusion to short circuit and the activation energy is decreased as a consequence [74]. It is apparent that the kinetic energy of the balls is transferred to the powders, which increases lattice energy and decreases the

activation energy. Moreover, shearing milling and impact milling have a similar effect, although the impact milling generates a rapid decrease in grain size at earlier stages of milling.

When calcium oxide, copper oxide and titanium oxide are milled in an oxygen atmosphere the following reaction takes place $CaO + 3CuO + 4TiO_2 = CaCu_3Ti_4O_{12}$. However, when milling is conducted in a closed chamber filled with oxygen under high pressure (e.g. 110 KPa), the reaction between the powders can be determined by monitoring the changes in pressure. This provides a simple way to monitor the progress of the reaction during milling and allows for a direct comparison between different milling conditions. However, our experimental results revealed that noticeable nano-structure formations occurred because ball milling of CaO, CuO and TiO_2 mixture leads to the formation of a nano-structure, which then transformed into CCT on sintering.

The dielectric constant of pellets sheared and milled for 120 hours shows a higher dielectric constant than pellets that were impact-milled. The contributing factors are believed to include; (i) a grain size effect and (ii) the effects associated with an increasing iron (Fe) contamination in the sample milled under impact. The average grain size of sheared milled pellet was larger than pellets impact ball milled and there was less iron contamination from the milling cell because the shear-milling mode is much gentler. Iron, as a conductive metal was believed to be responsible for a reduction in the dielectric constant. During sintering, Fe was dissolved into the grains making it less susceptible to being conductive which increased the dielectric constant. Before sintering, the powders milled for 120 hours under impact ball milling had a smaller grain size, which would mean that they were more reactive

during sintering. A comparison between the impact and shear ball milled sintered samples shows that the impact-milled pellets had better results than the shear-milling pellets due to a larger grain size. Samples with large grains are believed to contain many domains compared to the samples with normal or fine grains. A large amount of tiny domains inside the large size grains typically results in high dielectric constant, because of the IBLC effects [138-140].

CHAPTER 5: SUMMARY AND CONCLUSIONS

In this thesis the microstructure and dielectric properties of complex ceramics produced by novel EDAMM processing and subsequent sintering in air have been investigated. High permittivity complex ceramics can be used for dielectrics in a solid state supercapacitor of which $MgAl_2O_4$, $CaCu_3Ti_4O_{12}$, $BaLa_2Ti_4O_{12}$, $Bi_5Ti_3FeO_{15}$ are highly promising materials for this application due to their stable and insulating charecteristics.

Different types' solid state synthesis routes, e.g., mixed solid state, Sol-gel etc., can also be used for synthesising these complex materials, but in this study, we used EDAMM and magneto-ball milling to synthesise these ceramics. By using EDAMM, single-phase multi-element oxides can be formed in as little as 0.1% of the processing time required in conventional solid state synthesis techniques.

The four complex ceramic phases, ($MgAl_2O_4$, $CaCu_3Ti_4O_{12}$, $BaLa_2Ti_4O_{12}$, $Bi_5Ti_3FeO_{15)}$ were successfully synthesised using both the EDAMM and conventional mechanical milling methods followed by sintering in air. XRD analysis of as-milled products showed the presence of nano-structures in all EDAMM processed samples which were converted into coarser grained structures after pressing and sintering in air. The morphologies and compositions of the ceramic structures were investigated by SEM-EDS and TEM. As expected for complex oxide dielectrics, with increasing measurement temperature, dielectric constants increased due to the increased ease of movement of charge carriers in the semi-conducting region within the crystals. A summary of results is given in Table.5.1.

Table 5.1: Summary of results

Complex oxides	Processing method	Dielectric constant, εr at 50 Hz	Grain size, (nm)
$MgAl_2O_4$	EDAMM	14	10-30
$CaCu_3Ti_4O_{12}$	EDAMM	48,000	27.21-54.77
$Bi_5Ti_3FeO_{15}$	EDAMM	70	76.72- 149.42
$BaLa_2Ti_4O_{12}$	EDAMM	22-29	17.39
$MgAl_2O_4$	Magneto-Ball Mill	30-40	9.8-16.91
$CaCu_3Ti_4O_{12}$	Magneto-Ball Mill	50-60	57.1-125.2

The exceptionally high value of dielectric constant of $CaCu_3Ti_4O_{12}$ processed via EDAMM (ε_r=48,000) was attributed to a combination of the processing conditions, and the large grain size which according to the IBLC effect is believed to contain tiny domains. Larger grains have a larger density current path which is believed to affect the magnitude of the high dielectric constant. The samples with large grains contain many domains compared to the samples with normal or fine grains. A large amount of tiny domains inside the large size grains contribute to the high dielectric constant because of the IBLC effects. The dielectric constant of CCT was found to be in agreement with the Debye-like relaxation model, where the dielectric response in such a material is associated with mobile charge carriers inside the grain.

Single-phase $Bi_5Ti_3FeO_{15}$ (BTF) was also synthesised by EDAMM in nano-crystalline form. A more homogenous structure of BTF was found in BTF processed from elemental metals than from BTF processed from oxides and this variation is responsible for dielectric constant variation between the two samples. The sample prepared from elemental metals had a higher dielectric constant than the sample prepared from elemental oxides; this can be interpreted in terms of space charge polarisation that arises due to the inhomogeneous dielectric structure of the material.

BLT nanopowder was produced by EDAMM, and after sintering, recrystallised into microcrystalline BLT. A dielectric constant in the range 22-29 was measured. Concentration of Lanthanum affects the grain growth because, the La concentration increases, the grain size of BLT grains become smaller as La^{3+} ions inhibit grain growth.

The second aim of this study was to compare EDAMM with magneto-ball milling with selected complex oxide compounds, i.e., $MgAl_2O_4$ and $CaCu_3Ti_4O_{12}$. The milling was conducted under both impact and shear-milling modes. In both cases, impact ball milling produced more Fe contamination and smaller particles than shear ball milling, but after sintering, the samples processed via impact ball milling had a larger grain size which was believed to be responsible for the high dielectric constant. Materials processed via magneto-ball milling generally have higher contamination than those processed by EDAMM, except for the case of samples EDAMM processed in oxygen. Furthermore, a more nano-crystalline powder can be obtained using EDAMM rather than magneto-ball milling and within a much shorter time.

This study showed that the EDAMM processing is an innovative and highly effective method preparing of nano-sized powders with high purity, which gives us the ability to rapidly obtain chemically homogenous powder of single-phase complex oxide dielectrics.

CHAPTER 6: OUTLOOK

Based on this preliminary investigation of EDAMM synthesis of four different complex oxide dielectrics it can be concluded that EDAMM appears a suitable approach to the current and new phases for application in solid state supercapacitors.

The economic feasibility of EDAMM needs to be further researched. This will ultimately be determined by total energy consumption during the EDAMM synthesis, additional energy consumption for conversion of EDAMM processed nano-structural precursors into recrystallised product. The EDAMM power consumption is a key factor which would decide whether it can be applied to mass production or not. For measurement and calculation of the specific energy used to induce a selected reaction during EDAMM processing, energy inputs are those required for vibration of the mill base and plunger, and energy associated with application of the electrical discharge. Comparison of the specific energy to the thermodynamic requirements for the selected reaction need to be investigated.

REFERENCES

1. *Meeting the Energy Needs of Future Warriors*. 2004: The National Academies Press.
2. Love, G.R., J. American Ceram. Soc, 1990. **73**.
3. W. J. Sarjenat, J.Z.a.F.W.M., IEEE Trans. Plasma Sci, 1998. **26**(5): p. 1368-1398.
4. Christen, T. and M.W. Carlen, J. Power Sources, 2000. **91**(2): p. 210-216.
5. R.S. Khurmi, R.S.S., *Mater. Sci.* 2013: S.Chand & Company Ltd.
6. Frackowiak, E.a.F.B., Carbon, 2001. **39**: p. 937.
7. Wang, J., S.Q.Zhang,et al.,, J. Electrochem. Soc, 2001. **148**(D75).
8. Du, C.S., J.Yeh,et al, Nanotechnology, 2005. **16**: p. 350.
9. Arico, A.S., p.Bruce,et al.. Nature Materials, 2005. **4**: p. 366.
10. Burke, A., Journal of Power Sources, 2000. **91**(1): p. Pages 37-50.
11. Kim, I.H.a.K.B.k., Electrochemical and Solid-State Letters,, 2001. **4**: p. A62.
12. Mastragostino, M.C.A., et al, J. Power Sources, 2001. **97-98**: p. 812.
13. Ryu, K.S., K. M. Kim, et al.,, J. Power Sources, 2002. **103**: p. 305.
14. Zheng, J.P., and T.R.Jow,, J. Electroanal. Chem, 1995. **142**: p. L6.
15. Zheng, J.P., P.J.Cygan et al, J. Electroanal. Chemi., 1995. **142**: p. 2699.
16. Frackowiak, E., K.Jureicz et al., J. Power Sources, 2001. **97-98**: p. 822.
17. Jurewicz, K., S. Delpeux, et al.,, Chem.l Phys. Lett., 2001. **347**: p. 36.
18. Laforgue, A., P.Simon, et al, J. Electrochem. Soc., 2003. **150**: p. A645.
19. H.Li, L.C., Y. Xia, Solid State Lett., 2005. **8**: p. A433.
20. Weir, R.D. and C.W. Nelson. 2008, US patent 7466536.
21. Weir, R.D. and C.W. Nelson. 2006, US Patent 7033406.
22. Ho, J.J., T. R.; Boggs, S. , IEEE Electrical Insulation Magazine 2010. **26**: p. 20.
23. E.A. Nenashevaa, N.F. Kartenkob, J. Eur. Ceram. Soc., 2001. **21**: p. 2697-2701.
24. M. A. Subramanian, 1 Dong Li,* N. Duan,- B. A. Reisner, and A. W. Sleigh, J. Solid State Chem., 2000. **151**: p. 323-325.
25. Ji. Zhang, D., Xianghui,T. Lu,Y. Jiang and J. Zhu, Key. Eng. Mater, 2008. **368-372**: p. 412-412.
26. C. P˘acurariu a, I. Laz˘au a, Z. Ecsedi a, R. Laz˘au a, P. Barvinschi b, G. M˘arginean c, J. Eur. Ceram. Soc., 2007: p. 707–710.
27. D. Domanski, G.U., F. J. Castro§ and Fabiana C. Gennari, J. Am. Ceram. Soc., 2004. **87**(11): p. 2020-2024.
28. S. Guillemet-Fritsch a, T. Lebey b, M. Boulos a, B. Durand a, J. Eur. Ceram. Soc., 2006. **26**: p. 1245–1257.
29. N. Kolev, R.P.B., 2 A. J. Jacobson,2 V. N. Popov,3 V. G. Hadjiev,1 A. P. Litvinchuk,1 and M. N. Iliev1, Phys. Rev. B, 2002. **66**(132102).
30. Morrel H. Cohen, a.J.B.N., a) Lixin He, and David Vanderbilt, J. Appl. Phys., 2003. **94**.
31. Sinclair, D.C., Adams, T. B., Morrison, F. D. and West,, Appl. Phys. Lett., 2002. **80**(12): p. 2153–2155.
32. Sabar D. Hutagalung∗, L.Y.O., Zainal A. Ahmad, J. Alloys Compd., 2009. **476** p. 477–481.

33. Seong-Hyeon Hong*, w.a.D.-Y.K., J. Am. Ceram. Soc., 2007. **90** (7): p. 2118–2121.
34. Aurivillius, B., Ark. Kemi, 1949. **463**(1): p. 499.
35. Chen, X.F.D.a.I.W., J. Am. Ceram. Soc., 1998. **81**: p. 3253.
36. S. T. Zhang, Y.F.C., Z. G. Liu, N. B. Min, J. Wang, and G. X. Cheng,, J. Appl. Phys., 2005. **97**: p. 104106.
37. A. Snedden, C.H.H., and P. Lightfoot,, Phys. Rev. B, 2003. **67**(092102).
38. S. L. Ahn, Y.N., M. Miyayama, and T. Kudo,, Mater. Res. Bull., 2000. **36**: p. 825.
39. A. Srinivas, S.V.S., G. S. Kumar, and M. M. Kumar, J. Phys. : Condens. Matter, 1999. **3335**(11).
40. R. S. Singh, T.B., G. S. Kumar, and S. V. Suryananrayana,, Solid State Commun, 1994. **91**: p. 567.
41. S. Solomon, N.S., I. N. Jawahar, H. Sreemoolanadhan, M. T. Sebastian, J. Mater. Sci. - Mater. Electron, 2000. **11**: p. 595-602.
42. C. Ostos a, L. Mestres a, M.L. Martı´nez-Sarrio´n a, J.E. Garcı´a b, A. Albareda b, R. Perez b, Solid State Sci., 2009. **11**.
43. Bloor D, B.R., Flemings MC, Mahajan S, editors., *The encyclopedia of advanced materials.Oxford.* Pergamon Press, 1994.
44. Koch CC. In: Cahn RW, Mater. Sci. Technol., 1991. **15**: p. 193-245.
45. C., S., *Mechanical Alloying and Milling.* Cambridge International Science Publishing, 1995.
46. C., S., Prog. Mater. Sci, 2001. **46**: p. 1-184.
47. Lai MO, L.L., *Kluwer Academic Publishers,Boston, MA.* Mechanical alloying., 1998.
48. Murty BS, R.S., Int. Mater. Rev, 1998. **43**: p. 101-141.
49. C, S., *Non-equilibrium processing of materials.* Oxford: Pergamon Press, 1999.
50. Bickerdike RL, C.D., Easterbrook JN, Hughes G, Mair WN, Partridge PG, Ranson HC., Int J. Rapid Solidif., 1984. **1**: p. 305-25.
51. T. Furuhashi, M.M., W. Sakamoto, T. Yogo J. Ceram. Soc. Jpn, 2010. **118**: p. 701-705.
52. Cihlar, E.B.a.J., Int. J. Mod Phys B, 2010. **24**: p. 770-779.
53. Kaluza, S., Catal. Lett., 2009. **129**: p. 287-292.
54. NJ. Ali and SJ. Milne, J. Mater. Res, 2006. **21**: p. 1390-1398.
55. A. Goldstein, A.G., M. Hefetz, J. Ceram. Soc. Jpn, 2009. **117**: p. 1281-1283.
56. A. Goldstein, A.G., Y.Yeshurun, M. Hefetz,, J. Am. Ceram. Soc., 2008. **91**: p. 4141-4144.
57. LZ. Pei, Y.Y., JF. Wang, J. Chen, QF. Zhang, Mater. Res.-Ibero-American J. of Mater. chemistry, 2010: p. 339-343.
58. NM Khalil, M.H., EMM Ewais, FA Saleh, J. Alloys Compd., 2010. **496**: p. 600-607.
59. V Montouillout, D.M., A Douy, JP Coutures, J. Am. Ceram. Soc., 1999. **82**: p. 3299-3304.
60. D Dhak, P.P., J. Am. Ceram. Soc., 2006. **89**: p. 1014-1021.
61. RK Pati, P.P., J. Am. Ceram. Soc., 2000. **83**: p. 1822.
62. S Nugroho, Z.C., A Kawasaki, MOD Jarligo, J. Alloys Compd., 2010. **502**.
63. Suryanarayana, C., Progress in Materials Science, 2001. **46**: p. 1-84.

64. B. Gerand, G.N., J. Guenot, M, *Preparative methods in Solid State Chemistry*. Figlarz, Academic press.
65. John D. Wright, N.A.J.M.S., *Sol- Gel Materials : Chemistry and Applications*, in *Advanced Chemistry Texts*. 2001, CRC press.
66. Aegerter, M.A.a.M., M., ed. *Sol-Gel Technologies for Glass Producers and Users* 2004, SPRINGER SCIENCE.
67. Phalippou, J., *Sol-Gel: A Low temperature Process for the Materials of the New Millennium.* 2000.
68. P.B. Avakyan, M.D.N., A.G. Merzhanov, Am. Ceram. Soc. Bull., 1996. **75**: p. P2.
69. Y. Choi, N.-I.C., H.C. Kim, Y.D. Hahn, J. Mater. Sci. , 2000. **11**: p. 25-30.
70. Y. Li, J.Z., J. Han, Mater. Res. Bull., 2002. **37**: p. 583.
71. C.H. Peng, C.C.H., C.K. Hong, S.Y. Cheng, Mater. Sci. Eng. B, 2004. **107**: p. 209.
72. Borovinskaya, A.G.M.a.P., Comb. Sci. Tech, 1975. **10**: p. 195.
73. Sheppard, L.M., Adv. Mater. Proc, 1986. **25**.
74. Schaffer, J.S.F.a.G.B., Metall. Trans. A 1995. **26**: p. 725.
75. Lajtai, E.Z., Tectonophysics, 1971. **11**(2): p. 129-156.
76. W.H. Qi, M.P.W., Mater. Chem. Phys., 2004. **88**: p. 280-284.
77. Doherty, R., Materials Science and Engineering 1997. **A238**: p. 219-274.
78. Jangg G, K.F., Korb G., Aluminium, 1975. **51**: p. 641-5.
79. PG., M., Mater Trans Japan Inst Metals, 1995. **36**: p. 161-9.
80. El-Eskandarany MS, A.K., Suzuki K., J Less-Common Metals, 1990. **167**: p. 113-8.
81. Charlot F, G.e.E., Zeghmati B, Bernanrd F, Niepce JC, Mater Sci and Eng, 1999. **A 262**: p. 279-88.
82. Gauthier V, J.C., Bernard F, Ga E, eLarpin JP., Mater Sci and Eng, 1999. **A 265**: p. 117-28.
83. L.B. Kong a, T.S. Zhang b, J. Ma b, F. Boey b, Prog. Mater Sci., 2008. **53**: p. 207-232.
84. Suryanarayana C, I.E., Boldyrev VV., *Mat. Sci. Eng. A.* 2001. **304-306**: p. 151-8.
85. Varin, R.A., Chiu,C., Li, S., Calka, A. & Wexler, D., J. Alloys Compd., 2004. **370**: p. 230-243.
86. Lohse, B.H., Calka, A., Wexler, D., J. Mater. Sci., 2007. **42**: p. 669-675.
87. Schaffer, G.B.M., P.G., Mater. Forum, 1992. **16**: p. 91-97.
88. Forrester, J.S.S., Metall. Trans. A, 1995. **23A**: p. 725-730.
89. Best, T.E., *The Reduction of Electric Arc Furnace Dust in Carbon Monoxide*, in *Materials and Metallurgical Engineering*. 1998, Queen's University.
90. Hoyaux, M.F., in *Arc Physics*. 1968, Springer-Verlag.
91. Celik, C., et al. 2002, S patent 6379419 B1.
92. Ignatov, A.M., Journal De Physiqu iv, 1997. **17**: p. 215-223.
93. D.Wexler, A.C.a., Nature, 2002. **419**: p. 147-151.
94. R. Dombrowski, D.G., J. Kijtzler, and Chr. Marx, J. Appl. Phys. , 1994. **75**(10): p. 6054-6056.
95. M, A., Phys Rev Lett, 1990. **64**: p. 487-490.
96. Domanski, D., Urretavizcaya, G., Castro, F. J. and Gennan, F. C.,, J. Am. Ceram. Soc., 2004. **87**: p. 2020-2024.

97. A.Calka, J.I.N., Mater. Sci. Forum, 1995. **179-181**: p. 333-338.
98. Gleitrr, H., Prog. Mater Sci., 1989. **33**: p. 213.
99. Radlinski, A.C.a.A.P., Mater. Sci. Eng. A, 1991. **134**.
100. Goldstein, J. *Scanning Electron Microscopy and X-ray Microanalysis*. 2003.
101. Fultz, B.a.H., J ed. *Transmission Electron Microscopy and Diffractometry of Materials*. 2007.
102. P. Balaz, E.G., L. Takacs, E. Gock, Int. J. Materials Prod. Technol. , 2005. **23**: p. 26-41.
103. M A Ram´ırez1, P.R.B., R Tararam1, A A Cavalheiro2, E Longo1 and and J.A. Varela1, J. Phys. D: App. Phys., 2009. **42**(185503).
104. Y.C WU, N.J.H.H.Y.L., J. Microsc, 2005. **220**: p. 205-220.
105. A.Goswami, A.P.G., Thin Solid Films, 1973. **16**: p. 175-185.
106. Wong, C.P. and Y. Rao. 2001, US patent 6544651 B2.
107. Frölich, H., *Theory of Dielectric*. 1958, Clarendon, Oxford.
108. Shoichet, J.H.W.a.M.S., Chem. Mater, 2008. **20**: p. 55-60.
109. S.F. Shao, J.L.Z., P. Zheng, C.L. Wang, Solid State Commun, 2007. **142**: p. 281-286.
110. A.M.M. Farea, S.K., K.M. Batoo, A.Y. Alimuddin, Phys. B, 2008. **403**(684).
111. J.Dercz, A.S., G. Dercz, Int J Thermophys, 2011. **32**: p. 746-761.
112. M.H. Chan, D.M.S., J. Am. Ceram. Soc., 1984. **67**: p. 285.
113. M.H. Chan, M.P.H., D.M. Smyth, J. Am. Ceram. Soc., 1986. **69**: p. 507.
114. F.D. Morrison, D.C.S., J.M.S. Skakle, A.R. West, J. Am. Ceram. Soc., 1998. **81**: p. 1957.
115. F.D. Morrison, D.C.S., A.R. West, J. Am. Ceram. Soc., 2001. **84**(2): p. 474.
116. F.D. Morrison, A.M.C., D.C. Sinclair, A.R. West, J. Electroceram, 2001. **6**: p. 219-232.
117. F.D. Morrison, D.C.S., A.R. West, J. Appl. Phys., 1999. **86**(11): p. 6355.
118. A. Iacculescu, Z.V.M., L.P. Curecheriu, L. Padurariu, R. Trusca, J. Alloys Compd, 2011. **509**: p. 10040-10049.
119. E.A. Nenasheva, N.F.K., J. Eur. Ceram. Soc., 2001. **21**: p. 2697-2701.
120. Finlay D. Morrison, D.C.S., and Anthony R. West, J. Am. Ceram. Soc., 2001. **84**(3): p. 531-38.
121. Saburi, O., J. Phys. Soc. Jpm, 1959. **14**(9): p. 1159-47.
122. A. B. Alles, V.R.W.A., and V. L. Burdick, J. Am. Ceram. Soc., 1989. **72**(1): p. 148-51.
123. SD. Kolar, S.G., Z. Stadler, and D. Suvorov, *1980*. **Ferroelectrics**(1): p. 269-72.
124. K. Wakino, K.M., and H. Tamura, J. Am. Cerurn. Soc, 1984. **67**(4): p. 278-81.
125. Boilot, J.M.D.a.J.P., *1987*. J: Muter. Sci. Lett. **6**: p. 134-36.
126. Nishigaki, H.K., S. Yano, and R. Kamimura, Am. Ceram. Soc.Bull, 1987. **66**(9): p. 1405-10.
127. L. Schreyeck, A.W., H. Fuzellier, J. Mater.Chem, 2001. **11**: p. 483-486.
128. B.P. Ladganonkar, C.B.K., P.N. Vasambekar, A.S. Vaingankar, J. Eng. Mater.Sci, 2000. **419**(7).
129. R. Sarkar, S.K.D., G. Banerjee, Ceram. Int., 1999. **25**: p. 485.
130. B. Alinejad, H.S., A. Beitollahi, A. Saberi, S. Afshar, Mater. Res. Bull., 2008. **43**: p. 1188-1194.

131. *Ted Pella ,Inc (Microscopy Products for Science and Industry)* (*http://www.tedpella.com/company_html/hardness.htm)*.
132. F. Tavangarian, R.E., J. Alloys Compd, 2009. **485**: p. 648-652.
133. D.C. Sinclair, T.B.A., F.D. Morrison, A.R. West, Appl. Phys.Lett., 2002. **80**.
134. S. Y. Chung, I.-D.K., S.-J.L. Kang, Nature Mat. , Nature Mat., 2004. **3**.
135. M.A. Subramanian, A.W.S., Solid State Sci., 2002. **4**.
136. P. Lunkenheimer, V.B., A.V. Pronin, A.I. Ritus, A.A. and A.L. Volkov, Phys. Rev. B, 2002. **66**.
137. B. J. M. Aikin, T.H.C., and D. R. Maurice, Mater. Sci. Eng. A 1991. **147**: p. 229.
138. M.A. Sulaiman, S.D.H., J.J. Mohamed, Z.A. Ahmad, M.F. Ain and B. Ismail, J. Alloys Compd, 2011. **509**: p. 5701-5707.
139. L.T. Mei, H.I.H.a.T.T.F., J. Am. Ceram. Soc., 2008. **91**: p. 3735-3737.
140. Mei, T.T.F.a.L.T., J. Am. Ceram. Soc., 2007. **90**: p. 638-640.

APPENDIX A

EDS mapping

Sintered (900°C for 24 hours) sample of CCT after impact milling for 120 hours

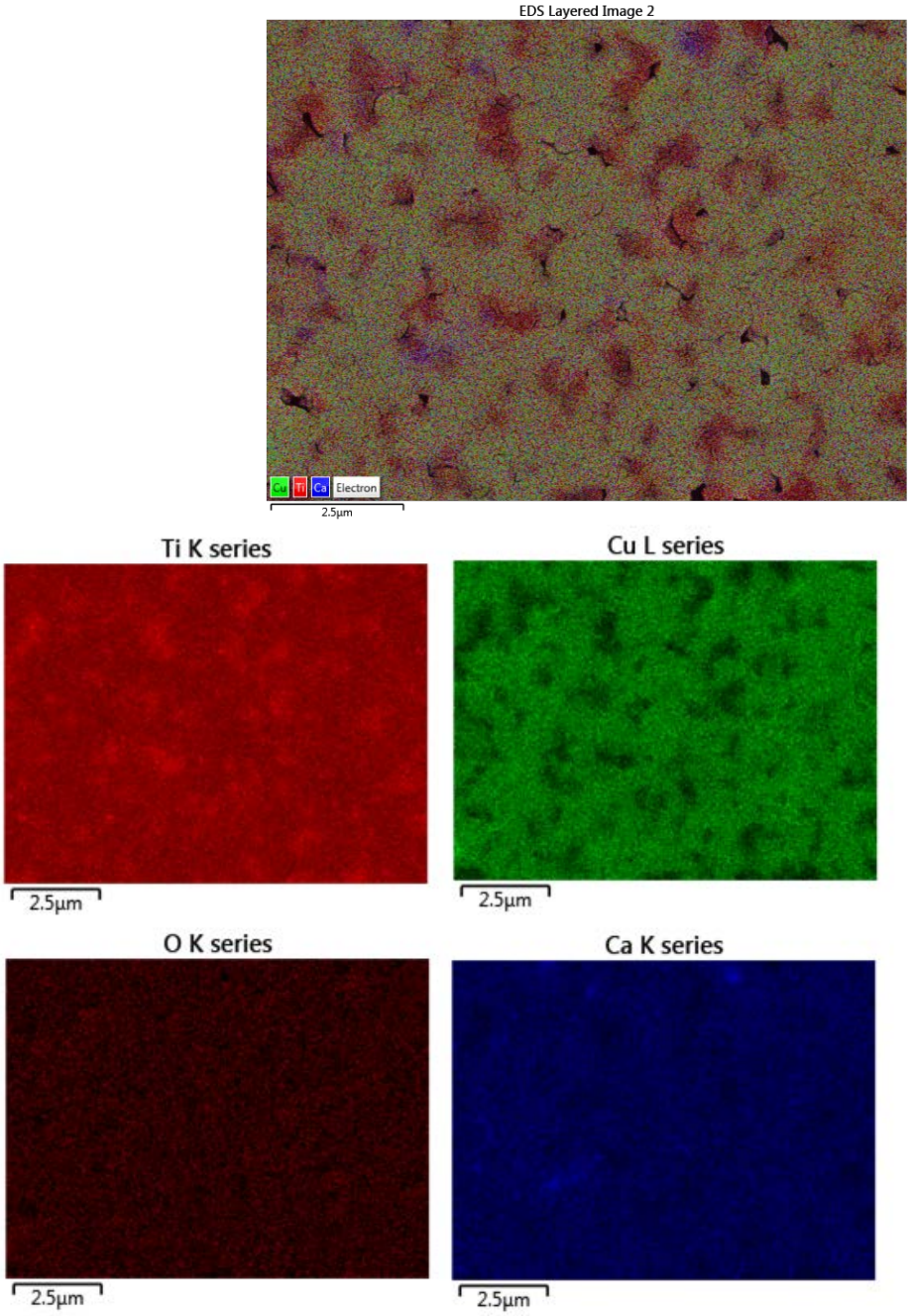

APPENDIX B

EDS Point analysis

Sintered (900°C for 24 hours) sample of CCT after impact milling for 120 hours

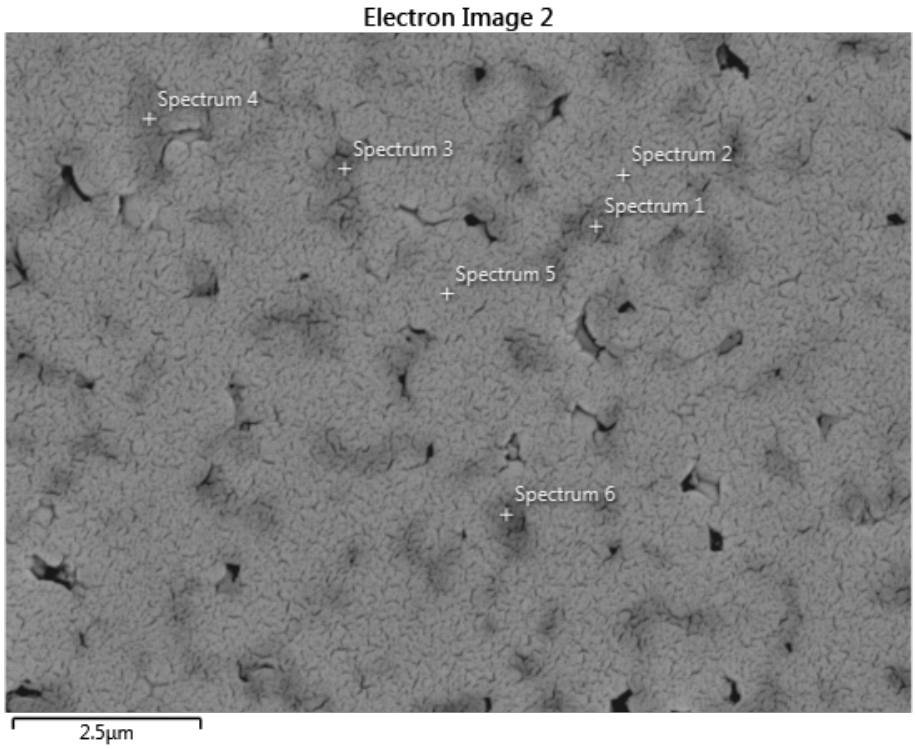

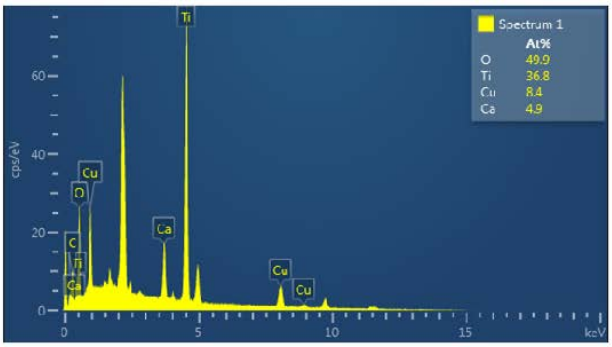
Spectrum 1
At%
O 49.9
Ti 36.8
Cu 8.4
Ca 4.9
cps/eV
keV

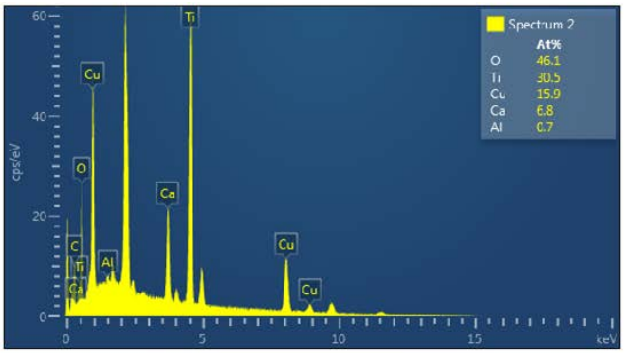
Spectrum 2
At%
O 46.1
Ti 30.5
Cu 15.9
Ca 6.8
Al 0.7
cps/eV
keV

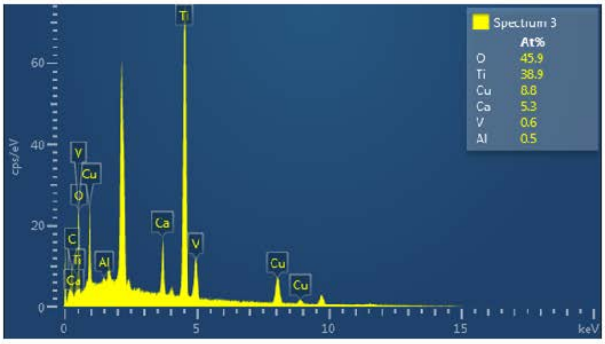
Spectrum 3
At%
O 45.9
Ti 38.9
Cu 8.8
Ca 5.3
V 0.6
Al 0.5
cps/eV
keV

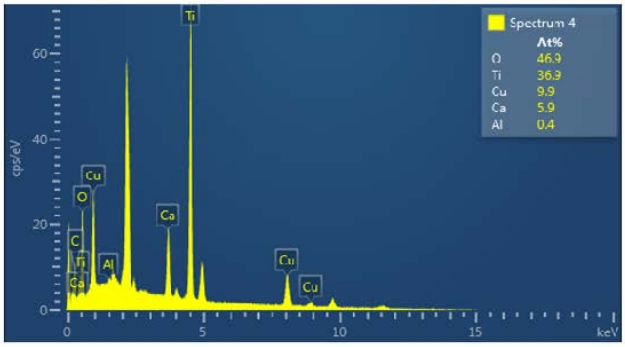
Spectrum 4
At%
O 46.9
Ti 36.9
Cu 9.9
Ca 5.9
Al 0.4
cps/eV
keV

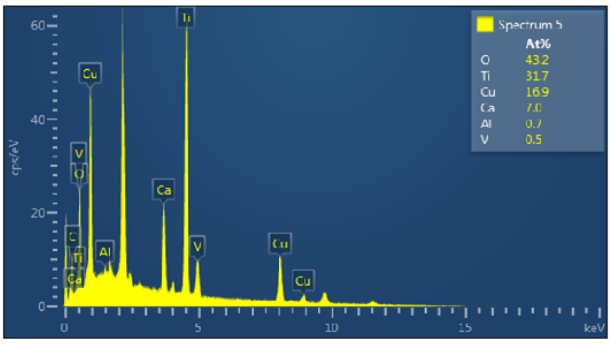
Spectrum 5
At%
O 43.2
Ti 31.7
Cu 16.9
Ca 7.0
Al 0.7
V 0.5
cps/eV
keV

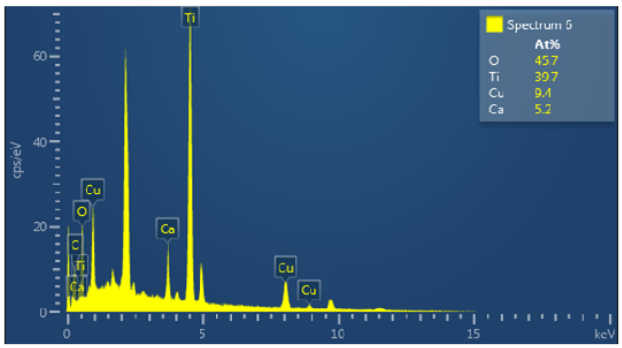
Spectrum 6
At%
O 45.7
Ti 39.7
Cu 9.4
Ca 5.2
cps/eV
keV

APPENDIX C

EDS Analysis

Sintered (900°C for 24 hours) sample of CCT after shear-milling for 120 hours

Secondary electron image

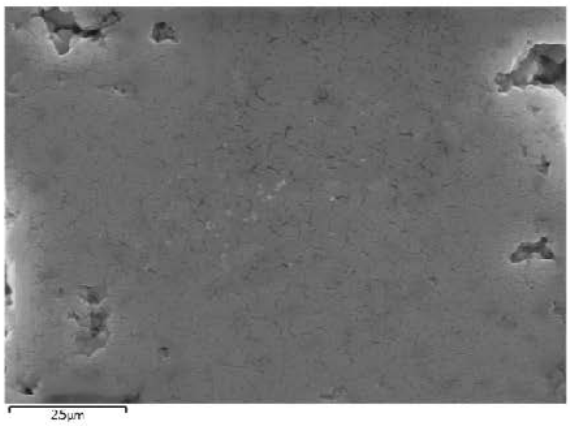

Back scattered image